An Experimental and Theoretical Study of Electric-Field Induced Particle Segregation in Concentrated Suspensions

by

Anil Kumar

A Dissertation Submitted to the Graduate Faculty in Engineering in Partial Fulfillment of the Requirement for the Degree of Doctor of Philosophy

The City University of New York

2005

INFORMATION TO USERS

The quality of this reproduction is dependent upon the quality of the copy submitted. Broken or indistinct print, colored or poor quality illustrations and photographs, print bleed-through, substandard margins, and improper alignment can adversely affect reproduction.

In the unlikely event that the author did not send a complete manuscript and there are missing pages, these will be noted. Also, if unauthorized copyright material had to be removed, a note will indicate the deletion.

ProQuest Information and Learning Company
300 North Zeeb Road
P.O. Box 1346
Ann Arbor, MI 48106-1346

This manuscript has been read and accepted by the Graduate Faculty in Engineering in satisfaction of the dissertation requirement for the degree of Doctor of Philosophy.

10/6/2004

Date

Chairman of Examining Committee

10/6/2004

Date

Executive Officer

Prof. Andreas Acrivos (Mentor)

Prof. Morton Denn

Prof. Charles Maldarelli

Prof. Alexander Couzis

Prof. Boris Khusid

Supervisory Committee

THE CITY UNIVERSITY OF NEW YORK

Abstract

An Experimental and Theoretical Study of Electric-Field Induced Particle Segregation in Concentrated Suspensions

by

Anil Kumar

Advisor: Prof. Andreas Acrivos

This thesis describes an experimental and theoretical investigation of electric-field-induced particle segregation in concentrated suspensions of particles having different electrical properties from that of the suspending fluid. When such a suspension is subjected to a spatially nonuniform electric field, the particles migrate toward the region of high- or low-field, depending on the relative polarization of the suspending fluid and the particles. This phenomenon, known as dielectrophoresis, finds numerous applications in processes involving the collection/trapping, selective filtration and manipulation of individual particles.

We begin by briefly summarizing the theory of the dielectrophoretic force in Chapter 1. In Chapter 2, we present the experimental setup and the suspension physical properties along with a brief description of the various instruments and the methods being employed for the measurement of the various suspension properties. Chapter 3 is devoted to the description of the theoretical model for non-dilute suspensions.

In Chapter 4, we present an experimental study demonstrating the influence of a relatively weak, rotating gravity force on the field-induced particle interactions in a "clinostat" using a positively polarized suspension of heavy particles.

In Chapter 5, we study the behavior of concentrated suspensions ($c_{initial}$~5-15%), comprised of neutrally buoyant, negatively polarized particles, subject to a spatially non-uniform electric field. We find that, following the field exposure, the suspension undergoes a field induced phase transition in which the particles concentrate in the low field region. The process was modeled using an electrohydrodyanamic model, developed by Khusid and Acrivos. In chapter 6, we analyze the electrohydrodynamic model in the special case when, via a similarity transformation, the model equations reduce to ordinary differential equations for the particle concentration. Chapter 7 is devoted to an experimental study of the particle aggregation in neutrally buoyant suspensions subject to a spatially uniform ac electric field in which a new, and hitherto unexplained, pattern formation has been observed.

Preface

This thesis describes an experimental and theoretical investigation of electric-field-induced particle segregation in concentrated suspensions of particles having different electrical properties from that of the suspending fluid. When such a suspension is subjected to a spatially nonuniform electric field, the particles migrate toward the region of high- or low-field, depending on the relative polarization of the suspending fluid and the particles. This phenomenon, known as dielectrophoresis, finds numerous applications in processes involving the collection/trapping, selective filtration and manipulation of individual particles.

In Chapter 1, we begin by briefly summarizing the theory of the dielectrophoretic force. In Chapter 2, we present the experimental setup and the suspension physical properties along with a brief description of the various instruments and the methods being employed for the measurement of various suspension properties. These measurements were essential before any comparison could be made between the theoretical results and the experimental data. In Chapter 3, we describe the theoretical model for non-dilute suspensions. This continuum model was developed by Khusid and Acrivos, and was based on a generalization of their earlier theory for the thermodynamics of field-induced phase transitions in suspensions of polarized particles [*Phys. Rev. E,* ***52****, 1669(1995),* ***54****, 5428(1996), and* ***60****, 3015(1999)*], which treats the suspension as an effective continuum fluid with concentration dependent physical properties and also includes the effects of Brownian motion.

In Chapter 4, we present the experimental results that demonstrate the influence of a relatively weak rotating gravity force on the field-induced particle interactions in a

"clinostat", an electric chamber slowly rotating about its horizontal axis. This study involved conducting experiments in microgravity (aboard NASA's research aircraft KC-135) and on the ground in a horizontally rotating electric chamber capable of generating a spatially non-uniform electric field. The experiments were conducted with a dilute suspension of heavy, positively polarized aluminum particles after exposing it to a high-gradient ac electric field. This experimental and theoretical study has demonstrated that the clinorotation did not produce the zero gravity morphology of the aggregation pattern, indicating that even a relatively weak, rotating gravity could lead to a pronounced effect on the morphology of the field-induced aggregation pattern.

In Chapter 5, we extend the earlier studies, on dilute suspension behavior under non-uniform electric fields employing dielectrophoresis [Dussaud et. al., Qiu et. al., Markarian et. al. JAP], to the case of concentrated suspensions ($c_{initial}$~5-15%) where the particles not only affect each other's motions but the local electric field distribution as well. We performed a series of careful experiments for a wide range of concentrations ($c_{initial}$=5%-15%) with a suspension of Mazola corn oil and Poly alpha-olefin particles having the same density (~0.92g/cc) as that of the oil and which exhibit negative dielectrophoresis. A characteristic feature of all these experiments was the presence of a propagating distinct front between the regions enriched with and depleted of particles. Such a front was not seen at low concentrations ($c_{initial}$<1%), where an undulating boundary was found instead. The experimental results for the front propagation were tested against the predictions of a continuum model, described in Chapter 3, and the theoretical predictions for the front position were found to be quantitatively consistent with the experiments.

In Chapter 6, we focus on elucidating the mechanism of the concentration front formation, as discussed in chapter 5, by examining analytically and numerically the electro-hydrodynamic model in the special case when, via a similarity transformation, the model equations reduce to an ordinary differential equation for the particle concentration. We establish the existence of "shock solutions" to these equations and determine the location of the concentration front and the dependence of the front velocity on the bulk particle concentration of the suspension, the particle polarizability, and the field strength. In particular, we demonstrate that the appearance of the front can be caused either by the electric field induced local phase separation of a suspension or by the rapid local growth of the suspension viscosity due to a field-driven particle accumulation in a certain area.

In Chapter 7, we present the results of an experimental study conducted under spatially uniform electric field conditions, in contrast to our earlier work reported in Chapters 4 and 5 where the field was spatially non-uniform. We report a series of events which occurs beyond the chain/column formation in a suspension exposed to a spatially uniform ac electric field (~1.1-2.2kV/mm, 0.1-3kHz) where, via a new electric field induced bulk phase transition, a cellular pattern is found to evolve. We study the influence of various parameters, such as the field strength, the confinement, the initial suspension concentration, the particle size, the frequency, and the geometrical shapes and sizes, on the morphology and kinetics of the cellular structure growth.

To summarize, this thesis describes many facets of electric-field induced phenomenon, both in spatially uniform and non-uniform ac electric fields, and lists several unanswered questions that could form the basis for future work in this research area.

Acknowledgements

I would like to express my deepest gratitude to Professor Andreas Acrivos for being an extraordinary mentor during the course of my Ph.D. His deep insight into research problems and dedication toward research, along with an extraordinary attention for his students will always be a great source of inspiration to me. I would like to dedicate my work to this great legend.

I am greatly indebted to Professor Boris Khusid at New Jersey Institute of Technology and Dr. David Jacqmin at NASA Glenn Center for their hard work and dedication for research. I would also like to thank Professor Charles Maldrelli, Alexender Couzis, Mark Shattuck, as well as Professor Morton Denn for various valuable suggestions and help in understanding of several research concepts.

I acknowledge the unfailing love, affection and support of my parents, Ranvir Singh and Ombiri Devi, my brother and sister-in-law, Manoj and Shalini, for being a constant source of emotional support during the course of this work.

During my Ph.D. work, I received many valuable suggestions from Dr. Zhiyong Qiu, Dr. Nikolai Markarian, Dr. Bo Jin, Dr. German Drazer, and Mike Yeksel and I am thankful to them. I would specially like to acknowledge the help that I continuously received from Andy Eng and Mr. Xu of Chemical Engineering department for their help from computers to fabrication of my experimental set-ups.

Finally, there are many friends who have helped me in many ways. They are: Manoj K. Sharma, Pradeep Rai, Chandra Shekar, Ravichadra Palaparthi, Nitin Kumar, John Singh, Ashish Taneja, Felomena Califano, Francisco Citro, Vivek Dviwedi, Nikhil Kalyankar, Rajesh Goyal, and Rohit and Shyam and many others whose names I cannot collect.

Contents

List of Tables

List of Figures

and (d_1) 2.5 inch, respectively. Experimental parameters: 3kV/100Hz, L=1.79mm, c=0.02, d_p=90μm. The aerial average number density of the cells for (c)-(d_1) are 17.54, 16.86, and 21.6 cells/inch^2, respectively. Figs. (e)-(f_1) shows the effect of changing the confinement between the electrodes for L= (e) 3.53mm, (f) 2.3mm, and (f_1) 1.7mm, respectively. Experimental parameters: E=1.7kV/mm, f=100Hz, c=0.02(v/v), D=2.02", d_p=90μm. (e)-(f_1) corresponds to N_{cells} = 17, 37, and 66, respectively. Figs. (g)-(h_1) shows the effect of changing the initial particle concentration for c= (g) 0.01, (h) 0.03, and (h_1) 0.05 (v/v), respectively. Experimental parameters: E=1.7kV/mm, f=100Hz, D=2.0", L=2.3mm, d_p=90μm. (g)-(h_1) corresponds to N_{cells} = 28, 45, and 63, respectively. Figs. (i)- (j_1) shows the effect of varying the particle diameter, d_p, where (i) and (j) are for d_p=90μm whereas (i_1) and (j_1) are for d_p=45μm. (i) and (i_1) corresponds to c=0.01, L=1.7mm while (j) and (j_1) corresponds to c=0.02, L=2.3mm. Experimental parameters: E=1.7kV/mm, f=100Hz, D=2 inch. (i)-(j_1) corresponds to N_{cells}= (i) 54, (i_1) 59, (j) 36, and (j_1) 37, respectively. Fig. (k) shows the particle columns spanning the gap between the electrodes when observed from an angle ~30^0 to the horizontal plane. Experimental parameters: c=0.02(v/v), L=1.79mm, 3kV/100Hz, d_p=90μm, D=1.5 inch. 110

7.3 Shows the effect of varying the frequency [(a)-(c)], the magnitude of the field strength [(d)-(f)], and the ramp of the applied field [(g)-(h)] on the final structural morphology. Figs. (a)-(c) correspond to frequencies, f= (a) 100Hz, (b) 1kHz and (c) 3kHz, respectively. The experimental pictures were taken ~30min following the field application. Experimental parameters: E=1.7kV/mm, D=1.5 inch, L=1.79mm, c=0.01, d_p=90μm. (a)-(c) corresponds to N_{cells} = 24, 26, and 23 respectively. Figs. (d)-(f) were taken after 60min, 30min and 20min, respectively following the application of the electric field of strength, E= 1.2, 1.7, 2.2kV/mm. f=100Hz, D=1.5 inch, L=1.79mm, c=0.02, d_p=90μm. (d)-(f) corresponds to N_{cells} = 39, 29, and 24 respectively. Photos, (g) and (h) were, taken after 55min following the application of an applied field, for increasing and decreasing ramp, respectively. The experiment for increasing ramp was conducted by applying an instantaneous field of 0.28V/mm followed by an increase at 0.028V/(mm.min) at steps of one minute, till the final value of 1.82kV/mm was reached over a period of 55 min, while for decreasing ramp, we applied 1.82kV/mm followed by a decrease at 0.028V/(mm.min) at steps of one minute, till the final value of 0.28kV/mm over a period of 55 min was achieved. D=1.5 inch, L=1.79mm, c=0.02, d_p=90μm, f=100Hz. 111

Chapter 1

Introduction to Dielectrophoresis

1.1 Introduction

In this section we will explain some of the basic concepts, to be applied to a suspension containing uncharged particles having electrical properties (permittivity and conductivity) different from those of the fluid. When such a suspension is subjected to an electric field, the particles become polarized and if the electric field is spatially non-uniform, the particles (even if uncharged) experience a net force, known as the dielectrophoretic force [7]. The origin of this force can be understood using the simple concept of a dipole being placed in a spatially non-uniform electric field. Under these conditions, the positive charge on the dipole experiences a different force than the negative charge, and hence a net force is exerted on the particle, which is proportional to the product of the dipole moment and the gradient of the applied field. But since the dipole moment is proportional to the strength of the applied field, the dielectrophoretic force appears, in turn, to be proportional to the product of the particle polarization times the gradient of the square of the applied field. This implies that, under the action of an AC electric field, the dielectrophoretic force on a particle, being proportional to the square of the field, does

not change its sign during the field oscillations and therefore attains a nonzero time-average value.

This dielectrophoretic force moves the particle to regions of either high field (positive dielectrophoresis) or low field (negative dielectrophoresis), depending on the sign of the polarizability of the particles relative to the suspending fluid. There are several ways in which the dielectrophoretic force acting on the particle can be changed. First, it can be controlled by changing the geometry of the system in which the experiment is being performed, thereby tailoring the electric-field distribution to whatever suits the requirements. Secondly, by changing the frequency of the applied electric field, which changes the relative particle polarization and therefore the dielectrophoretic force.

One major advantage of dielectrophoresis over electrophoresis, which refers to the motion of charged particles in a uniform dc field, is its applicability to both charged and uncharged particles. Another advantage of AC dielectrophoresis, as compared to electrophoresis, is that it eliminates undesirable electrolytic effects in the suspending fluid and does not depend on the particle charge, which is difficult to control. In many cases these advantages are more important than the fact that the use of relatively high electric fields in dielectrophoresis could generate an undesirable degree of heating within the suspension. Because of numerous advantages of dielectrophoresis, it has been applied in a great variety of processes involving the control and manipulation of particle motions, such as separation [**8**], filtration [**8**], orientation, sorting, levitation and particle characterization. Also, it is currently receiving increased attention because of its potential application in miniaturized analytical instrumentation for biological systems.

The focus of the theoretical and experimental research on dielectrophoretic phenomena has varied throughout the years. Specifically, the theoretical studies have focused on deriving the expression for the dielectrophoretic force acting on a single dielectric particle (not perfectly insulating or perfectly conducting, layered, non-spherical etc.), and a detailed account of this work has been compiled in reference [**7**]. In contrast, most of the earlier experimental investigations on dielectrophoresis in suspensions have dealt with the design and fabrication of dielectrophoretic filters for removing particles from the fluid [**8-11**]. But, due to the complexity of such filters because of their complicated geometry and associated flow patterns, the studies referred to above were mostly concerned with the issue of the collection efficiency of these devices as measured by the inlet and outlet concentration of the particles in the suspension, as a function of the applied voltage, field frequency, flow rate, and the type of particles.

Recent investigations of dielectrophoretic phenomena in suspensions focus on the development of microdevices for the separation of biospecies [**12-16**]. In these series of experiments, it has been shown that dielectrophoresis is able to separate two populations of particles which exhibit positive and negative dielectrophoresis [**12,13**]. In addition, it has been found that different particles, all of which exhibited negative dielectrophoresis, could be separated by means of an original combination of dielectrophoretic and gravitational field flow fractionation [**16**]. Most studies on biological suspensions used a flat, transparent horizontal microchannel equipped with an array of miniature electrodes at the bottom, in which the particle motions were observed by looking from the top under a microscope. But due to the small size of these devices and the complexity of the flow pattern involved as well as the difficulty of ascertaining the position of the particles, their

velocities etc., none of the authors [**14, 15**] tried, to our knowledge, to investigate the motion of the particles in microdevices. One such attempt was undertaken in Prof. Khusid's research group at NJIT, the description of which can be found in recently published articles [**6,17,18**].

Recently, two studies have appeared dealing both theoretically and experimentally with the motion of individual particles for the case of dilute suspensions subjected to high-gradient strong electric field [**4, 5**]. The results of these studies showed good agreement between theoretical predictions and the experimental data.

In what follows, we will present the basic theoretical background pertaining to the particle response to an applied ac electric field along with derivation of the expression for the dielectrophoretic force acting on these polarized particles when exposed to a spatially non-uniform electric field.

1.2 Theoretical Background

If the particle is perfectly dielectric, the particle polarization will follow instantaneously the time variation of the applied electric field, but there are numerous mechanisms which can lead to energy dissipation in suspensions when placed in an electric field including conduction and dielectric relaxation phenomena. Specifically when energy dissipation is present in the system, the basic assumption of a loss-less dielectric (or of a perfect dielectric) fails and the particle dipole moment does not follow the same time variation as that of the applied field. The polarization of such a suspension exhibits a time delay when an electric field is suddenly applied and has a phase lag when the electric field is a sinusoidal function of time. Our research, presented in the following chapters, deals with suspensions whose polarization cannot be described by the model of a perfect dielectric

with the result that the dielectric permittivity of the suspensions, when exposed to an ac electric field, is a complex number the imaginary part of which characterizes the loss of the electric energy during a cycle of the field oscillation. In this section we will focus on understanding the theoretical basis for characterizing the behavior of these non-perfect dielectric particles and their subsequent response to an AC electric field.

1.2.1 Dielectric Response of Materials

The macroscopic response of an isotropic dielectric exposed to a time varying relatively weak electric field, E(t), can be described (in SI units) by the following equation [**19**]:

$$D(t) = \varepsilon_0 E(t) + \varepsilon_0 \int_0^{\infty} f(\tau) E(t-\tau) d\tau \qquad (1.1)$$

where D(t) is the electric displacement, ε_0 is the dielectric constant of a vacuum and $f(\tau)$, which is a scalar function, characterizes the history dependence of the material polarization. This function accounts for some inertia of the displacement of charges when the material is subjected to a field. The linearity of Eq. (1.1) with respect to the electric field strength enables one to decompose the polarization of a material subjected to an AC electric field, $E(t) = E(\omega)\exp(i\omega t)$, into Fourier components such that

$$D(\omega) = \varepsilon(\omega) E(\omega) \qquad (1.2)$$

where ω is the frequency of the applied field and ε_0 is included, for brevity, into $\varepsilon(\omega)$. $D(\omega)$, in general, is out of phase with $E(\omega)$ and the complex number $\varepsilon(\omega)$, the proportionality factor between them, is called the complex dielectric permittivity. Splitting $\varepsilon(\omega)$ into its real and imaginary part yields:

$$\varepsilon(\omega) = \varepsilon'(\omega) - i\varepsilon''(\omega) \qquad (1.3)$$

where $\varepsilon'(\omega)$ determines the polarization of the dielectric, whereas $\varepsilon''(\omega)$ accounts for the energy loss. As an example, the widely used Debye model for the polarization of a non-perfect dielectric [**20**] leads to the following expressions for $\varepsilon'(\omega)$ and $\varepsilon''(\omega)$:

$$\varepsilon'(\omega) = \varepsilon_\infty + \frac{\varepsilon_s - \varepsilon_\infty}{1+\omega^2\tau^2}$$
$$\varepsilon''(\omega) = (\varepsilon_s - \varepsilon_\infty)\frac{\omega\tau}{1+\omega^2\tau^2} \qquad (1.4)$$

where ε_s and ε_∞ refer to the static and optical dielectric constants, respectively, and τ denotes the time constant characterizing the relaxation time of the dipole moment of the particles or molecules. These functions are illustrated in [**Fig. 1.1**].

For the model of a perfect dielectric with $f(\tau) = \chi\delta(\tau)$, where $\delta(\tau)$ being the delta function and χ being the electric susceptibility of the dielectric, Eq. (1.1) yields

$$D(t) = \varepsilon_0 E(t) + \varepsilon_0\chi E(t) = \varepsilon_0(1+\chi)E(t) \quad \text{or} \quad D(t) = \varepsilon E(t) \qquad (1.5)$$

where $\varepsilon = \varepsilon_0(1+\chi)$ is the dielectric constant of the material. For an AC field, Eq. (1.5) can be written as

$$D(\omega) = \varepsilon E(\omega) \qquad (1.6)$$

This expression shows that the dielectric displacement of a perfect dielectric does not depend on the frequency of the applied field. Moreover, the dielectric constant, ε, does not contain an imaginary part, so that there is no phase shift between the electric displacement and the applied field. The model of a perfect dielectric is only applicable for insulating liquids such as transformer oils, when the real part of the dielectric constant does not vary over a wide range of frequencies and its imaginary part can be neglected. A schematic for the plots of the dielectric constants for both, i.e., a perfect and a non-perfect dielectric is depicted in [**Fig. 1.2**]. Recall that, in our work we shall be using mostly the

model of a non-perfect dielectric. For example, [**Fig. 1.3**] shows the values of the real and imaginary parts of the complex dielectric permittivities of the corn oil and of a 10%(v/v) suspension of polyolefin particles in corn oil. As can be seen from [**Fig. 1.3**] the model of a perfect dielectric, which generally is of very limited use for colloidal suspensions, cannot describe this system [**21**].

1.2.2 Theory of the Ponderomotive Force

In this section we will focus on deriving the expression of the dielectrophoretic force on a freely suspended single sphere in the presence of a spatially non-uniform ac electric field. Recall from the previous section that, when a dielectric particle, having no net charge, is placed in a spatially non-uniform electrostatic field, $\overline{E}$, the particle become polarized and a dipole is formed consisting of equal and opposite charges, +q and –q, which are located at $\bar{r} + \bar{d}$ and $\bar{r}$ respectively, as depicted in [**Fig. 1.4**]

If the applied field is spatially non-uniform, these two charges (+q and –q) will experience different values of the vector field $\overline{E}$ and, thus, the dipole will experience a net force. Summing the forces acting on these charges, we have [**7**]

$$\overline{F} = q\overline{E}(\bar{r} + \bar{d}) - q\overline{E}(\bar{r}) \qquad (1.7)$$

Eq. (1.7) can be simplified for the case when $|\bar{d}|$ is small compared to the characteristic dimension of the electric field nonuniformity. In this case, the electric field can be expanded about $\bar{r}$ using a Taylor series expansion.

$$\overline{E}(\bar{r} + \bar{d}) = \overline{E}(\bar{r}) + \bar{d} \bullet \nabla\overline{E}(\bar{r}) + ... \qquad (1.8)$$

where all the additional terms, of order higher than d, have been neglected, this being a good approximation for the case when $|\bar{d}|$ is small relative to the length scale over which

$\overline{E}$ varies. Combining Eq. (1.7) and Eq. (1.8), the force acting on the particle can be written as

$$\overline{\mathrm{F}} = \mathrm{q}\overline{\mathrm{d}} \bullet \nabla\overline{\mathrm{E}} + ... \tag{1.9}$$

If the limit $\left|\overline{\mathrm{d}}\right| \to 0$ is taken in such a way that the dipole moment $\overline{p} \equiv q\overline{d}$ is finite then the following expression for the force acting on an infinitesimal dipole results:

$$\overline{\mathrm{F}}_{\mathrm{dipole}} = \overline{\mathrm{p}} \bullet \nabla\overline{\mathrm{E}} \tag{1.10}$$

where $\overline{\mathrm{p}}$ is the vector starting from the location of the –q charge and ending at that of +q. For the special case of a homogeneous, dielectric single sphere, with its center at $\bar{r}$, immersed in a perfectly dielectric medium, the expression for the effective dipole moment is [**7**]:

$$\overline{p}_{eff} = 4\pi\varepsilon_f \beta R^3 \overline{E} \tag{1.11}$$

where R is the radius of the particle, $\overline{E}$ is the applied field and β, known as the Clausius-Mossotti function which characterizes the effective polarization of a spherical particle as a function of ε_f (the permittivity of the suspending medium) and ε_p (the permitivity of the particles), is defined as

$$\beta(\varepsilon_p, \varepsilon_f) = \frac{\varepsilon_p - \varepsilon_f}{\varepsilon_p + 2\varepsilon_f} \tag{1.12}$$

Combining Eqs. (1.10-1.12) and taking into the account that $\nabla \times \overline{E} = 0$, where the effect of the magnetic field was neglected (which is the case for all our experiments because there is no free charge moving in the system), we obtain the following expression for the dielectrophoretic (DEP) force acting on a perfect dielectric spherical particle [**19**]

$$\overline{F}_{DEP} = 2\pi\varepsilon_f R^3 \left(\frac{\varepsilon_p - \varepsilon_f}{\varepsilon_p + 2\varepsilon_f} \right) \nabla E^2 \tag{1.13}$$

A careful examination of Eq. (1.13) reveals some of the important features of the dielectrophoretic force acting on the particle some of which can be summarized as follows:

1. $\overline{F}_{DEP}$ is proportional to the particle volume.
2. $\overline{F}_{DEP}$ is proportional to ε_f, the dielectric permittivity of the medium in which the particles are suspended.
3. $\overline{F}_{DEP}$ depends on the magnitude and the sign of the Clausius-Mossotti function, β. The latter is a very important parameter the sign of which determines whether we have positive or negative dielectrophoresis.
4. $\overline{F}_{DEP}$ is directed along the gradient of the electric field intensity ∇E^2, which in general is not parallel to the electric field vector $\overline{E}(\overline{r})$.

As mentioned above, we can distinguish two special cases of dielectrophoresis depending on the sign of the Clausius-Mossotti coefficient, β:

Positive Dielectrophoresis: when $\beta > 0$ (or $\varepsilon_p > \varepsilon_f$), the particles are attracted into the region of high electric field and are repelled from the region of low field intensity.

Negative Dielectrophoresis: In contrast, when $\beta < 0$ (or $\varepsilon_p < \varepsilon_f$), the particles are attracted into the region of low electric field and are repelled from the region of high field intensity.

Now, lets consider the case of a leaky dielectric, i.e. a non-perfect dielectric, in which both the fluid and the spherical particle have finite energy losses depending on the

frequency of the applied signal. In the presence of an AC electric field $\overline{E}$ of frequency ω, the equation for the complex effective dipole moment of a single sphere becomes [7], in lieu of Eqs. (1.11) and (1.12):

$$\overline{p}^*_{eff} = 4\pi\varepsilon_f \beta^* R^3 \overline{E} \tag{1.14}$$

where the complex Clausius-Mossotti factor is now

$$\beta^*(\varepsilon_p{}^*, \varepsilon_f{}^*) = \frac{\varepsilon_p{}^* - \varepsilon_f{}^*}{\varepsilon_p{}^* + 2\varepsilon_f{}^*} \tag{1.15}$$

with the complex permittivities of the particle and the suspending medium being given by:

$$\begin{aligned} \varepsilon_p{}^* &= \varepsilon'_p - i\varepsilon''_p \\ \varepsilon_f{}^* &= \varepsilon'_f - i\varepsilon''_f \end{aligned} \tag{1.16}$$

where ε''_f and ε''_p are the frequency dependent dielectric loss terms. Hence, the time-averaged dielectrophoretic force in such case can be written as [7]

$$\left\langle \overline{F}_{DEP} \right\rangle = 2\pi\varepsilon_f R^3 \,\mathrm{Re}\left[\beta^*\right] \nabla E^2{}_{rms} \tag{1.17}$$

where E_{rms} is the root mean-square magnitude of the imposed AC electric field. The real part of the Clausius-Mossotti function $\mathrm{Re}\left[\beta^*\right]$ determines the frequency dependence of the time-averaged dielectrophoretic force. According to the expression given above, the existence of a dielectrophoretic force requires that two essential conditions be satisfied, namely that the relative particle polarization be non-zero and that the electrode configuration be capable of generating a spatially non-uniform electric field.

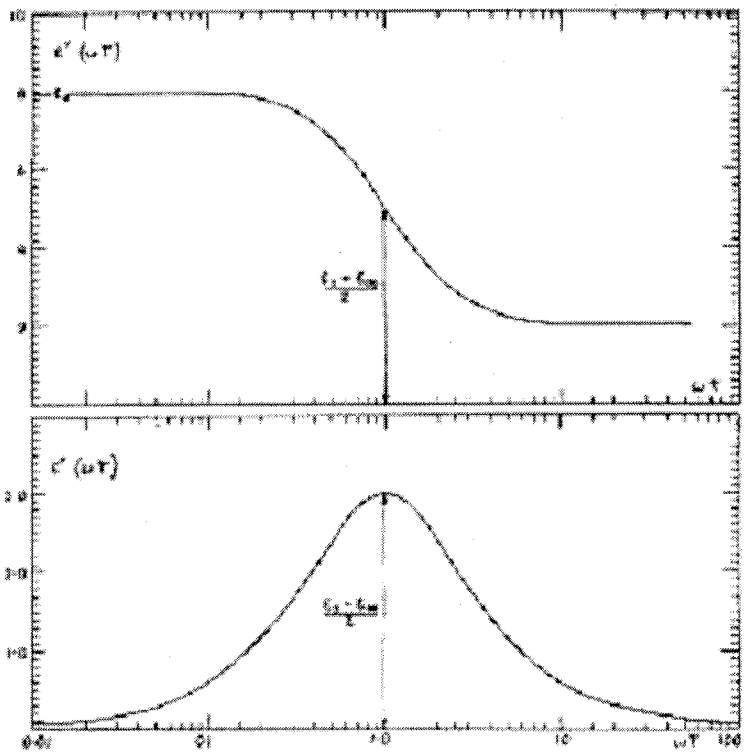

Figure. 1.1: Relaxation in the dielectric with a single relaxation time (Daniel, 1967): (a) the real part of ε^* as a function of $\log(\omega\tau)$ according to the Debye equations; (b) the imaginary part of ε^* for the same dielectric.

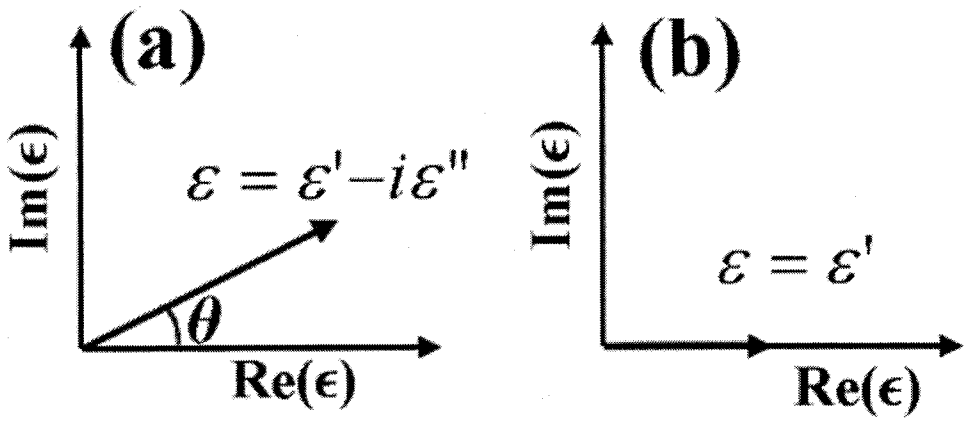

Figure 1.2: The dielectric permittivity of a non-perfect dielectric and a perfect dielectric: (a) Non-perfect dielectric, where θ is the phase shift between the electric displacement D(t) and the applied electric field E(t); (b) Perfect dielectric showing no phase shift between D(t) and E(t).

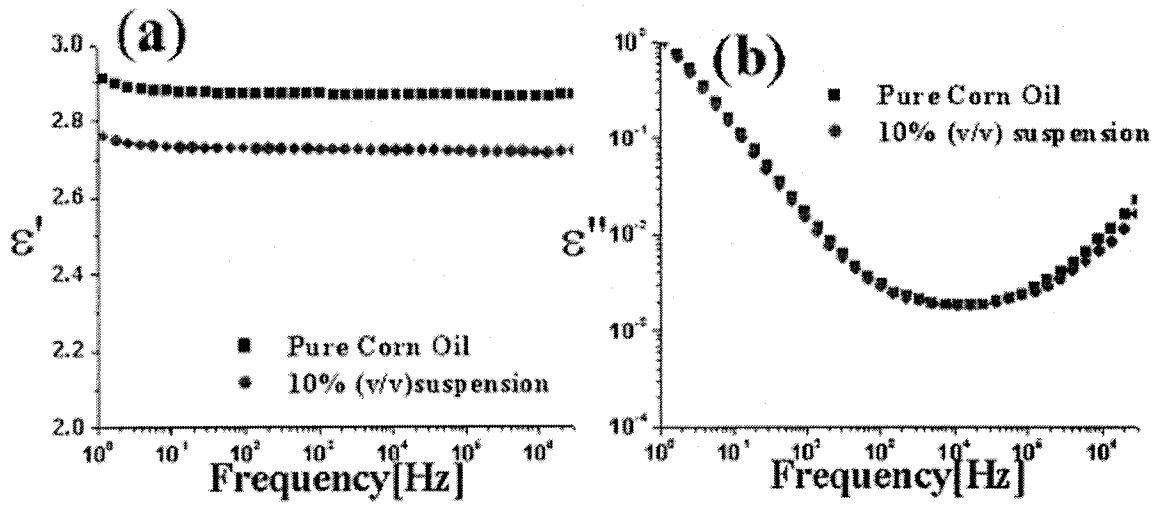

Figure 1.3: Comparison of the (a) real and (b) imaginary part of the complex dielectric permittivity for the case of pure corn oil and a 10%(v/v) suspension of polyolefin particle in corn oil [Calibration factor is taken from Ref. 4]. The decrease in the dielectric permittivity when particles are added to the corn oil shows that this suspension will exhibit negative dielectrophoresis.

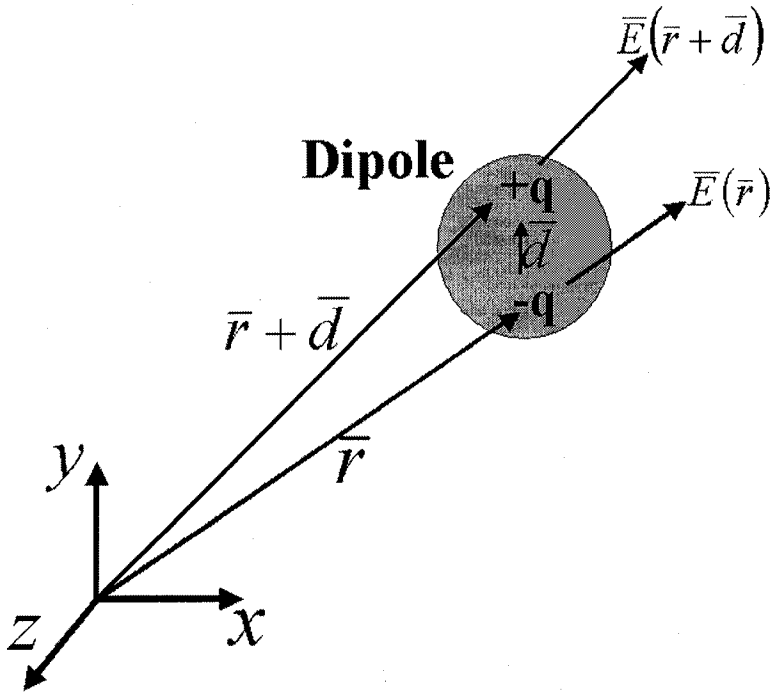

Figure 1.4: When a dielectric particle having zero net charge is placed in an electric field, a dipole moment $\bar{p} = q\bar{d}$ is formed as a result of a dielectric mismatch between the fluid and the particle, and when the applied field strength is spatially non-uniform, the particle experiences a net force.

Chapter 2

Experimental Setup and Procedures for the Suspension Characterization

2.1 Introduction

Recall from Eq. (1.17) that, in order to study the dielectrophoretic behavior of a suspension, we need to satisfy two conditions, namely a non-zero relative particle polarization, $\mathrm{Re}(\beta^*) \neq 0$ and an electrode assembly capable of generating a spatially non-uniform electric field. In this chapter, we first describe the electrohydrodynamic experimental setup used in our research to study the dielectrophoretic behavior of suspensions to be presented in Chapter 4 and 5, and the subsequent electric field distribution. This will be followed by a brief description of the various instruments being used for the suspension characterization and the results thereby obtained.

2.2 Experimental Setup

2.2.1 The Electric Chamber

The electric chamber used for generating the non-uniform electric field consisted of a horizontal parallel-plate chamber (6 cm wide, 12 cm long, and 3 mm high) [**Fig. 2.1(a)**]. The bottom of the Plexiglas chamber was equipped with 16 linear, flat, brass electrodes

(1.6 mm wide and 11 cm long) having smoothed edges, which were embedded into 1.6-mm-deep groves at 2 mm intervals. The electrodes were alternately connected to the high voltage and to the ground. The top of the chamber, consisting of a transparent glass coated with a conducting layer of indium tin oxide (ITO), was grounded. A Teflon spacer was used to keep a gap between the chamber top and bottom. The chamber was illuminated through the transparent top plate using a spread beam light source so as to visualize the particles. The particle segregation was recorded through the top by a digital camera fixed above the chamber. The applied ac field, the amplitude and frequency of which varied from 1 to 5 kV rms (root mean square) and 0.1 to 3 kHz, was produced with a high voltage amplifier (model 10/40, Trek Inc., Medina NY). These frequency and voltage ranges were selected in order to suppress the effects of electro-convection and, for an occasionally charged particle its oscillatory motion due to the sinusoidal nature of the ac-field.

2.2.2 Computation of the Electric-Field Distribution in the absence of particles

To compute the ∇E^2_{rms} in the absence of particles, we need to solve the Laplace's equation $\nabla^2\phi = 0$ where ϕ refers to the voltage. Since the gap between the electrodes (2 mm) was small compared to the length of the channel (11 cm), the field was taken to be two-dimensional and to vary only within the cross section of the channel. In addition, because of the symmetry and the periodicity of the electrode assembly, the electric field was computed only for the element enclosing two adjacent halves of the high-voltage electrodes along with one full ground electrode in between. The sides were considered as insulating boundaries (by symmetry) and the top was taken as being grounded. The

similar dielectric properties of the corn oil, $\varepsilon_f = 2.87$, and the acrylic sheet, $\varepsilon_{acrylic} = 3.0$, permits simplification of the problem to the one shown in [**Fig. 2.2**], where a symmetry boundary condition in the region, located between the electrodes, is imposed. The effect of taking this assumption at the bottom of the chamber between the electrodes was reported [**4**] to change the field strength in the corn oil, the suspending fluid, by less than 2% and therefore justifies the simplification just described.

Laplace's equation was then solved using a finite element code from a library of C++ finite element subroutine called DIFFPACK (version 1.4), developed at the University of Oslo, Norway [**22**]. All the variables were rendered dimensionless using the rms value of the voltage applied to the energized electrodes, (V_{rms}), as the characteristic voltage, and the distance, d, between the electrodes as the characteristic length scale in both the horizontal (x) and vertical (y) directions. To match the experimental conditions, the electric field distribution shown in [**Fig. 2.1(b)**] was computed for a channel of electrode gap ratio (center to center distance) equal to 3.6 with the range $[0 \le x \le 0.8$ and $6.4 \le x \le 7.2]$ corresponding to the two halves of the high-voltage electrode and $[2.8 \le x \le 4.4]$ being the full ground electrode. Notice the appearance of two regions of high field strength near the electrode edges and a wide region of low strength above the center of the grounded electrode near the midplane of the channel, in which the negatively polarized particles are expected to accumulate.

2.3 Suspension Characterization

Before any comparison could be made between the experimental data and the theoretical results is was essential that the suspension properties, specifically the relative particle polarization and particle size distribution, be first measured In this section, we will

describe the various instruments which were used for this purpose along with a brief description of their operating principles.

2.3.1 Dielectric Spectroscopy: BDS 80 Dielectric Spectrometer

This instrument can be used for measuring both the dielectric and magnetic properties of the suspensions over a broad range of frequencies and temperatures. Recall from Chapter 1, that the frequency of the applied field is an important parameter, which can be used for tuning the electrical properties of the material by changing the polarization of its molecules as well as for studying the relaxation process in the molecules. This instrument can also be used for measuring the properties of a material as a function of five independent variables: the frequency, temperature, AC voltage, time and DC bias, out of which any four free variables can be arranged in an arbitrary order. For each independent variable, the user can create a value list containing up to 1000 points with linear, logarithmic or arbitrary distance between the points. In addition to fixed setpoints, an arbitrary series of temperature ramps or time intervals for continuous measurements can be defined. Some of the basic features of this instrument include:

- A Frequency range: $10\,\mu Hz \rightarrow 1.8 GHz$
- Accuracy: $\tan(\delta) \equiv \frac{\varepsilon''}{\varepsilon'} < 10^{-4}$
- An Impedance range: $1 Ohm \rightarrow 10^{14} Ohm$

This instrument is connected to a computer by mean of which the user is able to control various operating parameters (such as the temperature conditions, the applied field, the frequency range etc.) for any measurement online. During the measurement, the data are displayed on-line in the form of a graph as well as in the form of a numerical table in a

log window. In addition, all the activities of the software and the state of the device are presented in a message window. Finally, the actual system state is graphically displayed in a status window.

Recall, from Chapter 1, that to compute the dielectrophoretic force we need to determine the real part of the relative polarization, $\mathrm{Re}[\beta^*]$ which requires measuring the dielectric permittivity of the particle, ε^*_p. This is hard to achieve directly given that ε^*_p is sensitive to the medium in which the measurements are being performed. We employed an alternative way in which the complex permittivity of a suspension of randomly distributed spherical particles was first measured for different suspension concentrations c, along with the complex permittivity of the pure fluid and then the Maxwell-Wagner expression Eq. (2.1) was applied to determine the real part of the relative polarization $\mathrm{Re}[\beta^*]$: [**18**]

$$\mathrm{Re}\left(\frac{\varepsilon_s^* - \varepsilon_f^*}{\varepsilon_s^* + 2\varepsilon_f^*}\right) = c\,\mathrm{Re}(\beta^*)$$
$$\mathrm{Re}(\beta^*) = \mathrm{Re}\left(\frac{\varepsilon_p^* - \varepsilon_f^*}{\varepsilon_p^* + 2\varepsilon_f^*}\right) \qquad (2.1)$$

where c is the volume concentration of the particles, ε_f^* and ε_s^* are the complex dielectric permittivities of the suspending fluid and the suspension, respectively, and β^* is the relative particle polarization. The value of $\mathrm{Re}[\beta^*]$ was determined from the slope of $\mathrm{Re}\left(\frac{\varepsilon_s^* - \varepsilon_f^*}{\varepsilon_s^* + 2\varepsilon_f^*}\right)$ vs. c after fitting the data with a line passing through zero over a frequency range. The result of such measurements for the suspension of aluminum oxide particles in Mazola Corn oil is shown in [**Fig. 2.3**] [**5**]. Notice that for the suspension,

$\mathrm{Re}[\beta^*] > 0$, therefore these particles would be expected to accumulate in regions of high-field strength as a result of positive dielectrophoresis. In contrast the measurements for the suspension of polyolefin particles in corn oil showed that $\mathrm{Re}[\beta^*] < 0$ therefore we would expect these particles to accumulate in regions of low-field strength [**Fig. 2.4**]. In addition, as seen in [**Fig. (1.3)**], the dielectric permittivities of the corn oil was found to be constant, $\varepsilon_f = 2.87$, over the frequency range from 1 Hz to 3 MHz. The dielectric sample cell used in all these measurements consisted of a round plate capacitor (20 mm in diameter) filled with a suspension and the cell constant was determined with pure hexadecane (Aldrich Chemical Co., St. Louis, MO, 99%). During all the measurements, the temperature of the cell was controlled at 22.0 ± 0.05^0C. All these measurements were performed at a low electric field ~ 4 V/mm due to the limitation of the measuring device, in contrast to our dielectrophoretic experiments which were conducted at a much higher strength of the applied electric field ~kV/mm. So a valid question is whether these values for the electrical permittivity, which were measured at low field, are accurate enough for predicting the behavior of the suspensions under high fields. In our work we will show that even though the measurements were conducted at low field strengths, they are able to capture accurately the behavior of the suspensions even at the higher field strengths of several ~kV/mm.

A series of steps which were taken to perform measurements on this device are briefly outlined in **APPENDIX 2A**.

2.3.2 Particle Counters

These analytical instruments were used for the characterization of the particle size distribution in the suspensions. We used two separate instruments, specially designed for two different particle size ranges:

- COULTER® LS™ 230 Enhanced Laser Diffraction Particle Size Analyzer.
- COULTER® N4 Plus™

2.3.2.1 COULTER® LS™ 230

The basis of COULTER® LS™ 230 is the Laser Diffraction method, which relies on the optical principle that small particles in the path of a light beam scatter the light in a characteristic, symmetrical pattern that can be viewed on a screen. The distribution of the particle sizes can then be deduced by studying a certain pattern of the scattered light intensity ("flux pattern") as a function of the angle between the incident beam and the reflected light [**Fig. 2.5**]. The simplest flux pattern, for a dispersion of equi-sized spheres, consists of a central bright spot (known as the airy disk), surrounded by concentric dark and bright rings whose intensity diminishes further from the center of the pattern, i.e. at higher scattering angles. The scattering angle, at which the first dark ring, or the diffraction minimum, occurs depends on the size of the particles, in that the smaller the particle the higher is the angle of the first dark ring (or, alternatively, the larger is the size of the airy disk).

These flux patterns obey the rule of linear superposition. In other words, the pattern from a mixture of two (or more) monomodal dispersions of the particles can be constructed by adding the intensity functions of the constituent particles in the mixture. The goal of a Laser Diffraction particle size measurement is to measure the flux pattern accurately

enough to determine the distribution of particle sizes in suspensions. This instrument is capable of measuring particle sizes ranging from 0.04μm to 2000μm in a single scan, using 116 size channels. A brief description of the various steps for performing the measurements on this device is summarized in **Appendix 2B.**

2.3.2.2 COULTER® N4 Plus™

The COULTER® N4 Plus™ Submicron Particle Size Analyzer is based on the Photo-Correlation Spectroscopy method, which is also referred to as dynamic light scattering or quasi-elastic light scattering. This technique is applicable to particles, suspended in a liquid, which are in a state of random motion due to Brownian fluctuations (i.e., particles generally 2-3μm in diameter or smaller). The instantaneous velocity of these particles is inversely proportional to the particle size (i.e., the smaller the particle, the faster they move, or diffuse) and can be detected by analyzing the time dependency of the light intensity fluctuations scattered from the particles when they are illuminated with a laser beam. The analyzer has one 80-channel multi-tau correlator (the hard-wired computation circuit which characterizes the rate of fluctuations in the scattered light intensity) and optimizes the resolution across the dynamic range of the instrument. This instrument is capable of measuring particle sizes ranging from 3nm to 3μm.

We used this instrument for measuring of the size distribution of the nanoparticles [**Appendix 5A**], synthesized in our laboratory. A brief description of the various steps required for performing the measurements on this device is given in **Appendix 2C.**

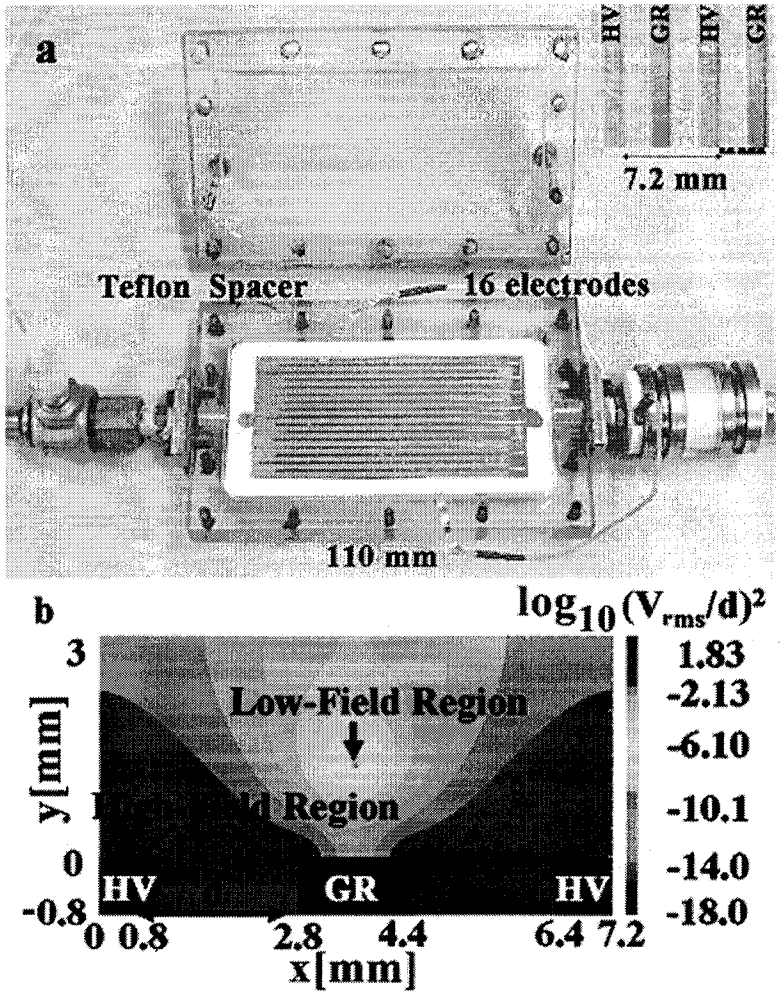

Figure 2.1: (a) Dielectrophoretic chamber, having 16 electrodes and Teflon spacer used to maintain gap of 3mm above the electrodes with the inset showing the top view of the 4 electrodes along with their dimensions (HV and GR refer to the high-voltage and the grounded electrode respectively). (b) The distribution of the square of the field strength, E^2 (expressed in units of V^2_{rms}/d^2 on a base 10 logarithmic scale) for a pair of electrodes. Half of the high-voltage electrodes are on the left ($0 \leq x \leq 0.8$) and on the right ($6.4 \leq x \leq 7.2$) while the grounded electrode is in the middle ($2.8 \leq x \leq 4.4$). The top (y=3.0) is also grounded.

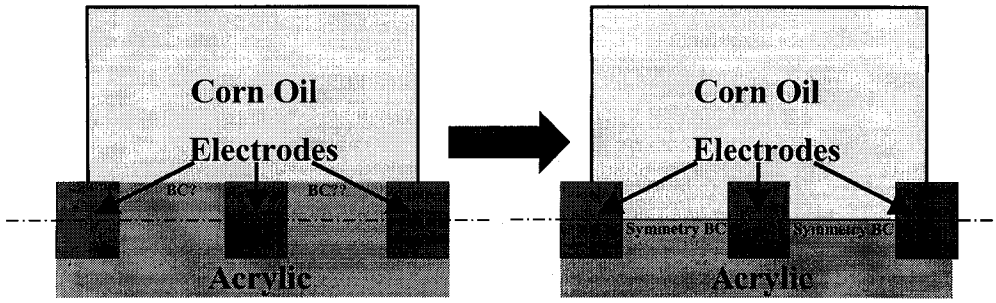

Figure 2.2: The transformation used to apply a symmetry boundary condition within the region located between the adjacent edges of the neighboring electrodes.

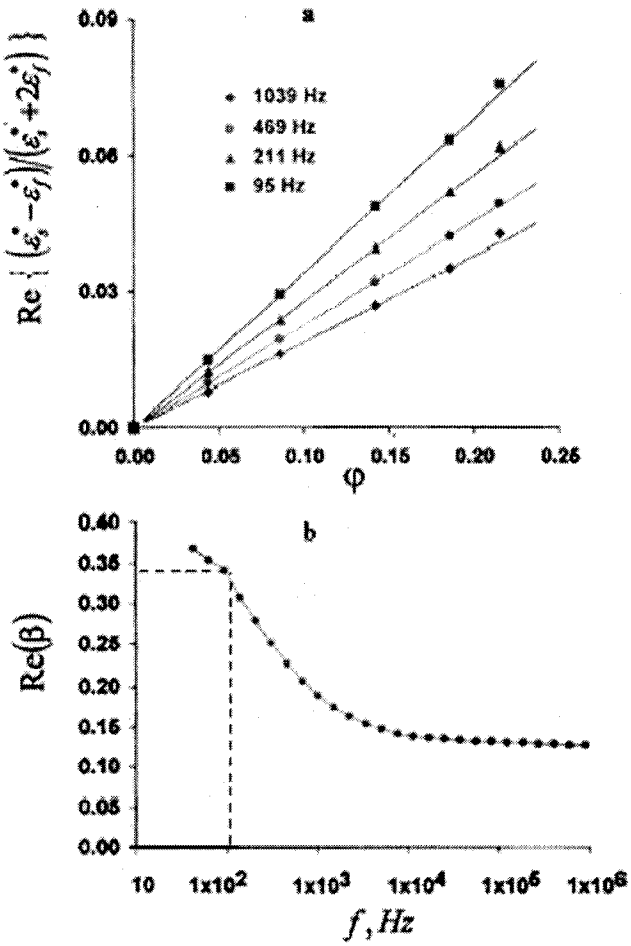

Figure. 2.3: The relative particle polarization for suspension of aluminum oxide particles in corn oil; (a) shows the dependence of the real part of $\left(\varepsilon_s^* - \varepsilon_f^*\right)/\left(\varepsilon_s^* + 2\varepsilon_f^*\right)$, measured by using the BDS 80 dielectric spectrometer, on the particle volume concentration, c ;(b) shows the frequency dependence of the real part of the particle polarization, $\mathrm{Re}(\beta)$, which inturn was obtained by taking the slope of the straight line in (a). [Data taken from Ref. 4]

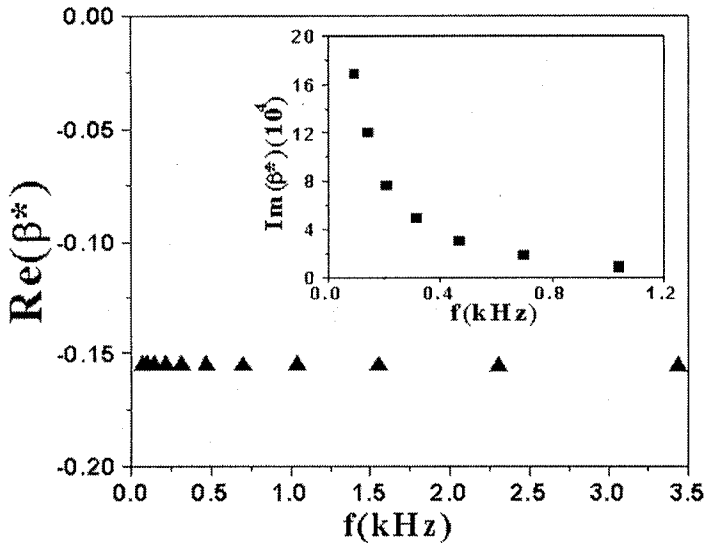

Figure 2.4: The frequency dependence of the particle polarizability for a suspension of polyolefin particles in corn oil. The particle concentration ranged from 1% to 15%(v/v).

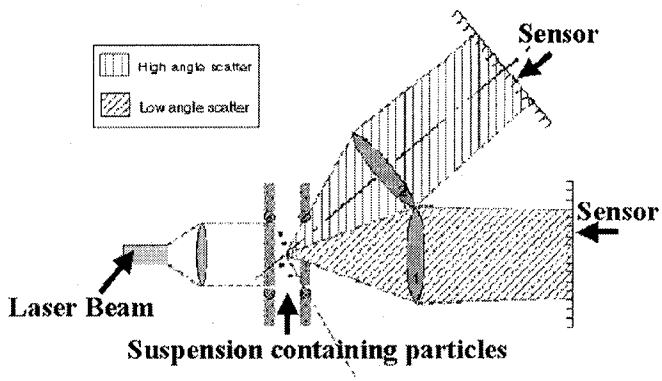

Figure 2.5: Schematic showing the working principle of the Laser Diffraction method (Image taken from the Beckman Coulter website [**23**]).

Chapter 3

Theoretical Model for non-Dilute Suspensions

3.1 Introduction

In this chapter we shall present the basic features of the theoretical model for studying the behavior of concentrated suspensions. In earlier studies [**4-6**], a single particle model was used for predicting the behavior of dilute suspensions which was based on the assumption that the electric field distribution is unaffected by the presence of the particles and that the particles could overlap. Consequently, this earlier model, which is briefly described below in Section 3.2.3 of this Chapter and then used in Section 4.4 of Chapter 4, is appropriate only for infinitely dilute suspensions and is unable to predict the final morphology of the particle distribution once the particles accumulate in the high or low field regions.

But, given that the primary aim of this thesis is to study the behavior of non-dilute suspensions, it becomes necessary to seek a model which would be expected to apply, at least approximately, beyond the dilute regime. To this end, we return to a model, developed by Khusid and Acrivos and referred to henceforth as the "Electrohydrodynamic Model", which is based on a generalization of their previous

theory for the thermodynamics of the field-induced phase transition in suspensions of polarized particles [**1-3**].

3.2 The Electrohydrodynamic Model

3.2.1 Thermodynamics and The Phase Diagram

In [**Refs. 1-3**], Khusid and Acrivos described a theory for the free energy of a suspension of polarized spherical particles subject to an ac electric field, $\mathbf{E} = \mathbf{E}_0(r)\cos\omega t$, based on the Maxwell-Wagner model for the interfacial polarization of a particle and the Lorentz-Lorenz model for the local field acting on a particle. This theory yields the following expressions for the chemical potential, μ_p, and the osmotic pressure, Π_p, of the particles averaged over the period of the field oscillations under conditions when the $|\mathrm{Im}(\beta)| << |\mathrm{Re}(\beta)|$ (which is the case in our experiments):

$$\mu_p = \frac{k_B T}{v_p}\frac{df_0}{dc} - \varepsilon_0\left(\frac{\partial\varepsilon'_s}{\partial c}\right)_{\omega t_c}\left\langle\frac{\mathbf{E}^2}{2}\right\rangle \qquad \text{with} \quad f_0 = c\ln\frac{c}{e} + c\int_0^c\frac{Z(c)-1}{c}dc$$

$$\Pi_p = \frac{k_B T}{v_p}cZ + \varepsilon_0\left[\varepsilon'_s - c\left(\frac{\partial\varepsilon'_s}{\partial c}\right)_{\omega t_c}\right]\left\langle\frac{\mathbf{E}^2}{2}\right\rangle, \quad \text{with} \quad \left(\frac{\partial\varepsilon'_s}{\partial c}\right)_{\omega t_c} \approx \frac{3\varepsilon_f\beta}{[1-c\beta]^2} \qquad (3.1)$$

where $\beta = \mathrm{Re}(\beta^*)$, $\varepsilon_f = \mathrm{Re}(\varepsilon_f^*)$, $k_B T$ is the thermal energy, c is the particle volume fraction, c_m is the concentration of the spheres at random close packing, and $(\partial\varepsilon'_s/\partial c)_{\omega t_c}$ is the derivative of the real part of the complex dielectric permittivity of the suspension, $\varepsilon_s^* = \varepsilon'_s(\omega,c) - i\varepsilon''_s(\omega,c)$, taken at a constant value of ωt_c with t_c being the relaxation time of the dielectric phenomena [**Ref. 3**]. Also, the dependence of ε_s^* on c is assumed to be given by the Maxwell-Wagner expression [Eq. (2.1)]. The first term in Eqs. (3.1)

refers to the free energy and the osmotic pressure of the particles in the absence of the electric field whereas the other represents the contribution due to the field.

The concentration dependence of the compressibility factor is described by the Carnahan-Starling equation for a suspension of spheres in the disordered state [**Ref. 19**] where $Z = \left(1 + c + c^2 - c^3\right)/(1-c)^3$ when $0 < c \le 0.5$ and $Z \approx A/(c_m - c)$ for $0.5 < c \le c_m$. The value of the constant A was determined by requiring that the function, Z(c) be continuous at $c = 0.5$. A=1.85 if c_m is set equal to 0.64. Making use of the expressions for Z(c) given above yields:

$f_0' \approx \ln c + 8c + 15c^2$ for $c \to 0$ and

$$f_0' \approx \frac{A}{c_m - c} - \frac{A}{c_m}\ln(c_m - c) + \chi(c) \text{ for } c \to c_m$$

$$\text{with } \chi = \frac{A}{c_m}\ln[2c(c_m - 0.5)] - 1\ln 2e + \int_0^{0.5}\frac{Z-1}{c}dc, \qquad (3.2)$$

Based on the expressions for the chemical potential and for the osmotic pressure given by Eqs. (3.1), a phase diagram for a suspension subject to a spatially uniform ac electric field can be constructed for "the particle concentration, c, vs. the relative field strength, $\lambda = \varepsilon_0\varepsilon_f\langle E^2\rangle v_p/k_BT$". A characteristic plot for such a diagram is shown in Fig. 3.1 for $\beta = 0.1$. This phase diagram appears to be similar to "the concentration vs. temperature" phase diagrams for the first-order phase separation in a mixture of two liquids which are completely miscible only above a certain temperature [**Refs. 1, 3**]. This phase diagram can be subdivided into two regions: a single-phase region and a two-phase region. Within the single-phase region (shown by the shaded area in Fig. 3.1), the particles are randomly distributed but, for $\Lambda > \Lambda_{cr}$, this random arrangement becomes unstable when

$\partial\mu_p/\partial c = 0$, which represents the spinodal curve in the phase diagram (shown by curve 2 in Fig. 3.1) with M and U denoting the metastable and unstable domains, respectively. A field-induced separation is thereby predicted to result leading to the creation of a two-phase region with phases 1 and 2 consisting, respectively, of dilute and concentrated suspensions. The critical point on the spinodal curve, c_{cr} and Λ_{cr}, which is located on the inflection point of μ_p as a function of c, is determined from equations $Z + cZ' = \frac{\Lambda c}{(1-\beta c)^3}$ and $2Z' + cZ'' = \frac{\Lambda(1+2\beta c)}{(1-\beta c)^4}$, where $\Lambda = 3\beta^2\lambda$. With increasing β from –0.5 to 1, $\Lambda_{cr}(\beta)$ decreases from 25.24 to 11.7 whereas $c_{cr}(\beta)$ increases from 0.11 to 0.27 with $c_{cr}(0) = 0.13$ and $\Lambda_{cr}(0) = 22.2$ for $\beta = 0$ [**3**]. Moreover, on the coexistence curve in the phase diagram (shown by curve 1 in Fig. 3.1), the corresponding values of the two chemical potentials, μ_p, and of the two osmotic pressures, Π_p, of the particles in the coexisting phases having particle concentrations, c_1 and c_2, respectively, are equal:

$$\mu_p(c_1) = \mu_p(c_2) \text{ and } \Pi_p(c_1) = \Pi_p(c_2) \tag{3.3}$$

By taking the asymptotic form of Eqs. (3.1) and (3.3) as $\beta^2\lambda \to \infty$, one can deduce, for the particle chemical potential in the two-phase region,

$$\mu_p \approx \varepsilon_0\varepsilon_f\langle E^2\rangle\left[-\frac{3\beta}{2(1-c_m\beta)} + \frac{A}{c_m\lambda} - \frac{A}{c_m\lambda}\ln\frac{2(1-c_m\beta)^2}{3c_m\beta^2\lambda}\right], \text{ for } c_2(\lambda) > c > c_1(\lambda), \tag{3.4}$$

while, within the single-phase region,

$$\mu_p \approx \varepsilon_0\varepsilon_f\langle E^2\rangle\left[-\frac{3\beta}{2(1-c\beta)^2} + \frac{1}{\lambda}(\ln c + 8c)\right] \text{ for } c < c_1(\lambda), \tag{3.5}$$

and

$$\mu_p \approx \varepsilon_0 \varepsilon_f \langle E^2 \rangle \left[-\frac{3\beta}{2(1-c\beta)^2} + \frac{1}{\lambda}\left(\frac{A}{c_m - c} - \frac{A}{c_m} \ln(c_m - c) \right) \right] \quad \text{for } c > c_2(\lambda), \tag{3.6}$$

where, along the coexistence curve,

$$\ln c_1 \approx -\frac{3c_m\beta^2\lambda}{2(1-c_m\beta)} - \frac{A}{c_m} \ln \frac{2(1-c_m\beta)^2}{3c_m\beta^2\lambda} + \frac{A}{c_m} + \chi(c_m) + \ldots\ldots$$

$$c_2 \approx c_m - \frac{2A(1-c_m\beta)^2}{3c_m\beta^2\lambda} - \frac{4A^2(1-c_m\beta)^3(1+c_m\beta)}{9c_m^2\beta^4\lambda^2} + \ldots\ldots$$

The detailed derivation of these asymptotic forms is provided in **Appendix 3A**. The phase diagram described above provides a consistent interpretation of the experimental data on the field-induced aggregation phenomena in electro-rheological fluids and aqueous suspensions [**Refs. 1, 3**]. To explore the effect of spatially non-uniform fields on the particle distribution, Khusid and Acrivos [**Ref. 2**] considered a quasi-equilibrium condition for the spatial distribution of the particle concentration caused by dielectrophoresis. This can be achieved when the chemical potential of a particle becomes independent of position so that

$$\nabla \mu_p \left[c(\mathbf{r}), \langle \mathbf{E}^2(\mathbf{r}) \rangle \right] = 0 \tag{3.7}$$

Equation (3.7) represents c as a function of $\langle \mathbf{E}^2 \rangle$ along the curve $\mu_p = \text{const}$ on the suspension phase diagram, Fig. 3.1. It was shown in [**Ref. 2**] that, under certain conditions, this curve crosses the coexistence curve, Eqs. (3.3) in which case, dielectrophoresis is accompanied by a phase separation leading to an abrupt change in the spatial particle concentration distribution and, as a result, to the formation of a concentration front across which the particle concentration is discontinuous. Using the continuity equation for the particles, Eqs. (3.11), the continuity equation at the front becomes:

$$\left[c^{-}\left(\mathbf{v}^{-}-\mathbf{U}\right)+\mathbf{j}_{p}^{-}\right]\cdot\mathbf{n}=\left[c^{+}\left(\mathbf{v}^{+}-\mathbf{U}\right)+\mathbf{j}_{p}^{+}\right]\cdot\mathbf{n}\,, \tag{3.8}$$

where $\mathbf{U}$ is the front velocity, $\mathbf{j}_p$ is the particle flux in the reference frame moving with the suspension, $\mathbf{v}$ is the bulk velocity of the suspension, $\mathbf{n}$ is a vector normal to the concentration front, and the superscripts "+" and "–" denote, respectively, the values before and after the discontinuity.

Now, to understand the front formation and its propagation kinetics, the thermodynamic theory presented above needs to be combined with the field and flow equations.

3.2.2 Electro-Hydrodynamic Model

The theory encompasses the field and flow equations for both the single-phase as well as the two-phase states of a suspension. The single-phase or two-phase equations should be used depending on whether the point representing the local values of the particle concentration and the electric field in the suspension phase diagram is located below or above the coexistence curve [Fig. 3.1]. First, let us consider the equations for the one-phase region for which $\partial\mu_p/\partial c>0$. Since the time scale of the hydrodynamic phenomena is significantly larger than the period of the field oscillations, we can average the equations for the suspension flow over the field oscillations. Next, because of the small suspension velocity, we can neglect any difference between the electromagnetic fields in the laboratory system and in the instantaneous reference system moving with the suspension. Furthermore, we limit the analysis to the case when any magnetic effects associated with a time varying electric field are negligible. Under these conditions, we can write the quasi-steady electrodynamic equations [**Refs. 24, 25**] for the suspension, averaged over the field oscillations, in terms of the complex Fourier components of the electric field, $\mathbf{E}_{\omega}^{*}(\mathbf{r})$, the electric potential, φ_{ω}^{*}, and the electric displacement, $\mathbf{D}_{\omega}^{*}(\mathbf{r})$, as:

$$\nabla \cdot \mathbf{D}^*_\omega(\mathbf{r}) = 0,\ \nabla \times \mathbf{E}^*_\omega(\mathbf{r}) = 0 \quad \text{with} \quad \mathbf{D}^*_\omega = \varepsilon_0\left[\varepsilon'_s(\omega, c) - i\varepsilon''_s(\omega, c)\right]\mathbf{E}^*_\omega, \tag{3.9}$$

$$\text{or } \nabla \cdot \left[\varepsilon^*_s(\omega, c)\nabla\varphi^*_\omega\right] = 0 \qquad \text{with} \quad \mathbf{E}^*_\omega = -\nabla\varphi^*_\omega \tag{3.10}$$

In addition, we have for the hydrodynamic, continuity, and mass conservation equations:

$$\nabla \cdot \mathbf{v} = 0 \tag{3.11a}$$

$$\rho_s\left(\frac{\partial \mathbf{v}}{\partial t} + \mathbf{v}\cdot\nabla\mathbf{v}\right) = -\nabla p + \nabla\cdot\boldsymbol{\sigma}^{vis} - c\nabla\mu_p + c\left(\rho_p - \rho_f\right)\mathbf{g} \tag{3.11b}$$

$$\frac{\partial c}{\partial t} + \nabla\cdot\left(c\mathbf{v} + \mathbf{j}_p\right) = 0 \tag{3.11c}$$

where $\mathbf{v}$ is the bulk velocity of the suspension, $\rho_s = (1-c)\rho_f + c\rho_p$ is the suspension density with ρ_p and ρ_f being the densities of the particles and of the fluid, $\mathbf{g}$ is the gravitational acceleration, p is the pressure, $\boldsymbol{\sigma}^{vis}$ is the viscous stress tensor, and $\mathbf{j}_p$ is the particle flux in the reference system moving with the suspension. For the concentration dependence of ε^*_s, Eq. (2.1) was used in which the frequency dependence of $\beta(\omega)$ was taken from the measurements, at low electric fields, using the dielectric spectroscopy technique described in Chapter 2. The spatial variation of $\varepsilon^*_s(\omega, c)$ in Eq. (3.10) is caused by the spatial variation of the particle concentration, c, due to their motion following the application of a spatially non-uniform ac electric field. The fourth term on the right-hand side of Eq. (3.11b) refers to the bulk gravity force which vanishes for neutrally buoyant particles, whereas the term $-c\nabla\mu_p$, with μ_p being given by Eq. (3.1) with $\langle \mathbf{E}^2 \rangle = \frac{1}{2}\left|\mathbf{E}^*_\omega(\mathbf{r})\right|^2$, represents the bulk electric force exerted on the suspension by the applied ac field. This approximation for the bulk electric force is appropriate only when $|\mathrm{Im}(\beta)| << |\mathrm{Re}(\beta)|$, which is the case with our suspension of polyolefin particles in corn oil

shown by Fig. 1.3. For a spatially uniform particle concentration, the bulk electric force equals the total force exerted on the particles per unit volume of the suspension, so that, on account of Eq. (3.1):

$$-c\nabla\mu_p\big|_{c=const} = n\mathbf{F}_{dep} \qquad \text{with} \quad \mathbf{F}_{dep} = \frac{\varepsilon_0 v_p}{2}\left(\frac{\partial\varepsilon_s'}{\partial c}\right)_{\omega t_c}\nabla\langle\mathbf{E}^2\rangle, \tag{3.12}$$

where n defines the number density of the particles and $\mathbf{F}_{dep}$ is the dielectrophoretic force exerted on a single particle in a suspension. Since, from the Maxwell-Wagner expression [Eq. (2.1)], $(\partial\varepsilon_s'/\partial c)_{\omega t_c} \to 3\varepsilon_f \mathrm{Re}(\beta)$ for $c \to 0$, Eq. (3.12) for $\mathbf{F}_{dep}$ generalizes the expression, Eq. (1.17), for the dielectrophoretic force acting on a test particle in the suspension by accounting, in an approximate way, for the effect of the other particles on the coefficient multiplying the gradient of the magnitude of the applied field.

For calculation purposes, the analysis developed by Khusid and Acrivos was limited to the specific case of low particle Reynolds numbers and relatively high particle Peclet numbers associated with a weak Brownian diffusion of the particles, which is relevant to the experiments referred to in Chapter 5. The suspension was treated as an effective Newtonian fluid with a concentration dependent viscosity [**Ref. 26**]. Under these conditions, the equations for the effective viscous stress and the particle flux become:

$$\sigma_{ij}^{vis} = \eta_s(c)\left(\frac{\partial v_i}{\partial x_j} + \frac{\partial v_j}{\partial x_i}\right) \qquad \text{and} \quad \mathbf{j}_p = \frac{c(1-c)^2 v_p}{6\pi a \eta_s(c)}\left[-\nabla\mu_p + (\rho_p - \rho_f)\mathbf{g}\right] \tag{3.13}$$

where $\eta_s = \eta_f \hat{\eta}(c)$ is the suspension viscosity, with η_f being the suspending fluid viscosity and $\hat{\eta} = \left(1 + \frac{1.5c}{1 - c/c_m}\right)^2$ the Leighton-Acrivos expression for the concentration dependence of the suspension viscosity [**Ref. 26**]. Also, the factor $(1-c)^2$ in the

expression for the particle flux represents the hindrance function [**Ref. 26**]. The hydrodynamic equations, Eqs. (3.11) and (3.13), are coupled with the electrodynamic equations, Eqs. (3.9) and (3.10), through the field dependence of μ_p for the former and the concentration dependence of ε_s^* for the latter and need to be solved simultaneously.

We next turn to the task of modifying the electro-hydrodynamic model, Eqs. (3.1), (3.9)-(13), in order to treat the two-phase region of the suspension phase diagram, Fig. 3.1. Recall from Chapter 3, that, since $\left(\partial\mu_p/\partial c\right)_E < 0$, these equations are unstable within the unstable domain, U, in the phase diagram (Fig. 3.1). But under special conditions, when the field-induced phase separation occurs significantly faster than typical hydrodynamic phenomena, a quasi-equilibrium approximation for the local values of the particle concentration and of the electric field in the two-phase region can be employed. In that case, the value of the chemical potential in both phases remains the same and is specified by the coexistence curve, Eqs. (3.3), in the phase diagram as a function of λ, i.e., $\mu_p = \mu_p(\lambda)$. In addition, the particle concentrations in the two phases, c_1 and c_2, will be specified by the coexistence curve, Eqs. (3.3), as functions of λ, while the volume fraction of the high concentration phase, ψ, is computed using the lever rule, $c_2\psi + c_1(1-\psi) = c$, as a function of c and λ. Within this approximation, the two-phase state of the suspension could be viewed as a "mushy" zone. For simplicity, the complex dielectric permittivity, the viscosity, and the hindrance function for this zone were assumed to be determined only by the total particle concentration, c, through the use of the same functions as those for the one-phase region, even though they are in fact functions (unfortunately, unknown at present) of both c and ψ. Under these conditions,

the two-phase model consists of Eqs. (3.9)-(3.11) and (3.13) in which the chemical potential is specified as a function of the field strength, $\mu_p = \mu_p(\lambda)$, through the solution of Eqs. (3.3).

3.2.3 The Single-Particle Model

For the limiting case of a dilute suspension, for which $c \to 0$ and $\partial f_0/\partial c \to 1/c$, Eqs. (3.9)-(3.11) reduce to the field and flow equations for the suspending fluid while Eqs. (3.1), (3.11) and (3.13) yield:

$$\frac{\partial c}{\partial t} + \nabla \cdot [c(\mathbf{v} + \mathbf{u}_e)] = D_B \nabla^2 c \text{ with } \mathbf{u}_e = \frac{v_p}{6\pi a \eta_f}\left[\frac{3}{2}\varepsilon_0 \varepsilon_f \, \mathrm{Re}(\beta) \nabla \langle \mathbf{E}^2 \rangle + (\rho_p - \rho_f)\mathbf{g}\right], \quad (3.14)$$

where $\mathbf{u}_e$ is the velocity of a particle relative to the suspending fluid under the action of the dielectrophoretic, Eq. (1.17), and gravity forces, and $D_B = k_B T/6\pi a \eta_f$ is the particle Brownian diffusion coefficient. When Brownian effects are insignificant, Eq. (3.14) reduces to the single-particle model [**4-6**]

$$\frac{\partial c}{\partial t} + \nabla \cdot [c(\mathbf{v} + \mathbf{u}_e)] = 0, \quad (3.15)$$

The predictions of Eq. (3.15) with Eq. (3.14) for u_e were found to be consistent with the experimental data for dilute suspensions of negatively and positively polarized particles subject to a high-gradient electric field (~kV/mm) and a shear flow even though the value of the particle polarizability, β, was measured at low-field strengths (~V/mm).

Another limiting case is that of the quasi-equilibrium state of a suspension of neutrally buoyant particles subject to a spatially nonuniform ac field, for which Eqs. (3.1), (3.11)–(3.13) yield $\mathbf{v} = 0$ and $\nabla p = 0$, while the particle distribution satisfies Eq. (3.7).

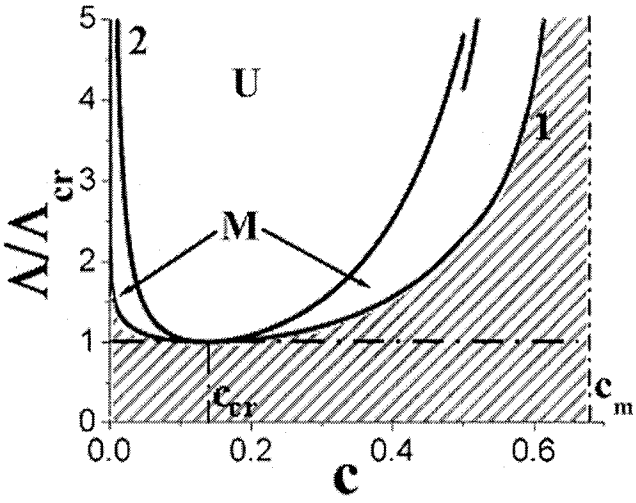

Figure 3.1: The phase diagram of the "particle concentration vs. the field strength" of suspensions subjected to electric fields for $\beta = 0.1$: the metastable and unstable domains are denoted by M and U, respectively, $\Lambda = 3\beta^2\lambda$ where $\lambda = \varepsilon_0\varepsilon_f\langle E^2\rangle v_p / k_B T$ is the relative strength of the field, and c is the particle volume concentration [**Ref. 3**]; 1 and 2 are respectively, the coexistence and spinodal curves. The Single-phase region is shown by the shaded area.

Chapter 4

Positive dielectrophoresis and effect of clinorotation on suspensions of heavy particles

4.1 Introduction

In this Chapter, we shall present experimental results which illustrate the influence of a relatively weak, rotating gravity force on field-induced particle interactions within a range of parameters typical of clinostats. The experiments, in which a dilute suspension of heavy, positively polarized spheres was exposed to a high-gradient strong ac electric field, were conducted in microgravity (aboard NASA's research aircraft KC-135) as well in a ground-based environment in the electric chamber described in Chapter 2. The latter will be referred to as a "clinostat" due to the fact that it was slowly rotated around its horizontal axis to prevent the particles from settling. Although one might have expected, that by rotating the chamber about it axis, one should be able to simulate, on average, microgravity conditions, this experimental study showed that this is not so as far as the morphology of the aggregation pattern is concerned. In this work, the experiments under microgravity conditions were carried out by Dr. Nikolai Markarian, Mike Yeksel, Prof. Boris Khusid, and Tin Padeta, whereas my contribution consisted in performing all the ground based experiments, as well as quantifying the experimental data and doing the theoretical

modeling. This combined team effort lead to a publication in the Physics of Fluids, **16,** 1826(2004) [**27**].

4.2 Experimental Procedures

4.2.1 Materials

The suspension consisted of a fraction of sieved aluminum oxide spherical particles (AL-604, 99.9%, AEE, NJ) suspended in Mazola corn oil. The particle size distribution on a number basis was measured with the Beckman-Coulter LS 230 device described in Chapter 2. The average diameter of the particles was 89.6 μm, and 50% of the particles had diameters between 69 and 107 μm. The particles (ρ_p= 3.75 g/cm^3) were dispersed in corn oil ($\rho_f = 0.92$ g/cm^3, viscosity $\eta_f = 59.7$cp, and dielectric constant $\varepsilon_f = 2.87$ at 23^{0}C). The measured complex permittivities using the BDS 80 Dielectric Spectrometer are shown in [**Fig. 2.2**]. Due to the time constraint under microgravity (only 4 flights were available with each flight having 40 microgravity parabolas each lasting ~20sec followed by ~40sec under ~2g before coming back to microgravity again), all the microgravity experiments were conducted by exposing the suspension, having a fixed particle volume fraction, $c = 2 \cdot 10^{-3}$, to a fixed magnitude and frequency of the applied ac electric field. We chose the values of the field strength, 4kV, and for the frequency, 100Hz, so as to have the characteristic dielectrophoretic time be smaller than 20sec which is the duration of each experiment under microgravity. The value of the relative particle polarization, Re (β), at this frequency was measured to be 0.34, showing the positive dielectrophoretic behavior of this suspension under electric field. The details of the suspension properties have been described in **Ref. 5**.

4.2.2 Experimental Setup and Working Conditions

The experimental setup constituting the electric chamber [**Fig. 2.1(a)**] is shown in [**Fig. 4.1(a)**]. During this study, since the particles were heavier than the suspending fluid and therefore to diminish the effects of the gravitational force, the chamber was rotated about its horizontal axis using a step motor with a step controller (SmartStep, IDC, CA), which was programmed to bring the channel instantaneously at preset positions. The details about the workings of the device have been described in **Ref. 5**. Energizing the chamber with an ac voltage of several kV generated a spatially nonuniform field of order kV/mm with the regions of the highest field strength located at the edges of the energized electrodes [**Figs. 4.1(b)** and **(c)**] and that of its lowest strength above the centers of the grounded electrodes near the midplane of the channel [**Fig. 2.1(b)**]. An ac voltage of $V_{rms} = 4$ kV (root mean square) and 100 Hz was used to energize the electrodes giving for the dielectrophoretic time [**5**] $\tau_d = 3d^4\eta_f / a^2\varepsilon_0\varepsilon_f |Re(\beta)| V_{rms}^2 = 10.3s$, where ε_0 is the vacuum permittivity and $d = 2mm$ is the gap between adjacent electrode edges. τ_d is a measure of the time required for a particle to move over a length of d under the action of a dielectrophoretic force [**5**]. In all the experiments, with the flowing suspension, the flow rate through the channel was set at 20 ml/min giving for the shear rate at the wall $\dot{\gamma}_w = 3.7s^{-1}$ and for the average fluid residence time $T = L/U_a$ =59.4s, where $L = 11cm$ is the electrode length and U_a is the average fluid velocity. Under these conditions: (a), the Reynolds numbers for the fluid flow and for the relative particle motion are $Re_f \sim 0.08$ and $Re_p \sim 10^{-4}$, respectively; (b), the ratios between the gravity, F_g, and dielectrophoretic, F_{dep}, forces acting on a particle and the dipolar force between two touching particles, F_{dd}, are $F_g / F_{dep} \sim G = 2(\rho_p - \rho_f) g d^3 / 3\varepsilon_0\varepsilon_f |Re(\beta)| V_{rms}^2 = 1.07$ and $F_g / F_{dd} \sim S = 8aG/3|Re(\beta)|d = 0.19$; and

(c), the Mason number [**Ref. 5**], which represents a ratio between the shear stress at the wall and the interparticle dipolar interactions, is $Ma = 8\eta_f \dot{\gamma}_w d^2 / 3\varepsilon_0 \varepsilon_f V_{rms}^2 \, Re(\beta)^2 = 0.05$.

4.2.3 Image Analysis

The images were analyzed using the VISILOG-5 (Noesis, Inc.) software which collects the readings of the gray level (GL) of individual pixels, defined as the relative brightness with a value of the GL ranging from 0 (black) to 255 (white), over a selected rectangular box on an image and calculates the average brightness for this box. The relative change of the GL, $I = [GL(x,t) - GL_0] / \sum_{x'} [GL(x',t) - GL_0]$ with GL_0 being the value for the area without the particles, taken on a set of consecutive images was shown [**5**] to provide an estimate of the variation in the particle accumulation at the location x with time t.

4.3 Experimental Data

The microgravity experiments were performed aboard the aircraft KC-135 flying along a parabolic trajectory that provides a zero-gravity period for approximately 25s followed by ~40s under a gravity of ~2g before returning to the zero-gravity conditions. The experiments were repeated during four flights, each providing about 40 parabolas. The chamber was loaded with a suspension before the flight and was kept rotating (4 rpm) with the suspension being cycled through the channel until the aircraft had reached the zero gravity part of the trajectory. Then the rotating chamber was brought into the position with its top facing the camera fixed above it [**Fig. 4.1**], the rotation was stopped, and the electrodes were energized while the suspension continued to be cycled through the channel. At the end of the zero gravity period, the chamber was de-energized and brought into rotation until the next round of zero gravity where, the same experiment was repeated. The observed aggregation patterns did not vary from parabola to

parabola, indicating that the combined rotation of the de-energized chamber and the cycling of the suspension was sufficient to re-suspend the segregated particles between the zero gravity periods. The photos were taken in the middle of the channel where the flow entrance and exit effects were less pronounced. The exposure of the flowing suspension to the electric field under zero gravity for 20s caused the particles to segregate mainly on the edges of the high-voltage electrodes forming long bristles directed along the electric field lines [**Fig. 4.2**]. In the ground-based experiments, the chamber was loaded with the suspension and maintained rotating at 4 rpm for about 30 min while the suspension was cycled through the channel. When the plane with the electrodes formed a certain angle with the vertical, the voltage was applied to the electrodes while the suspension continued to be cycled [**Fig. 4.2(e)**]. A photo of the middle part of the channel was taken when the chamber was passing through the horizontal position with its top facing the camera fixed above. We varied the angle of the chamber at which the voltage was applied so as to take photos of the structures formed on the electrode edges following the exposure of the suspension to the field for 5s, 10s, 15s, and 20s. Experiments under similar conditions were also conducted without cycling the suspension through the channel. Photos of the field-induced aggregation patterns and data on the average length of the growing bristles are presented in Fig. 4.2. As can be seen from Fig. 4.2, a relatively weak gravity force ($S = 0.19$) exerts an unexpectedly pronounced effect on the field-driven aggregation pattern driven by the interparticle interactions, whereas a slight change due to the presence of the flow is in line with expectations for $Ma = 0.05$ [**5**]. Specifically, the bristles formed in the ground-based experiments appear to be significantly shorter and tighter packed than those formed in microgravity [Figs. 4.2 (a) – 4.2(d)].

The flight experiments also indicated that ac dielectrophoresis provides a reliable method in microgravity for manipulating air bubbles trapped in suspensions. While filling the chamber with a suspension, a small population of air bubbles was trapped inside the channel and released during the flight along the parabolic trajectories. Following the application of the field, these bubbles were attracted toward the low field regions above the grounded electrodes by the negative dielectrophoretic force and then traveled along the channel with the flow [Fig. 4.2(f) and Fig. 4.2(g)]. The time required for the air bubbles to travel to the low field region, as predicted by the single-particle model for $\mathrm{Re}(\beta) \approx (1-\varepsilon_f)/(1+2\varepsilon_f) = -0.27$ and $a \sim 0.16\mathrm{mm}$, is consistent with the experimental observations.

To understand and compare the effects of the electric, gravity, and shear forces on the re-suspension of the particles (with and without flow), ground-based experiments were performed by stopping the chamber rotation when its top was horizontal facing the camera and maintaining it in this position for about 2 min to allow all the particles to settle. The surface concentration of the particles in the sediment formed on the channel bottom was rather small, $c_s = 3c\,H/4a = 0.1$ with $H = 3\mathrm{mm}$ being the channel height, giving $\sim 1/c_s^{1/2} = 3.2$ particle diameters for the average distance between the particle centers. Once the particles settled [Fig. 4.3(a)], the voltage was applied while the chamber was maintained in the same position. It was found that the distribution of the particles located between the electrodes remained essentially unaffected even if a flow of 20ml/min was applied for 2 min. Next, the energized chamber was brought into rotation. First, the rotation of the chamber caused the particles to re-suspend slightly and form chains spanning the gap between the electrodes similar to those formed in electrorheological fluids [**28**, **29**] under the action of a spatially uniform electric field. As the time progressed, the particles slowly drifted toward the high-voltage electrodes and formed bristle-like structures typical of positive

dielectrophoresis [Fig. 4.3(b) and 4.3(c)]. To estimate the kinetics of the particle redistribution, we tracked the value of $I(x,t)$ between the adjacent electrodes [Fig. 4.3(d)]. As can be seen from Fig. 4.3(d), most of the particles were re-suspended during the first revolution. The presence of the flow facilitates the particle re-suspension [Fig. 4.3(d)] and leads to the formation of longer bristles on the high-voltage electrodes [0.7 mm for Fig. 4.3(b) and 0.4 mm for Fig. 4.3(c)].

4.4 Simulation Results

To simulate the particle accumulation on the electrodes in line with our experimental conditions, we distributed 596 particles uniformly over the channel cross-section and computed their trajectories using the single-particle model, Eq. (3.15) [**4**], which neglects the effect of Brownian motion due to the large size of the particles [d_p~O (100μm)] used in experiments. As said earlier, this model assumes that the electric field distribution, shown in Chapter 2, is unaffected by the presence of the particles and that electro-hydrodynamic interactions between particles can be neglected, both being good approximations in dilute suspensions. One major assumption underlying this model is the possibility of particle overlapping which prevents this model from predicting the final morphology of the particle distribution once they accumulate in the high or low field regions.

To compute the relative particle velocity, u_e, Eq. (3.14) is presented as:

$$6\pi\eta_f R\vec{u} = 2\pi\varepsilon_m R^3\,\mathrm{Re}(\beta)\vec{\nabla}E^2{}_{rms} + \frac{4}{3}\pi(\rho_p - \rho_f)R^3 g\vec{e}(t) \qquad (4.1)$$

where η_f is the viscosity of the suspending medium, ρ_f and ρ_p are the densities of the fluid and the particle, respectively; $\vec{e}(t)$ is the rotating unit vector along the orientation of the gravity force. Then given that $\nabla E^2{}_{rms}$ is $O(V^2{}_{rms}/d^3)$, we obtain that, in a quiescent suspension, u is

$O(d/\tau_d)$ where, on account of Eq. (4.2), τ_d, the characteristic time of the dielectrophoresis, is given by [**4**]

$$\tau_d = \frac{3d^4\eta}{R^2\varepsilon_m V^2{}_{rms}|\mathrm{Re}(\beta)|} \tag{4.2}$$

Since the electric field configuration is two-dimensional, it affects only the components of the particle velocity along x and y directions. The field-induced dimensionless displacement **r**(t) of a particle being initially at $r_0(x_0, y_0)$ is thereby obtained by solving

$$\frac{dr}{dt} = u \qquad r|_{t=0} = r_0 \tag{4.3}$$

where t refers to the time $\hat{t}$ rendered dimensionless by τ_d. The particle motion was computed using an interpolation method from the software DIFFPACK, which provides the value of ∇E^2 at any point. The initial distribution of the particle locations was assumed to be random and the simulations were carried out by varying the number of particles until the results were insensitive to the choice of the number of particles.

For the case of a flowing suspension, since the fully developed flow is always perpendicular to the plane of the electric field lines, the velocity components in the x and y directions are the same as those in a quiescent fluid, although now the particles will be having an additional velocity component in the z direction (along the flow direction), where they will travel with the local fluid velocity. The particle velocity component in the z direction, u_z, is given by well-known expression for the fully developed velocity profile of a fluid flowing through a parallel-plate channel [**30**]

$$u_z = 6U_a \frac{y}{H}\left(1 - \frac{y}{H}\right) \tag{4.4}$$

where H, equal to 1.5 in our case, is the channel height rendered dimensionless with d, and U_a is the dimensionless average velocity $Q\tau_d / Ad$ with Q being the volumetric flow rate and A being the channel cross sectional area. So, using this model we can track the motion of individual particles.

The simulations were conducted both for a rotating gravity force as well as for zero gravity. The former were carried out starting from different initial chamber positions shown in [Fig. 4.2(e)], while for zero gravity, the chamber position was held fixed [Fig. 4.2(e)]. The simulation results, depicted in Fig. 4.2(e), demonstrate that in all cases the exposure of the particles to the electric field for 20 s (greater than τ_d but smaller than the average fluid residence time T=59.4s) is sufficient to collect about 85% of them on the electrodes and that the maximum computed length necessary for these particles to travel along the channel axis in order to reach the electrode edges was about 33 mm ($\sim 0.3L$). Moreover, the simulations with rotating gravity, indicate that the variation of the angle at the instant when the rotating chamber was energized, significantly affected the particle trajectories, as expected, since the gravity force was comparable with the dielectrophoretic force for the ground-based experiments ($G = 1.07$). Also, as expected, the particle trajectories were significantly different for a rotating chamber (under gravity) and for zero gravity. Despite the variation in the particle trajectories, however, we found that in the ground-based experiments conducted under rotating gravity conditions, the aggregation patterns that formed on the electrode edges had similar features regardless of the orientation of the chamber at the instant when the electric field was applied. To characterize the field-induced particle accumulation on the electrodes under zero gravity, we tracked the variation of the GL between adjacent electrodes and then calculated $\sum_x I(x,t)$ over the layers formed by the particles close to the electrode edges which provide a quantitative measure of the relative change in the

particle amount in this region. As can be seen from Fig. 4.2(e), the predictions of the single-particle model for the total accumulation of the particles on the electrodes in the course of their heterogeneous aggregation under zero gravity are consistent with the experimental data even though the model does not contain any fitting parameters. For ground-based conditions, this fact was demonstrated in [**5**, **6**].

4.5 Summary and Conclusions

In conclusion, the data which we have presented demonstrate that dielectrophoresis provides a powerful method for the manipulation and concentration of particles in clinostats. However, clinorotation does not simulate the zero gravity morphology of the aggregation pattern because a relatively weak, rotating gravity force exerts a pronounced effect on the field-driven interparticle interactions. This fact may be explained as follows. The formation of bristle-like aggregates on the electrodes is caused by the interplay of the dielectrophoretic force that tends to confine the particles near the electrodes and strong dipolar forces between the nearby particles that either pull them together or push them away depending on their relative orientation. In a ground-based environment, the rotating gravity force causes those particles which are loosely connected to the growing bristles by the anisotropic electric forces to be released and to travel along the electrode edges thereby forming finer clusters and covering the edges more uniformly than in microgravity. In the same way, the rotating gravity causes the settled particles subjected to a strong field to re-suspend and then to rearrange themselves by first forming head-to-tail chains due to the prevailing interparticle anisotropic interactions and then drifting toward the electrode edges under the action of the dielectrophoretic force. The predictions of the single-particle model for the kinetics of the particle accumulation on the electrodes in the course of their

heterogeneous aggregation under zero gravity are shown to be consistent with the experimental data.

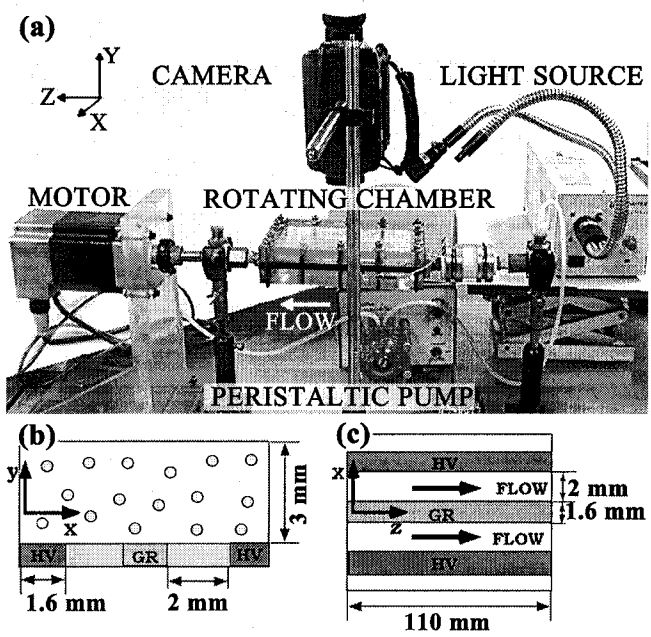

Figure 4.1: (a) Experimental setup. (b) Cross sectional and (c) top view of the channel (6 cm wide, 12 cm long, 3 mm high) showing 3 of 16 electrodes alternately connected to the high-voltage and ground outputs of a high-voltage amplifier. The channel top made of a glass coated with a conducting indium titanium oxide is grounded.

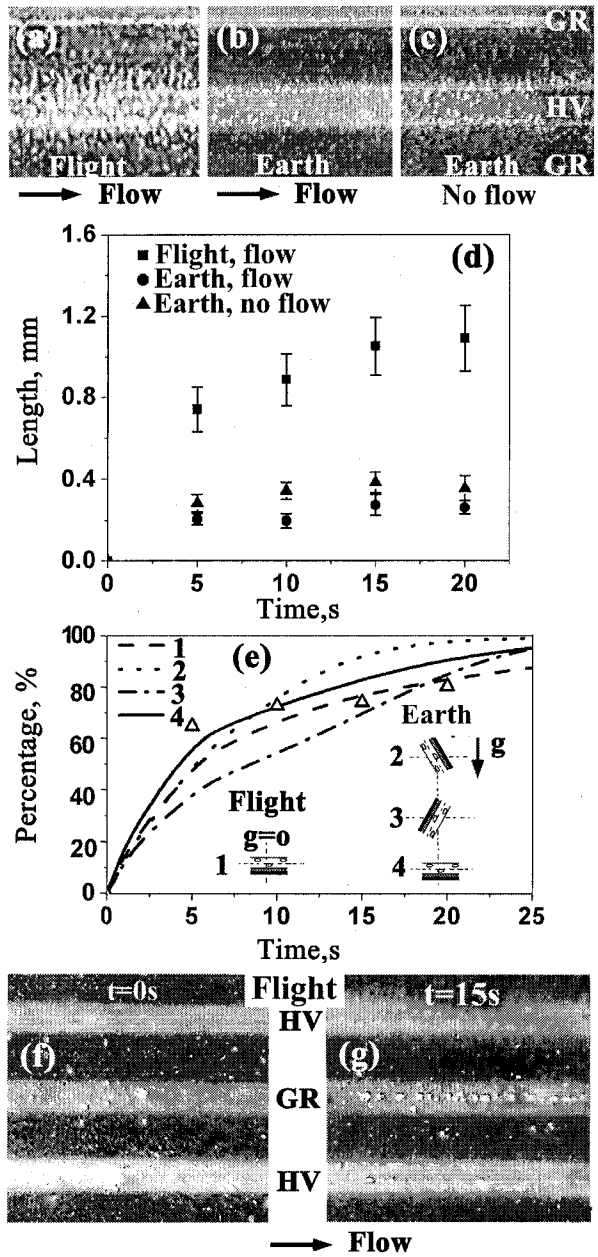

Figure 4.2: (a)-(c) Photos of the aggregation patterns formed during 10s and (d) the average length of the bristles growing on the high-voltage (HV) electrodes in the flight and in the ground-based experiments following exposure to the field; (e) The field-driven particle accumulation on the electrodes: the curves are computations for the flight and ground-based experiments for different positions of the chamber when the field was applied and the triangles are the experimental data for the flight; (f) Initial positions of the air bubbles and (g) their accumulation above the grounded electrode (GR) following a 15-s exposure to the field. The electrode width is 1.6 mm.

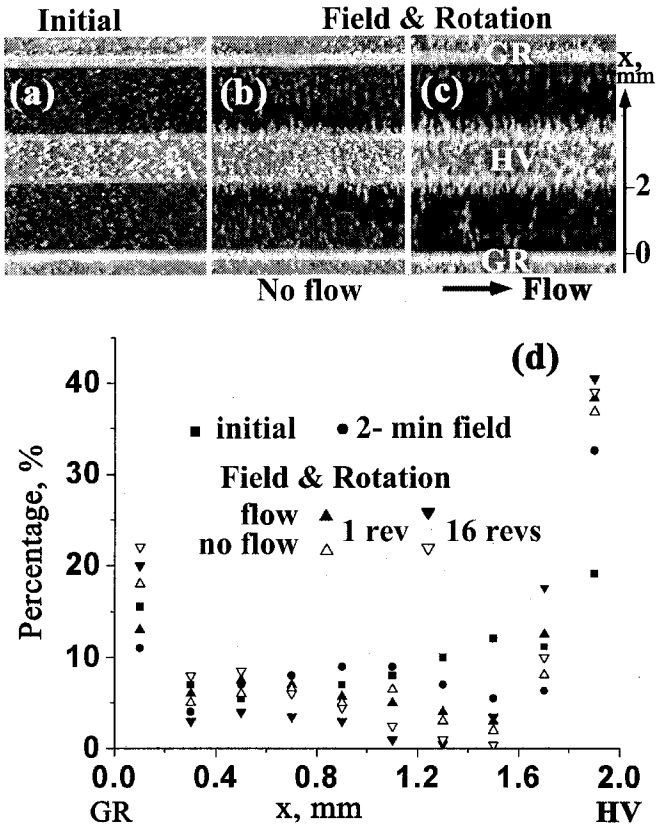

Figure 4.3: (a)-(c) show photos of the structures formed on the channel bottom: (a) shows the settled particles on the channel bottom achieved by keeping the chamber position horizontal for 2 min in the absence of the field; [(b) and (c)] show the structures formed after exposing the suspension shown in (a) to the electric field for 2 min (while keeping the chamber in the horizontal position) and then rotating the energized chamber for 16 revolutions. The average bristle length in (b) and (c) is 0.4 mm and 0.7 mm, respectively. The plot shown in (d) is the variation of $I(x,t)$ in the x direction between the edges of the adjacent grounded (GR) and high-voltage (HV) electrodes (with and without flow): (i) prior to the field application; (ii) following the exposure to the field for 2 min without rotation; (iii) after rotating the chamber, with the field on, for 1 revolution; and (iv) same as (iii) but after 16 revolutions. The electrode width is 1.6 mm.

Chapter 5

An experimental and theoretical study of combined negative dielectrophoresis and phase separation in concentrated suspensions subject to a high-gradient ac electric field

5.1 Introduction

In this Chapter, we focus our attention on investigating yet another side of dielectrophoresis, namely negative dielectrophoresis. Recall that, experimental studies with negative dielectrophoresis previously published [4] dealt mainly with very dilute suspensions. To extend the work further, we chose to work with concentrated suspensions [~5-15%(v/v)] of neutrally buoyant polyolefin particles suspended in corn oil. Following the application of a high-gradient ac field (~kV/mm), we found that, due to interparticle electric and hydrodynamic interactions, these suspensions underwent a phase separation and formed a propagating distinct front between the regions enriched with and depleted of particles. The purpose of this chapter is to study quantitatively, both experimentally and theoretically, this field induced phase separation. Clearly, as expected, at such high concentrations, the basic assumptions of the single particle model, which works nicely for

dilute suspensions, are no longer applicable since it becomes necessary to account for interparticle interactions, the effect of the particles on the electric-field distribution, as well as for the concentration dependence of the suspension physical properties, such as the viscosity and the dielectric permittivity. Therefore, a new model was introduced by Khusid and Acrivos, which was described in Chapter 3.

The organization of the chapter is as follows: In Sec. 5.2, the suspension properties and the experimental setup being used will be described with a more detailed description of the experimental procedures found in [**Refs. 5, 31**]. Sec. 5.3 contains the experimental data on the field-induced formation and propagation of the concentration front. The comparison of the theoretical predictions with the experimental data is given in Sec. 5.4. In Sec. 5.5, a mechanism is proposed for the experimentally observed accumulation of the particles in the region of high-field strength near the high-voltage electrodes where, according to Eq. (1.17), the particles should have been repelled. The main conclusions are summarized in Sec. 5.6.

My contribution consisted in carrying out the experiments (Sec 5.3) and their interpretation and comparison with the theoretical predictions. The experiments were conducted in collaboration with Dr. Zhiyong Qiu. On the other hand, Dr. David Jacqmin carried out the simulation work at NASA's Glenn Center while Professors. Khusid and Acrivos deserve the credit for developing the theoretical basis for this work. This combined team effort led to a publication in Physical Review E **69**, 021402(2004)[**31**].

5.2 Experimental Procedures

5.2.1 Materials

The suspension consisted of neutrally buoyant spherical polyalphaolefin particles (AVEKA, Woodbury, MN) suspended in Mazola corn oil ($\rho_f = 0.92 g/cm^3, \eta_f = 59.7 cp$ at 23^0C). The particle size distribution on a number basis was measured with a Beckman-Coulter laser diffraction particle size analyzer LS 230 and the average diameter of the particles was found to be 87 μm with 80% of them having diameters between 68 to 116 μm. The dielectric permittivities of the suspension, ε_s^*, and that of the corn oil, $\varepsilon_f = 2.87$, were measured using the standard technique of dielectric spectroscopy. The detailed description of the dielectric measurement is described in Chapter 2. The value Re(β) was found to equal –0.15 over the frequency range 0.1- 3.5 kHz (used in the experiments) whereas Im(β) was found to decrease rapidly with frequency from $1.8 \cdot 10^{-3}$ for 0.1 kHz to less than $2 \cdot 10^{-4}$ for frequencies greater than 1 kHz (**Fig. 2.3**).

5.2.2 Electric chamber

The experiments were performed in a horizontal parallel-plate electric chamber described in Chapter 2 and Chapter 4. The photograph of the experimental setup as well as the electric field distribution in the channel is shown in [**Fig. 5.1**]. In contrast to the experimental study reported in Chapter 4, the chamber was always kept in the horizontal position with its top facing the camera since the particles were density matched with the suspending fluid.

5.2.3 Suspension Preparation

The suspensions were freshly prepared before each experiment and were continuously stirred for ~30 min with a magnetic stirrer to disperse the particles uniformly. The suspension thus formed was kept for about 2 hours to allow those few particles which were either heavier or lighter than the fluid to settle down or float on the surface, and only that fraction of the suspension consisting of neutrally buoyant particles was used in the experiments. This suspension was then pumped into the chamber at a very low flow rate to prevent the trapping of air bubbles inside it. Once the chamber was filled without any air having been trapped within it, the flow was stopped and an ac electric field was applied. Typical experiments lasted about 30-90 min. Once the experiment was completed, the chamber was flushed with pure corn oil and the electrodes were gently cleaned.

5.3 Experimental Data

The photos presented in Fig. 5.2 show the time evolution of the particle distribution in the 10%(v/v)-suspension following the application of an electric field of 5 kV_{rms} and 0.1 kHz. The particles (seen as white spots in the photos) were initially uniformly distributed above the grounded and high-voltage electrodes [Fig. 5.2(a)]. As expected, the dielectrophoretic force, Eq. (1.17), caused the particles to move from the regions of high field strength towards those of low strength [Fig. 5.1(b)]. It took about 45 s for the particles, which were initially located near the high-voltage electrodes, to move away so that the electrodes became visible [Fig. 5.2(b)]. Following a 90-s exposure to the applied field, most of the particles traveled along the channel cross section from the regions near the high-voltage electrodes toward the low field region located above the grounded

electrode [Fig. 5.2(c)]. After about 150 s a distinct front formed along the channel between the suspension and the suspending fluid with the latter containing very few particles [Fig. 5.2(d)]. As time progressed, the front slowly moved away from the high field regions and the particles became progressively confined to a thin column above the grounded electrode [Fig. 5.2(e)]. After a sufficiently long exposure to the field, ~1 hr, nearly all the particles accumulated in the region above the grounded electrode, and the concentration front stopped moving. At that point the experiment was terminated given that no further changes could be discerned [Fig. 5.2(f)].

A similar type of field-driven particle redistribution was observed in suspensions having particle concentrations 5%, 10%, and 15% (v/v) and the photos presented in Fig. 5.3 demonstrate the final location of the concentration fronts for these suspensions. The sharpness of the front, as seen from the top of the channel, was found to increase with an increase in the magnitudes of the applied ac voltage and of the frequency (Fig. 5.4). We found that the use of the characteristic time for dielectrophoresis [**Refs. 4, 5**] τ_d, Eq. (5.1), makes it possible to combine the data on the time dependence of the front position for different voltages and frequencies into one band for $t/\tau_d \leq 20$ (Fig. 5.5). Here,

$$\tau_d = \frac{3d^4\eta_f}{a^2\varepsilon_0\varepsilon_f|\mathrm{Re}(\beta)|V_{rms}^2}, \qquad (5.1)$$

where η_f is the viscosity of the suspending fluid, d is the electrode width, a is the particle radius, and V_{rms} is the root mean square of the applied ac voltage.

Note that a distinct concentration front, as seen in Fig. 5.3, does not form in dilute suspensions. This is evident from the photographs shown previously in Fig. 3.2, which depict the redistribution of the particles in the 0.1% (v/v)-suspension following a 90-s

exposure to the applied field of 5 kV_{rms} and 0.1 kHz. There the particles are seen to accumulate above the grounded electrodes and to form a poorly defined undulating boundary between the suspension and the suspending fluid along the channel. Also, as can be seen from the photos in Figs. 5.2 and 5.3, another feature of the concentrated suspensions, ~ 5%-15% (v/v), is the appearance of a thin stripe of particles in the region of high-field strength along the centerline of the high-voltage electrode, where they should have been repelled by the dielectrophoretic force, Eq. (1.17). The stripe is roughly one particle thick and two or three particles wide. Its width was found to increase slightly with an increase in the initial particle concentration of the suspension. Such an accumulation of the particles in that region was not observed in dilute suspensions, ~0.01%-0.2% (v/v) [**Ref. 4**].

5.4 Simulation Results and Comparison with Experiments

The simulations were conducted using the data on the fluid and particle properties reported in Sec. 5.2. The simulations for the 5-15% (v/v)-suspensions were conducted using the electro-hydrodynamic model, Eqs. (3.9)-(3.13). The field-driven suspension flow was computed only within a periodic cell containing two halves of the high-voltage and grounded electrodes [Fig. 5.1(b)] with the appropriate boundary conditions Eqs. (5.2) and (5.3):

$$\left[\mathbf{E}^{*}_{\omega,\mathrm{II}}\right]_{S}=0,\quad \left[\mathbf{D}^{*}_{\omega,\perp}\right]_{S}=0,\quad \mathrm{Re}\left(\varphi^{*}_{\omega}\right)_{S_{el}}=\varphi_{el},\quad \mathrm{Im}\left(\varphi^{*}_{\omega}\right)_{S_{el}}=0 \qquad (5.2)$$

$$\mathbf{v}|_{S}=0,\quad \mathbf{j}_{p,\perp}|_{S}=0,\quad \text{and}\quad \mathbf{v}|_{t=0}=0,\quad c|_{t=0}=c_{0}, \qquad (5.3)$$

where the brackets denote the change in the respective variable along the tangential (II) and normal ($\perp$) directions to the channel wall S, $\varphi_{el}\cos\omega t$ is the potential applied at the

electrode surface S_{el}, and c_0 is the initial particle concentration. The ac field was applied at time $t = 0$.

The pictures presented in Fig. 5.6 show the computed evolution of the concentration distribution along the channel cross section following the application of an ac field of 5 kV_{rms} and 0.1 kHz to the 10%(v/v)-suspension at $t = 0$. After 5 min, the region above the high voltage electrode appears to be nearly free of particles (i.e., $c \approx 0$), whereas the concentration in the region above the ground electrode is gradually increasing, forming a distinct front, consistent with the experimental observations for concentrated suspensions (Fig. 5.2). The pictures presented in Fig. 5.6 indicate that the field-induced particle redistribution is accompanied by the formation of two vortices in the channel cross section separated by the concentration front. The suspension flows clockwise in the particle enriched and counter-clockwise in the region which has been depleted of particles. Depicted in Figs. 5.6 are the variations of the suspension velocity and of the total particle flux, $c\mathbf{v} + \mathbf{j}_p$, which demonstrate that the convective term dominates, causing the particles to move mainly along the flow streamlines. As a result, only the particles close to the concentration front travel with the front towards the low field region due to the presence of the component of $\mathbf{j}_p$ directed perpendicular to the front. The simulations showed that due to the relatively low magnitude of the particle polarization, $|\beta| \sim 0.15$, any changes of the electric field caused by the particle redistribution were within 10-30 % and were mainly located in the region close to the concentration front. Thus, for our experimental conditions, the field distribution away from the front region remained unaltered from that depicted in Fig. 5.1(b).

To compare the theoretical predictions with the experimental data, the computed particle concentration profile was averaged along the vertical direction to obtain $c_{av} = \frac{1}{h}\int_0^h c(x,y,t)dy$ which characterizes the particle distribution as seen on a photo taken through the channel top. As an example, the plots presented in Fig. 5.7 illustrate the computed time variation of c_{av} between the centers of the ground ($x = 0$) and the adjacent high-voltage electrodes ($x = 3.6$ mm) for the 10%(v/v)-suspension following the application of the electric field of 5 kV_{rms} and 0.1 kHz. Such figures were used to simulate the position of the concentration front as a function of time for suspensions having particle concentrations 5%, 10%, and 15%(v/v) for the range of voltages and frequencies used in our experiments. As can be seen from Fig. 5.5(b), the simulation results for the propagation of the concentration front are in a reasonable agreement with experimental data for $t/\tau_d \leq 20$ even though the model contains no fitting parameters. As time progresses, the simulations of the front position are found to overestimate the data for the high voltages and frequencies and to underestimate the data for the low voltages and frequencies. Also, the simulations do not predict that the front sharpness, as seen from the channel top (Fig. 5.4), increases with an increase in the magnitudes of the applied voltage and of the frequency. These drawbacks of the model might be related to the fact that this is a continuum model which operates on scales substantially larger than the particle size. Also, this model ignores any electrophoretic phenomena the significance of which increase with a reduction in the magnitude and frequency of the applied voltage and neglects the field-induced solid-like behavior of concentrated suspensions (the appearance of a yield stress, in particular) under the action of a strong electric field. As a

result, the model, Eqs. (3.1), (3.9)-(3.13), accounts for the influence of the field frequency on the particle motion only through the frequency dependence of the particle polarizability, $\beta(\omega)$.

5.5 Particle Accumulation On the High-Voltage Electrode

In this section, we shall propose a plausible mechanism for the particle accumulation along the centerline of the high-voltage electrode shown in [Fig. 5.8], which was observed in experiments with concentrated suspensions (~5-15%(v/v)). {Note that such a particle accumulation had not been reported or observed previously for dilute suspensions (~0.1%-1%(v/v)) [**4, 5**]}. Using Laplace's equation and accounting for the symmetry and periodicity of the electrode array [Fig. 5.1(a)], we find that the electric potential near the high-voltage electrode, $y \to 0$, can be expressed as

$$\varphi \approx \sqrt{2} V_{rms} \left[1 + Ay - \frac{y^3}{6} \frac{d^2 A}{dx^2} + O(y^5) \right] \cos \omega t, \qquad (5.4)$$

where $A(x)$ is symmetric about the electrode center, x_c. A numerical solution of Laplace's equation indicates that $A > 0$ and $d^2A/dx^2 > 0$ at $x = x_c$ [Fig. 5.1(b)]. Using Eq. (5.4), we therefore obtain that

$$\langle \mathbf{E}^2 \rangle \approx V_{rms}^2 \left\{ A^2 + \left[(dA/dx)^2 - A d^2A/dx^2 \right] y^2 \right\}, \quad \langle E_y^2 \rangle \approx V_{rms}^2 \left[A^2 - A(d^2A/dx^2) y^2 \right] \qquad (5.5)$$

Since $dA/dx \to 0$ for $x \to x_c$, the distribution of the field strength has a saddle point at x_c. Substitution of $\langle \mathbf{E}^2 \rangle$ into Eq. (1.17) yields the dielectrophoretic force acting on a particle near this point

$$\mathbf{F}_{dep} \approx$$

$$4\varepsilon_0\varepsilon_f\pi a^3\,\mathrm{Re}(\beta)V_{rms}^2\left\{\left[A\frac{dA}{dx}+\frac{1}{2}\left(\frac{dA}{dx}\frac{d^2A}{dx^2}-A\frac{d^3A}{d^3x}\right)y^2\right]\mathbf{e}_x+\left[\left(\frac{dA}{dx}\right)^2-A\frac{d^2A}{dx^2}\right]y\mathbf{e}_y\right\} \quad (5.6)$$

Polarized particles located near an electrode also experience an attraction force toward the electrode, which equals approximately the dipolar force between the particle and its image. The equation for this dipolar force [**Ref. 1**], taking the case of a negligibly small imaginary component of β, yields the following expression for the attraction force acting on a particle whose center is located at the distance y from the electrode surface: $\mathbf{F}_a \approx -\pi\varepsilon_0\varepsilon_f[\mathrm{Re}(\beta)]^2\langle E_y^2\rangle(3a^6/2y^4)\mathbf{e}_y$. Therefore, a particle will be trapped near the high-voltage electrode when the attraction force exceeds the y component of the dielectrophoretic force [Fig. 5.9]. Using Eqs. (5.5), we find that this condition is met for

$$3a^3|\mathrm{Re}(\beta)|\left[A^2-A(d^2A/dx^2)y^2\right]\geq 8y^5\left[A(d^2A/dx^2)-(dA/dx)^2\right] \quad (5.7)$$

The shape and size of the region defined by Eq. (5.7) is independent of the applied voltage. Having the maximum height near the centerline of about one particle diameter, it occupies a thin layer near the surface of the high voltage electrodes (Fig. 5.10), which constitutes about 0.45% of the channel volume. Following the application of an electric field, the x component of the dielectrophoretic force, Eq. (5.6), will cause the negatively polarized particles, which were initially located in this region, to move toward the centerline of the high-voltage electrode. When the number of these particles is sufficiently large they will form continuous stripes along the high-voltage electrodes. This explains the fact that such stripes are only observed for sufficiently concentrated suspensions. The characteristics of the particle accumulation along the centerlines of the high-voltage electrodes are qualitatively consistent with the experimental data reported in

Sec. 5.3. The prediction of the particle aggregation patterns on the high voltage electrodes is well beyond the scope of the continuum model presented in Chapter 3, which operates on scales substantially larger that the particle diameter.

5.6 Summary and Conclusions

We reported that, when concentrated suspensions of neutrally buoyant, negatively polarized particles were subjected to a high-gradient ac field, a distinct front was formed separating a suspension from a region of essentially particle-free fluid which moved away from the high field regions and eventually confined the particles to a thin column in the low field region. This phenomenon owed its existence to the interparticle electrical interactions. A theory was proposed by Khusid and Acrivos, for the front propagation which generalizes their earlier theory for the thermodynamics of the field-induced phase transitions in suspensions of polarized particles. The electro-hydrodynamic model encompasses the coupled quasi-steady field equations and the momentum and continuity balance equations for one- and two-phase states of a suspension, which are averaged over the field oscillations. The suspension is viewed as an effective Newtonian fluid with a concentration dependent effective viscosity. The bulk electric force exerted on a suspension and the particle velocity relative to the suspending fluid are expressed in terms of the chemical potential of the particles. Simulations were conducted using the data for the fluid and particle properties which were measured independently. The simulation results for the front propagation are quantitatively consistent with the experimental data even though the model contains no fitting parameters.

We also observed the appearance of a thin stripe, roughly one particle thick and two or three particles wide, in the region of the high-field strength, which should have been

repelled from this region by the dielectrophoretic force. The formation of such a thin stripe in the high-field region was explained by considering the balance of the various forces exerted on a particle located close to the high voltage electrodes.

The results of our studies demonstrate that by combining field-induced dielectrophoresis and phase separation one can create a new method for strongly concentrating particles in focused regions of a dielectrophoretic chamber. The proposed electro-hydrodynamic model can simulate the basic characteristics of these coupled phenomena.

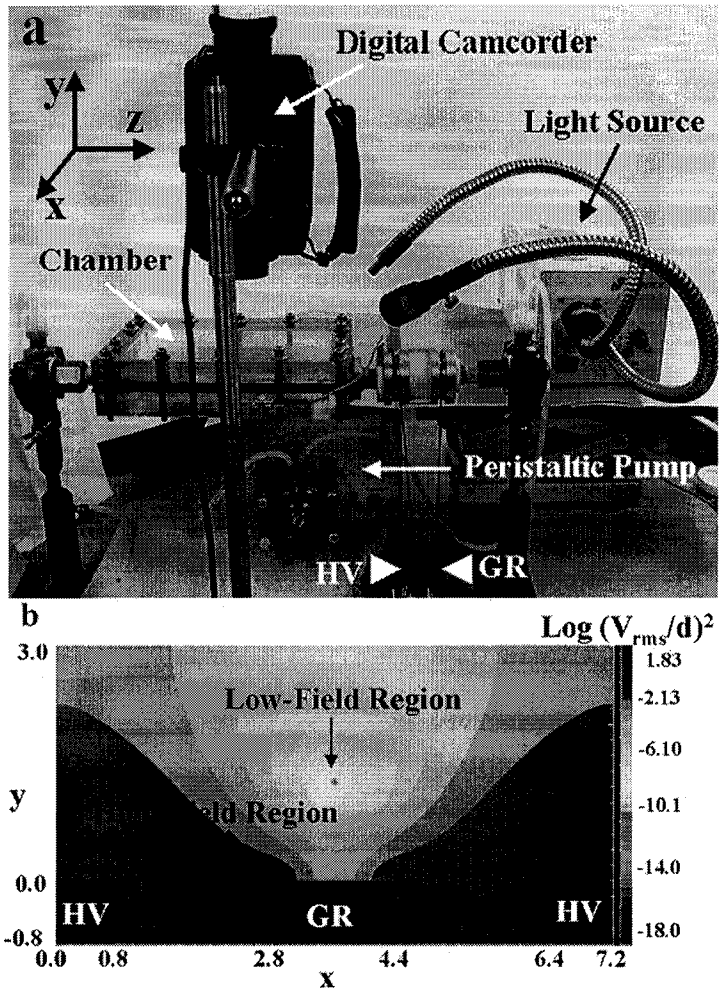

Figure 5.1: (a) The experimental setup with a dielectrophoretic chamber, having 16 electrodes pairs alternately connected to the high-voltage and ground of the power supply **(b)** The distribution of the square of the field-strength, E^2 (expressed in units of V_{rms}^2/d^2 in base-10 logarithmic scale), for a pair of electrodes. Half of the high voltage electrodes are on the left ($0 \le x \le 0.8$) and on the right ($6.4 \le x \le 7.2$) and the grounded electrode is in the middle ($2.8 \le x \le 4.4$). The top (y=3.0) is also grounded.

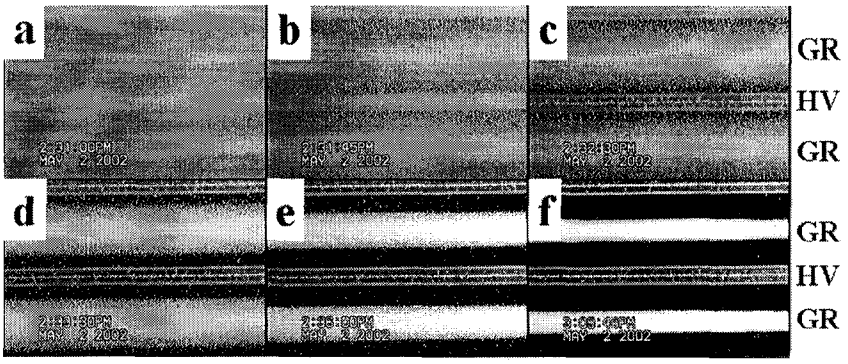

Figure 5.2: The particle distribution in a suspension with 10%(v/v) particle concentration (a) before and (b)-(f) following the application of a field $5kV_{rms}$, 100Hz at t= (b) 45s, (c) 90s, (d) 150s, (e) 300s, and (f) final state, ~39min. The electrode width is 1.6mm. HV and GR refer to the high-voltage and grounded electrodes, respectively.

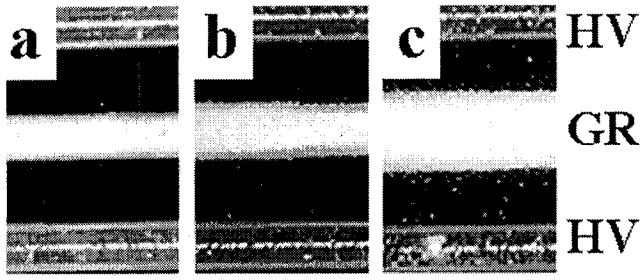

Figure 5.3: The final position of the concentration front in suspensions with (a) 5%, (b) 10%, and (c) 15% (v/v) particle concentrations following the application of a field $5kV_{rms}$, 100Hz. The exposure times: (a) 41min, (b) 38min, and (c) 30min. The electrode width is 1.6mm. HV and GR refer to the high-voltage and grounded electrodes respectively.

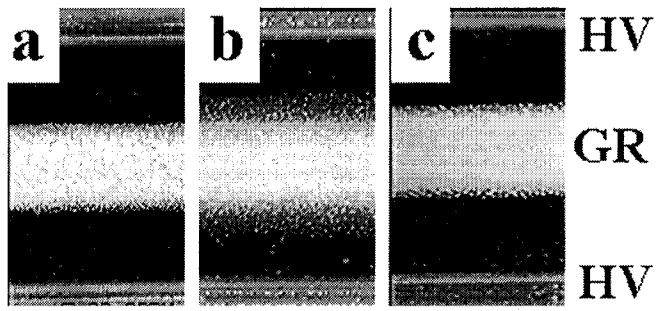

Figure 5.4: The effect of the field strength and frequency on the front sharpness in a suspension with 10%(v/v) particle concentration: (a) $5kV_{rms}$, 100Hz, t=20.5min, $t/\tau_d = 63.4$; (b) $3kV_{rms}$, 100Hz, t=54.5min, $t/\tau_d = 60.8$; and (c) $3kV_{rms}$, 2kHz, t=52.5min, $t/\tau_d = 58.6$. The electrode width is 1.6 mm. HV and GR refer to the high-voltage and grounded electrodes, respectively.

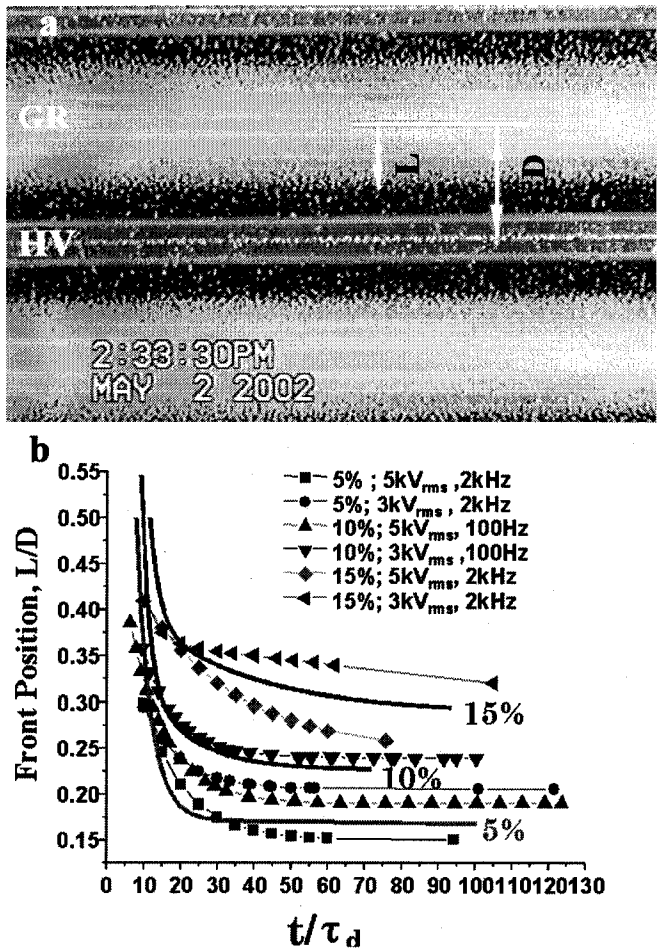

Figure 5.5: (a) The photographs illustrates how the front position L was measured; HV and GR refer to the high-voltage and grounded electrodes respectively; D=3.6mm. (b) The experimental data (symbols) and computational results (solid lines) of the electrohydrodynamic model presented in Chapter 3 for the front propagation in suspensions with 5%, 10%, and 15% (v/v) particle concentrations for different voltages and frequencies of the applied fields. The experimental data and the simulation results are plotted against a non-dimensional time t/τ_d, with τ_d given by Eq. (5.1).

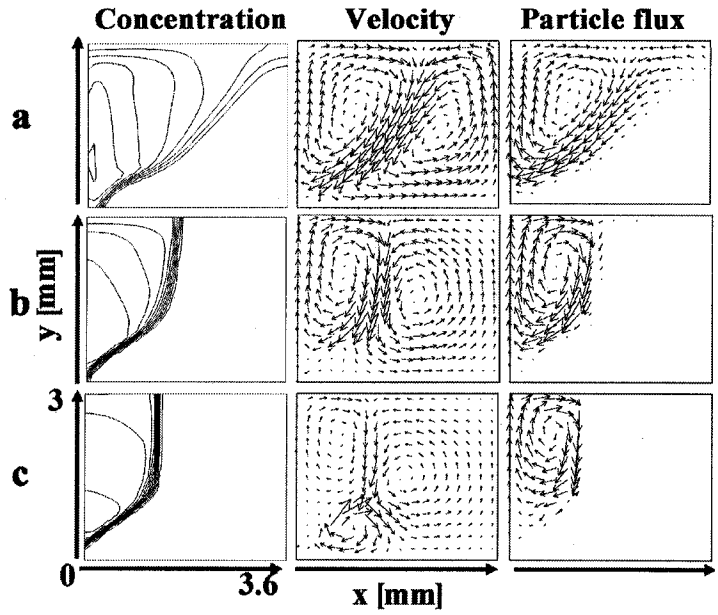

Figure 5.6: Numerical simulations of the concentration contours, the suspension velocities, and the particle fluxes for the 10% (v/v) suspension under the action of a field of $5kV_{rms}$ and 100Hz. Time is (a) 1 min, (b) 5min, and (c) 20 min. The computed values for c_{max} in the low-field region [in %(v/v)] are (a) 40.3, (b) 54.7, and (c) 60.9. The arrows show the relative magnitudes of the suspension velocities and the particle fluxes, respectively. In (a)-(c), the maximum values for v_{max} are (a) 45.1 μm/s, (b) 5.7 μm/s, and (c) 1.6 μm/s and the maximum values for $(cv + j_p)_{max}$ are (a) 0.123 μm/s, (b) 0.019 μm/s, and (c) 0.003 μm/s. Half of the grounded (GR) and high-voltage electrodes (HV) are on the left ($0 \le x \le 0.8$ mm) and on the right ($2.8 \le x \le 3.6$ mm), respectively. The top (y=3.0 mm) is also grounded.

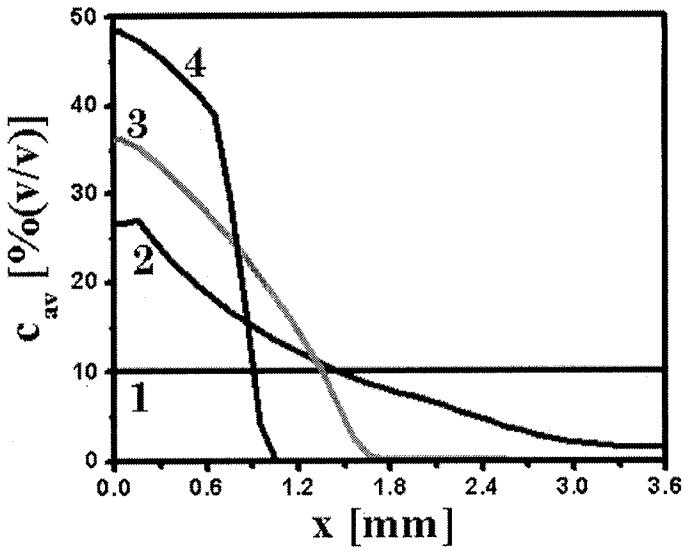

Figure 5.7: The computed time variation of the particle concentration profile averaged along the vertical direction, c_{av}, for a 10(v/v)% suspension following the application of a field of $5kV_{rms}$ and 100Hz. The locations x = 0 mm and x = 3.6 mm correspond respectively, to the centers of the adjacent ground (GR) and high-voltage (HV) electrodes. 1-4 correspond to concentration profiles at times = 0, 45, 120, and 2370 s, respectively.

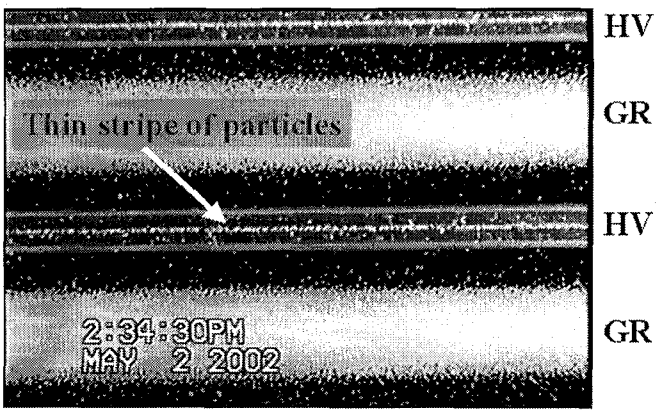

Figure 5.8: An experimental pictures taken after 210 sec following the application of an electric field, $5kV_{rms}$, 100Hz for a suspension having an initial particle concentration 10%(v/v) showing the particle accumulation in the centerline of the high-voltage (HV) electrode surface.

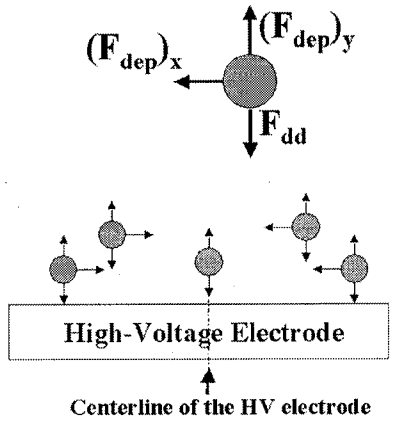

Figure 5.9: A schematic showing the various forces acting on a particle located close to the high-voltage (HV) electrode surface.

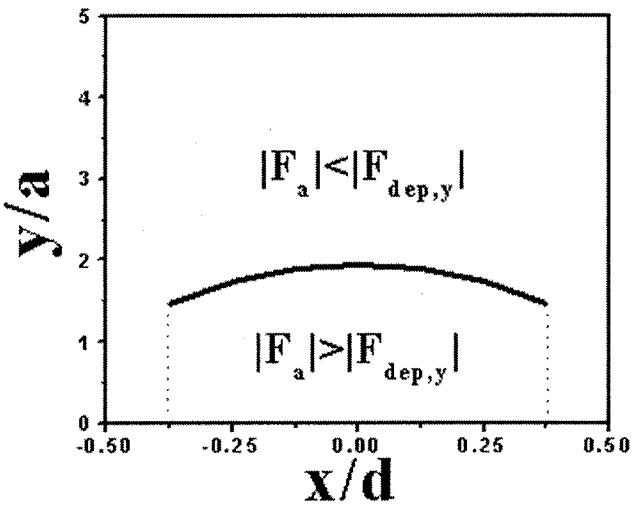

Figure 5.10: The computed boundary of the region (defined by Eq. 5.7) near the high-voltage electrode where the vertical component of the dipolar force exceeds that of the dielectrophoretic force; x/d =0.0, 0.5, and –0.5 refer to the center, and the two edges of the high-voltage electrode respectively; a is the particle radius.

Chapter 6

Study of some limiting cases of the high concentration equation for positive and negative dielectrophoresis

6.1 Introduction

Recall that, in Chapter 5, we showed that, when exposed to an electric field, a concentrated suspension of negatively polarized particles underwent an electric field induced phase transition forming a concentrated front, with regions enriched with particles separated from those without particles. In this chapter, we will focus on elucidating the mechanism of the concentration front formation by examining, both, analytically and numerically, the electro-hydrodynamic model (Chapter 3) for the special case when, via a similarity transformation, the model equations reduce to ordinary differential equations for the particle concentration. I analyzed the singular points of these ordinary differential equations and carried out the numerical simulations with the help of Profs. Khusid and Acrivos.

6.2 Problem Description

In this study, we considered the special case (Fig. 6.1) when, at time $t=0$, a suspension of neutrally buoyant particles (i.e., $\rho_p = \rho_f$) having bulk concentration c_0 is exposed to an ac electric field generated by the application of a voltage $V = Br^{1/2}\cos\omega t$ to the right electrode S_1

with the left electrode S_2 being grounded. Under these conditions, equations (3.9)-(3.11) are subjected to the standard boundary and initial conditions for the quasi-steady electrodynamic and flow equations [Chapter 3] which, in this geometry, become:

$$\varphi_\omega^*\big|_{S_1} = Br^{1/2},\ \varphi_\omega^*\big|_{S_2} = 0,\ \mathbf{v}\big|_{S_{1,2}} = 0,\ \mathbf{j}_{p,\perp}\big|_{S_{1,2}} = 0,\ \mathbf{v} \to 0 \text{ and } \mathbf{j}_p \to 0 \text{ for } r \to 0,$$

$$\mathbf{E}_\omega^* \to 0,\ \mathbf{v} \to 0,\ c \to c_0 \text{ and } \mathbf{j}_p \to 0 \text{ for } r \to \infty \text{ and } \mathbf{v}\big|_{t=0} = 0,\ c\big|_{t=0} = c_0, \qquad (6.1)$$

where $\perp$ denotes the normal component to the electrodes. We consider analytically the case of $|\beta| << 1$ when $\varepsilon_s^* \approx \varepsilon_f^*$, so that the electric field is unaffected by the presence of the particles. In this case, the solution of Laplace's equation, Eq. (3.10), subject to our boundary conditions, Eqs. (6.1), is $\varphi_\omega^* = Br^{1/2}\cos(\theta/2)$ in cylindrical coordinates giving, for the field strength $\langle \mathbf{E}^2 \rangle = B^2/8r$. Consequently when the field strength and the particle concentration c are both independent of the angle, θ, Eqs. (3.9) and (3.13) yield

$$\mathbf{v} = 0,\quad \frac{\partial p}{\partial r} = -c\frac{\partial \mu_p}{\partial r},\quad \frac{\partial c}{\partial t} - \frac{1}{r}\frac{\partial}{\partial r}\left[r\frac{c(1-c)^2 v_p}{6\pi a \eta_s(c)}\frac{\partial \mu_p}{\partial r}\right] = 0, \qquad (6.2)$$

where $\eta_s(c) = \eta_f \hat{\eta}(c)$ is the suspension viscosity, with η_f being the suspending fluid viscosity and $\hat{\eta} = \left(1 - \frac{c}{c_m}\right)^{-2}$ is chosen as the expression for the concentration dependence of the suspension viscosity with $c_m = 0.68$, being the maximum concentration beyond which the suspension is unable to flow. On account of Eq. (6.2), the steady state concentration distribution, to be referred to as the "equilibrium" profile $c_{eq}(r)$, satisfies the equation $\partial \mu_p / \partial r = 0$ everywhere within the single-phase domain of the suspension phase diagram (Fig. 3.1); hence, in

view of the expression for μ_p given by Eq. (3.1) and the boundary condition, $c \to c_0$ as $r \to \infty$, given in Eqs. (6.1),

$$f_0'(c_{eq}) - \frac{3\beta\lambda}{2(1-c_{eq}\beta)^2} = f_0'(c_0) \quad \text{with} \quad \lambda = \frac{\varepsilon_0 \varepsilon_f v_p B^2}{8 k_B T r} \tag{6.3}$$

As expected, and, as can be seen from Eq. (6.3), the particle concentration in the region $r \to 0$ is greater or smaller than c_0 depending on whether β is positive or negative. In fact, by making use of the asymptotic expression for f_0', given by Eq. (3.2) we find that, for $|\beta\lambda| \to \infty$

$$\ln c_{eq} \approx f_0'(c_0) + 3\beta\lambda/2 \quad \text{for } \beta < 0 \quad \text{and} \quad c_{eq} \approx c_m - \frac{2A(1-c_m\beta)^2}{3\beta\lambda} \quad \text{for } \beta > 0.$$

In the phase diagram of the suspension, shown in Fig. 3.1, equation (6.3) determines a line of a constant chemical potential. As can be seen from Fig. 6.2, these lines form two families separated by the limiting trajectory passing through the critical point on the spinodal, which corresponds to the bulk (i.e. for $\lambda = 0$) particle concentration c_{tr} given by the expression $f_0'(c_{tr}) = f_0'(c_{cr}) - \frac{3\beta\lambda_{cr}}{2(1-c_{cr}\beta)^2}$. Those of the first, (i.e. curve 3), $c_0 < c_{tr}$ for $\beta > 0$ and $c_0 > c_{tr}$ for $\beta < 0$, will intersect the coexistence curve, but those of the second family (curve 4) will not. In the former case, the equilibrium particle concentration, $c_{eq}(r)$, will change abruptly when the line of a constant chemical potential, Eq. (6.3), intersects the coexistence curve in the phase diagram while, in the second case, the spatial variation of $c_{eq}(r)$ will be smooth because the trajectory lies entirely in the single-phase region. We note, parenthetically, that for $|\beta| \to 0$, we have $\ln c_{tr} \approx f_0'[c_{cr}(0)] - \Lambda_{cr}(0)/2\beta$ for $\beta > 0$ and $c_{tr} \approx c_m - A/[f_0'[c_{cr}(0)] - \Lambda_{cr}(0)/2\beta]$ for $\beta < 0$. These abrupt changes in the particle concentration result from an "electric-field induced phase

transition", when the trajectory enters from a single-phase to a two-phase region after crossing the coexistence curve, which corresponds to the boundary between the two phases.

6.3 Self-Similarity Solutions

6.3.1 Asymptotic analysis

We next return to Eq. (6.2) and study the time variation of the particle concentration in regions of high, $|\beta\lambda| < \Lambda_{cr}/3|\beta|$, moderate, $1 < |\beta\lambda| < \Lambda_{cr}/3|\beta|$, and low, $|\beta\lambda| < 1$, field strengths, where, as mentioned earlier (Thesis, Page 31), $\Lambda_{cr}(\beta)$ ranges from 25.24 to 11.7 for values of β varying from –0.5 to 1. First of all we note that, depending on the local concentration, the suspension in the high field region could be either in the two-phase or the single-phase state depending on whether or not c lies, respectively, within or outside the range $c_1(\lambda) < c < c_2(\lambda)$, where $c_1(\lambda)$ and $c_2(\lambda)$ lie on the coexistence curve in the suspension phase diagram (Fig. 3.1). Recall, that the particle chemical potential for high field strengths is given by Eqs. (3.4)–(3.6). On the other hand, in regions of moderate and low field strengths, the suspension is in the single-phase state with the chemical potential given by Eqs. (3.1) and (3.2) as

$$\mu_p = -\frac{3\beta\varepsilon_0\varepsilon_f\langle E^2\rangle}{2(1-c\beta)^2} + \frac{k_B T}{v_p} f_0'(c) \tag{6.4}$$

As can easily be seen from Eq. (6.3), $c_{eq}(r) \approx c_0$ within the region of low field strengths, $|\beta\lambda| << 1$, hence Eqs. (6.2) and (6.4) can be linearized about c_0 giving, for the deviation of the particle concentration from equilibrium, $\tilde{c} = c - c_{eq}(r)$

$$\frac{\partial \tilde{c}}{\partial t} = \frac{1}{r}\frac{\partial}{\partial r}\left[r D_p(c_0)\frac{\partial \tilde{c}}{\partial r}\right] \quad \text{with} \quad D_p = \frac{k_B T}{6\pi a \eta_f}\hat{D}(c_0) \quad \text{for} \quad \tilde{c}|_{t=0} = c_0 - c_{eq}, \tag{6.5}$$

where, from Eq. (6.3), $(c_0 - c_{eq}) = -\dfrac{3\beta\lambda(r)}{2f_0''(c_0)(1-c_0\beta)^2}$ and $\hat{D} = \dfrac{c(1-c)^2 f_0''(c)}{\hat{\eta}(c)}$, with $\hat{D} = 1$ for $c = 0$ and $\hat{D} = (1-c_m)^2 A/c_m$ for $c = c_m$. As can be seen from Eq. (6.5), the rate at which the particle concentration profile approaches $c_{eq}(r)$ is governed by weak Brownian diffusion and is unaffected by the electric field.

In contrast, the kinetics of the particle redistribution within the regions of high and moderate field strengths is governed by the electric field, with the contribution of the steric factor generally being negligible. Under these conditions, Eq. (6.2) together with Eqs. (3.4) and (6.4) for μ_p yield the following equations for the two-phase and single-phase domains in the suspension phase diagram (Fig. 3.1), respectively:

$$\frac{\partial c}{\partial t} - \frac{\beta\varepsilon_0\varepsilon_f v_p B^2}{32\pi a\eta_f(1-c_m\beta)}\frac{1}{r}\frac{\partial}{\partial r}\left[\frac{c(1-c)^2}{\hat{\eta}(c)r}\right] = 0 \qquad \text{for } c_1(\lambda) < c < c_2(\lambda) \text{ and } |\beta\lambda| < \Lambda_{cr}/3|\beta| \quad (6.6)$$

$$\frac{\partial c}{\partial t} + \frac{\beta\varepsilon_0\varepsilon_f v_p B^2}{32\pi a\eta_f}\frac{1}{r}\frac{\partial}{\partial r}\left[\frac{rc(1-c)^2}{\hat{\eta}(c)}\frac{\partial}{\partial r}\frac{1}{(1-c\beta)^2 r}\right] = 0 \qquad \text{for } 1 < |\beta\lambda| < \Lambda_{cr}/3|\beta| \quad (6.7)$$

Unfortunately as can be seen from Eq. (3.6), the steric factor cannot be neglected outside the two-phase region $c_1(\lambda) < c < c_2(\lambda)$ when $|\beta\lambda| < \Lambda_{cr}/3|\beta|$ and the analysis requires the use of the full Eq. (6.2). Now, dimensional analysis shows that both Eqs. (6.6) and (6.7) with our boundary conditions, Eqs. (6.1), have a similarity solution of the form $c_t(\xi_t)$ with $\xi_t = r/g_t t^{1/3}$, and $c_s(\xi)$ with $\xi = r/g_s t^{1/3}$, respectively, where $g_s = \left(\dfrac{3|\beta|\varepsilon_0\varepsilon_f v_p B^2}{32\pi a\eta_f}\right)^{1/3}$ and $g_t = \dfrac{g_s}{(1-c_m\beta)^{1/3}}$, with $c_t(\xi_t)$ and $c_s(\xi)$ satisfying:

(a) For $|\beta\lambda| < \Lambda_{cr}/3|\beta|$ and $c_1(\lambda) < c_t(\xi_t) < c_2(\lambda)$, i.e. for the two-phase region,

$$-\xi_t^2 \frac{dc_t}{d\xi_t} + \text{sign}(\beta)\frac{dy_t}{d\xi_t} = 0 \qquad \text{where} \quad y_t = -\frac{c_t(1-c_t)^2}{\hat{\eta}(c_t)\xi_t}, \tag{6.8}$$

with boundary conditions $y_t \to 0$ for $\xi_t \to 0$ and $c_t \to c_0$ for $\xi_t \to \infty$, and

(b) for $1 < |\beta\lambda| < \Lambda_{cr}/3|\beta|$, i.e. for the single-phase region,

$$-\xi^2 \frac{dc_s}{d\xi} + \text{sign}(\beta)\frac{dy_s}{d\xi} = 0 \text{ where } y_s = \frac{\xi c_s(1-c_s)^2}{\hat{\eta}(c_s)} \frac{d}{d\xi}\left[\frac{1}{(1-c_s\beta)^2\xi}\right], \tag{6.9}$$

with boundary conditions $y_s \to 0$ for $\xi \to 0$ and $c_s \to c_0$ for $\xi \to \infty$.

In the special case when $c_t \to 0$ and $c_s \to 0$, Eqs. (6.8) and (6.9) can be simplified into a common linear equation which, as will be shown presently, has the important general property that only a solution with a discontinuity (i.e. a solution with a shock) can satisfy all our boundary conditions. Specifically, it is easy to show that the solution of the (common) linearized version of Eqs. (6.8) and (6.9) is, with the subscripts being omitted,

$$c = \frac{c_0\xi}{\left[\xi^3 + \text{sign}(\beta)\right]^{1/3}} \text{ and } y = -\frac{c_0}{\left[\xi^3 + \text{sign}(\beta)\right]^{1/3}}.$$

As can be seen from these expressions, our boundary conditions are satisfied only for $\xi \to \infty$. On the other hand, when $\beta < 0$, $c \to \infty$ and $y \to -\infty$ for $\xi \to 1$, while when $\beta > 0$, $c \to 0$ and $y \to -c_0$ for $\xi \to 0$. This suggests, therefore, that we should seek a discontinuous solution (i.e., a shock solution) to Eqs. (6.8) and (6.9) in order to be able to satisfy the remaining boundary condition $y \to 0$ as $\xi \to 0$.

6.3.2 Two-Phase Region

Figures 6.3 (a) and 6.3 (b) show the behavior of the trajectories of Eq. (6.8) starting from various locations in the phase plane for $\beta < 0$ and $\beta > 0$, respectively, in the region $0 \le c_t \le c_m$ and

$\xi_t \geq 0$. A brief description of the behavior of these trajectories as well as the local expansions are summarized in Table 6.1 and 6.2 for $\beta < 0$ and $\beta > 0$, respectively.

The phase planes of Eq. (6.8), depicted in Figs. 6.3(a) and 6.3(b) for negative and positive β, respectively, clearly demonstrate that there exist no continuous trajectories satisfying our boundary conditions for which c_t approaches a constant value for $\xi_t \to \infty$, and $y_t \to 0$ for $\xi_t \to 0$. Instead all the trajectories originating from $\xi_t \to \infty$, end up at $\xi_t \to 0$ with $y_t \neq 0$. Thus, in order to construct a discontinuous solution (i.e. a shock solution) that satisfies our boundary conditions for a particular value of c_0, we need to take part of the trajectory (Figs. 6.3), which approaches c_0 for $\xi_t \to \infty$, and combine it with part of another trajectory for which $y_t \to 0$, as $\xi_t \to 0$, provided that the relative particle flux, $F_t = -\xi_t^2 c_t + \text{sign}(\beta) y_t$, is continuous along the composite trajectory. For $\beta > 0$ [Fig. 6.3(b)], both the trajectories passing through the fixed point $\xi_t = 0$, $c_t = c_m$ with $y_t = 0$ [trajectory 5] as well as the isocline $c_t = c_m$ meet the requirement $y_t \to 0$ for $\xi_t \to 0$. However, the latter is inappropriate because $c_m > c_2(\lambda)$ for any finite value of $\lambda(r)$, thus violating the condition that the trajectories of Eq. (6.8) fall within the two-phase region in the suspension diagram (Fig. 3.1). On the other hand, for $\beta < 0$ [Fig. 6.3(a)], only the isocline $c_t = 0$ meets the requirement $y_t \to 0$, as $\xi_t \to 0$, which appears to be appropriate since $c_1(\lambda)$ becomes exponentially small as $r \to 0$ given that, in this case, $\lambda \to \infty$. (Fig. 3.1)

To construct a composite trajectory which produces a traveling shock discontinuity, we need to consider the variations of the relative particle flux, $F_t = -\xi_t^2 c_t + \text{sign}(\beta) y_t$ along the trajectories

of Eq. (6.8) as well as along the verticals in the phase plane (Figs. 6.3). The derivatives of F_t are, respectively:

$$\frac{dF_t}{d\xi_t} = -2\xi_t c_t \text{ (equivalent to Eq. (6.8)), and } \frac{\partial F_t}{\partial c_t} = -\frac{1}{\xi_t}\left[\xi_t^3 + \text{sign}(\beta)\frac{d}{dc_t}\left(\frac{c_t(1-c_t)^2}{\hat{\eta}(c_t)}\right)\right] \quad (6.10)$$

with $F_t|_{c_t=0} = 0$, $F_t|_{c_t=c_m} = -\xi_t^2 c_m$, and $F_t \to -\xi_t^2 c_0$ for $\xi_t \to \infty$. As indicated in the first of the two Eqs. (6.10), F_t decreases monotonically with increasing ξ_t along a trajectory of Eq. (6.8), whereas $\partial F_t/\partial c_t$ changes its sign along the vertical in intersections with the isocline of the vertical direction (Figs. 6.3). Taking into account these properties, we find that, for $\beta < 0$, every trajectory of the second family [Fig. 6.3(a)], originating at the fixed point $\xi_t = 0$, $c_t = c_m$ and approaching c_0 for $\xi_t \to \infty$, intersects once the curve Q_0 along which $F_t = 0$, i.e. $\xi_t^3 = (1-c_t)^2/\hat{\eta}(c_t)$, since along, this trajectory F_t, is positive for $\xi_t \to 0$ but becomes negative as $\xi_t \to \infty$. Hence, for every c_0 there exists only one composite trajectory of Eq. (6.8) for $\beta < 0$ that satisfies our boundary conditions. To construct it, we need to take part of the trajectory approaching c_0 for $\xi_t \to \infty$ located to the right from its intersection with the curve Q_0, and then combine it with the isocline $c_t = 0$ to the left from this point [Fig. 6.3(a)]. Thus, the curve Q_0 specifies the location of the shock and the magnitude of the concentration jump for $\beta < 0$. A typical example of such a solution is shown in Fig. 6.4.

Now, we consider the case of $\beta > 0$. With increasing c_t for fixed ξ_t along a vertical in the phase plane [Fig. 6.3(b)], the value of F_t increases monotonically inside the domain bounded by the isocline $\xi_t^3 + \frac{d}{dc_t}\left[\frac{c_t(1-c_t)^2}{\hat{\eta}(c_t)}\right] = 0$ [shown by Region 2 in Fig. 6.5] and decreases monotonically

outside [shown by Regions 1 and 3 in Fig. 6.5]. Hence, we can construct two curves, namely Q_1 and Q_2 as follows. For the curve Q_1, we march along the upper branch of the curve 5 (shown in Fig. 6.3b) starting from the point $\xi_t = 0, c_t = c_m$ with $y_t = 0$ and first evaluate the value of the function $F_t(\xi_t)$. Now, since the upper branch of curve 5 (shown in Fig. 6.3b) lies entirely within the domain bounded by the isocline (shown by Region 2 in Fig. 6.5). Hence, for every point along the upper branch of curve 5, we can find another value of c_t (lying in the Region 1 in Fig. 6.5) such that the value of F_t is the same. The locus of these points is referred to as curve Q_1. Curve Q_2 was constructed in a similar fashion starting from the upper branch of the isocline in place of curve 5. Note that, as shown in Fig. 6.3(b), the curve Q_1 always lies above Q_2 for any fixed ξ_t.

Now, to construct the composite trajectory of Eq. (6.8) for $\beta > 0$, we next considered separately two cases depending on whether c_0 is less than or greater than c_{lim}. For the first case, when $c_0 \le c_{lim}$, (shown in Fig. 6.6, left), we need to take part of the trajectory approaching c_0 for $\xi_t \to \infty$, located to the right from its intersection with the curve Q_1, and combine it with the upper branch of the limiting trajectory (trajectory 5) on the left from this point [Fig. 6.3(b)]. Thus, the curve Q_1 specifies the location of the shock and the magnitude of the concentration jump for $c_0 \le c_{lim}$. An example of the concentration profile for the case $c_0 \le c_{lim}$ is shown in [Fig. 6.6, left].

On the other hand, when $c_0 > c_{lim}$, we need to be more careful because the function c_t vs. ξ_t along a trajectory of Eq. (6.8) for $\beta > 0$, which approaches $c_0 \ge c_{lim}$ as $\xi_t \to \infty$ (trajectory 4), becomes multivalued inside the domain bounded by the isocline due to the negative sign of

$dc_t/d\xi_t$ within that region [Fig. 6.3b]. This leads to the formation of a shock at the intersection of this trajectory with the upper branch of the isocline shown by trajectory 1 in [Fig. 6.3(b)]. Since $\partial F_t/\partial c_t > 0$ between the two branches of the isocline, whereas $\partial F_t/\partial c_t < 0$ below the lower branch and $F_t|_{c_t=0} = 0$, there exists only a single value of c_t along the vertical passing through the intersection for which the value of F_t becomes equal to that at the intersection. The curve Q_2 specifies the location of the first shock and the magnitude of the concentration jump for $c_0 > c_{lim}$. Since the value of F_t for any ξ_t along the upper branch of the isocline is greater than that at the point with the same ξ_t on the upper branch of the limiting trajectory passing through the fixed point $\xi_t = 0$, $c_t = c_m$, Q_2 is located to the right from the curve Q_1 [Fig. 6.3(b)]. Hence to construct a composite trajectory of Eq. (6.8) for $\beta > 0$, which will be the only one satisfying our boundary conditions for $c_0 > c_{lim}$, we need to take part of the trajectory approaching c_0 for $\xi_t \to \infty$ located to the right from its intersection with the upper branch of the isocline where it jump down vertically onto curve Q_2, combine it with the part of the appropriate trajectory bounded by the curves Q_1 and Q_2, followed by a vertical upward jump onto the upper branch of the limiting trajectory at the point where Q_1 and the trajectory between Q_1 and Q_2 intersects, followed by continuation of the limiting trajectory towards left until $\xi_t = 0, c_t = c_m$ [Fig. 6.3(b)].

6.3.3 Single Phase Region

To analyze Eq. (6.9), we begin with considering the intersections of its trajectories with the boundaries of the region $0 \le c_s \le c_m$ and $\xi \ge 0$. When $\xi \to \infty$, the trajectories are given by the asymptotic expansions

$$c_s \approx c_0 - \frac{\mathrm{sign}(\beta) c_0 (1-c_0)^2}{3\hat{\eta}(c_0)(1-c_0\beta)^2 \xi^3} \text{ and } y_s \approx -\frac{c_0(1-c_0)^2}{\hat{\eta}(c_0)(1-c_0\beta)^2 \xi} \tag{6.11}$$

The trajectories which pass through the point $\xi = 0$, $c_s = 0$ are given by the expansion

$$c_s \approx M\xi + 2M^2(1+1/c_m)\xi^2 \text{ with } y_s \to -M, \text{ as } \xi \to 0, \text{ for any } M \geq 0, \tag{6.12}$$

while the trajectories passing through the point $\xi = 0$, $c_s = c_m$ are given by

$$c_s \approx c_m(1 - L\xi^{1/2}) \text{ with } y_s \to -c_m(1-c_m)^2 L^2/(1-c_m\beta)^3, \text{ as } \xi \to 0, \text{ for any } L \geq 0 \tag{6.13}$$

In addition, a set of trajectories intersecting the line $c_s = 0$ at a point $\xi' > 0$ is given by the asymptotic expansions $c_s \approx N|\xi - \xi'|^{1/2}$ with $y_s \to \beta N^2 \mathrm{sign}(\xi - \xi')$, as $\xi \to \xi'$, for any $N > 0$ and $c_s \approx \frac{\xi'^3 + \mathrm{sign}(\beta)}{2|\beta|\xi'}(\xi - \xi')$ with $y_s \approx \xi' \frac{\xi'^3 + \mathrm{sign}(\beta)}{2\beta}(\xi - \xi')$ for $(\xi - \xi') \to 0$ but positive, while a set of trajectories intersecting the line $c_s = c_m$ at a point $\xi' > 0$ for $\xi \to \xi'$ is given by the asymptotic expansions $c_s \approx c_m[1 - P(\xi - \xi')^{1/3}]$ with $y_s \to -2\beta c_m(1-c_m)^2 P^3/3(1-c_m\beta)^3$ for any $P \neq 0$ and $c_s \approx c_m - \frac{\xi' c_m^{1/2}(1-\beta c_m)^{3/2}}{|\beta|^{1/2}(1-c_m)}(\xi - \xi')^{1/2}$ with $y_s \approx -\mathrm{sign}(\beta)\frac{\xi'^3 c_m^{1/2}(1-\beta c_m)^{3/2}}{|\beta|^{1/2}(1-c_m)}(\xi - \xi')^{1/2}$

(6.14)

Finally, when $\beta > 0$, Eq. (6.9) has also another trajectory [in addition to (6.13)] passing through the point $\xi = 0$, $c_s = c_m$, given by

$$c_s \approx c_m - 3c_m(1-c_m\beta)^2 \xi^3/5(1-c_m)^2 \text{ with } y_t \approx -9c_m(1-c_m\beta)^2 \xi^5/25(1-c_m)^2, \text{ as } \xi \to 0 \tag{6.15}$$

Next, we consider the conditions under which the derivative $dc_s/d\xi$ along a trajectory of Eq. (6.9) changes its sign. In view of Eq. (6.9), we find that wherever $dc_s/d\xi = 0$:

$$\left.\frac{d^2c_s}{d\xi^2}\right|_{dc_s/d\xi=0} = -\left(\frac{1-c_s\beta}{2\xi^2\beta}\right)_{dc_s/d\xi=0} \qquad \text{for } \xi > 0 \tag{6.16}$$

Hence, with increasing ξ, $dc_s/d\xi$ can change its sign continuously along a trajectory only from positive to negative for $\beta > 0$ and from negative to positive for $\beta < 0$. Eq. (6.11) shows that, for $\xi \to \infty$, $dc_s/d\xi$ is positive for $\beta > 0$ and negative for $\beta < 0$. This fact taken together with Eq. (6.16) and the asymptotics presented above for $c_s(\xi)$ near the intersections of the trajectories with the lines $c_s = 0$, $c_s = c_m$, and $\xi = 0$ indicates that trajectories approaching a constant value of c_s for $\xi \to \infty$, Eq. (6.11), can, for $\beta > 0$, originate only on the line $c_s = 0$ with a positive value of $dc_s/d\xi$, whereas, for $\beta < 0$, they can originate only on the line $c_s = c_m$ with a negative value of $dc_s/d\xi$. In particular, along these trajectories and for any finite ξ, $dc_s/d\xi$ will be positive for $\beta > 0$ and negative for $\beta < 0$. The use of this fact in Eq. (6.9) shows then that y_s should be increasing monotonically with ξ along these trajectories and, since, on account of Eq. (6.11), it is negative for $\xi \to \infty$ along trajectories approaching a constant value of c_s it also has to be negative on these trajectories for $\xi \to 0$. By making use of the asymptotics presented above for $y_s(\xi)$ near the intersections of the trajectories with the lines $c_s = 0$, $c_s = c_m$, and $\xi = 0$ we therefore demonstrate that only the trajectories originating at the point $c_s = \xi = 0$ for $\beta > 0$, Eq. (6.12), and at the point $c_s = c_m$, $\xi = 0$ for $\beta < 0$, Eq. (6.13), meet this additional requirement. This clearly shows that, as was the case for Eq. (6.8), there exist no continuous trajectories of Eq. (6.9) satisfying our boundary conditions for which c_s approaches a constant value for $\xi \to \infty$, and $y_s \to 0$ for $\xi \to 0$. Therefore, as was the case considered earlier with two-phase region, in order to construct a discontinuous solution (i.e., a shock solution) that

satisfies our boundary conditions for a particular value of c_0, we need to take part of the trajectory which approaches c_0 for $\xi \to \infty$, Eq. (6.11), and combine it with part of another trajectory for which $y_s \to 0$ when $\xi \to 0$, provided that the relative particle flux, $F_s = -\xi^2 c_s + \text{sign}(\beta) y_s$, is continuous along the composite trajectory. The expression for the derivative of F_s given by Eq. (6.9),

$$\frac{dF_s}{d\xi} = -2\xi c_s, \tag{6.17}$$

indicates that F_s decreases monotonically with increasing ξ along a trajectory.

Now let us consider separately the two cases $\beta > 0$ and $\beta < 0$.

Case A: $\beta > 0$

When $\beta > 0$, the lines $c_s = c_m$, $c_s = 0$, and the trajectory passing through the point $\xi = 0$, $c_s = c_m$ with $y_s = 0$, Eq. (6.15), meet the requirement of $y_s \to 0$ for $\xi \to 0$. But, since for the latter, $dc_s/d\xi < 0$ at the point $\xi = 0$, $c_s = c_m$, Eq. (6.15), $dc_s/d\xi$ is always negative along the entire trajectory for $\xi > 0$. It follows then that this trajectory will intersect the line $c_s = 0$ according to the asymptotic expression for $c_s(\xi)$ near this intersection, say ξ_i, given by $c_s \approx N(\xi_i - \xi)^{1/2}$ and $y_s \to -\beta N^2$ with a positive N and therefore will never be able to satisfy the condition $c_s \to c_0$ as $\xi \to \infty$.

Now let us consider the variation of F_s along trajectories to be taken to form a discontinuous solution of Eq. (6.9). Along a trajectory originating at the point $c_s = \xi = 0$, Eq. (6.12), this function, denoted by $F_s^{(1)}(\xi)$, varies from $F_s^{(1)}(0) = -M$ with $M > 0$ to $F_s^{(1)} \approx -\xi^2 c_0$ for $\xi \to \infty$, Eq. (6.11). In particular, this rules out the line $c_s = 0$ for which $F_s = 0$ given that, in that case

M=0. Next we consider the trajectories originating at the points $\xi = 0$, $c_s = c_m$, Eq. (6.15), and $c_s = \xi = 0$, Eq. (6.12). Since $dc_s/d\xi$ is negative along the former whereas $dc_s/d\xi$ is positive along the latter, two trajectories intersect only once at a certain point, say ξ_*, so that $c_s^{(2)} = c_s^{(1)} = c_*$ at $\xi = \xi_*$, where the superscripts 2 and 1 denote, respectively, the functions c_s vs. ξ along these two trajectories. Let us compare the variation of F_s along the trajectory originating at the point $\xi = 0$, $c_s = c_m$, to be denoted by $F_s^{(2)}(\xi)$, with $F_s^{(1)}(\xi)$. Since $dc_s^{(1)}/d\xi > 0$ and $dc_s^{(2)}/d\xi < 0$, we find that at the intersection of these trajectories

$$F_s^{(1)}(\xi_*) - F_s^{(2)}(\xi_*) = \frac{2\beta c_*(1-c_*)^2}{\hat{\eta}(c_*)(1-c_*\beta)^3}\left(\frac{dc_s^{(1)}}{d\xi} - \frac{dc_s^{(2)}}{d\xi}\right)_{\xi_*} > 0.$$

Because $F_s^{(2)}(0) = 0$ is greater than $F_s^{(1)}(0)$, there exists a point $\xi_1 < \xi_*$ where $F_s^{(1)} = F_s^{(2)}$. As follows from Eq. (6.17), $\frac{d}{d\xi}\left(F_s^{(1)} - F_s^{(2)}\right) = 2\xi\left(c_s^{(2)} - c_s^{(1)}\right)$ and since $c_s^{(2)} > c_* > c_s^{(1)}$ for $\xi < \xi_*$, $\frac{d}{d\xi}\left(F_s^{(1)} - F_s^{(2)}\right)$ is positive for $\xi < \xi_*$ and negative for $\xi > \xi_*$. This shows that there could exist only one root of the equation $F_s^{(1)} = F_s^{(2)}$ for $\xi < \xi_*$ at $\xi = \xi_1$. On the other hand, this also indicates that $\left(F_s^{(1)} - F_s^{(2)}\right)$, as a function of ξ, attains a maximum at the point ξ_*, hence another root of this equation, $\xi_2 < \xi_*$ could also exist. Consequently, we can construct one or two (if ξ_2 exists) composite trajectories satisfying our boundary conditions for $\beta > 0$, by taking part of the trajectory, which originates at the point $c_s = \xi = 0$ and approaches c_0 for $\xi \to \infty$, to the right of ξ_1 or ξ_2 and then combining it with the trajectory, which originates at the point $\xi = 0$, $c_s = c_m$, on the left of ξ_1 or ξ_2, respectively.

Along the line $c_s = c_m$, F_s equals $-\xi^2 c_m$ which is greater than $F_s^{(1)}(0)$ for $\xi = 0$ and smaller than $F_s^{(1)}(\xi)$ for $\xi \to \infty$, Eq. (6.11). Since, moreover, $dF_s^{(1)}/d\xi > -2\xi c_m$, there exists only one point at which $F_s^{(1)}(\xi) = -\xi^2 c_m$. Hence, we can construct another composite trajectory, which satisfies our boundary conditions for $\beta > 0$, by taking part of the trajectory, which originates at the point $c_s = \xi = 0$ and approaches c_0 for $\xi \to \infty$, to the right of the point referred to earlier and combining it with the line $c_s = c_m$ to the left. A similar analysis indicates that the requirement that F_s be continuous can be also satisfied by taking part of the trajectory, which approaches a constant value of c_s for $\xi \to \infty$, and combining it on the left with part of a trajectory originating at the line $c_s = c_m$ with $y_s = 0$, Eq. (6.14) within a certain range of ξ', and later on with the line $c_s = c_m$. However, we have to rule out all composite trajectories which include the line $c_s = c_m$ because Eq. (6.9) neglects the contribution of the compressibility factor, Z in Eq. (3.1), to the chemical potential in Eq. (6.2) for the single-phase region of the phase diagram, Fig. 3.1, that prevails in the vicinity of this line.

Case B: $\beta < 0$

When $\beta < 0$, only the lines $c_s = 0$ and $c_s = c_m$ meet the requirement that $y_s \to 0$ for $\xi \to 0$. But $F_s(\xi)$ taken along any trajectory, which originates at the point $c_s = c_m$, $\xi = 0$, Eq. (6.13), and approaches a constant value of c_s for $\xi \to \infty$, varies from $c_m(1-c_m)^2 L^2/(1-c_m\beta)^3$ at $\xi = 0$, for any L, to $-\xi^2 c_s$, as $\xi \to \infty$, Eq. (6.11). Therefore, since F_s decreases monotonically with increasing ξ, there is only one point on this trajectory where $F_s = 0$. Hence, we can construct only one composite trajectory, which satisfies our boundary conditions for $\beta < 0$, by

taking part of this trajectory approaching a constant value of c_s, as $\xi \to \infty$, on the right of this point and combining it with the line $c_s = 0$ on the left. Making use of the range of the variation of $F_s(\xi)$ presented above and the expression for the slope of $F_s(\xi)$, Eq. (6.17), demonstrates that the requirement that F_s be continuous cannot be satisfied for $\beta < 0$ on the line $c_s = c_m$ where F_s equals $-\xi^2 c_m$.

Typical solutions for $|\beta| = 0.1$ for $\beta < 0$ and $\beta > 0$ are shown in Figs. 6.7 and 6.8, respectively. Notice that the location of jump is very close to the one found for the case of the two-phase region as reported in the previous section.

6.4 Conclusions

In this chapter, we examined, both, analytically and numerically the electro-hydrodynamic model when, via a similarity transformation, we first reduced the model equations to ordinary differential equations for the particle concentration. We found that a continuous solution of the model equations does not exist for either positive or negative dielectrophoresis and that only a discontinuous or "shock solution" is possible. We established the existence of shock solutions to these equations and determined the location of the concentration front and the dependence of the front velocity on the bulk particle concentration of the suspension, the particle polarizability, and the field strength. In particular, we demonstrated that the appearance of the front can be caused either by the electrically induced local phase separation of a suspension or by the rapid local growth of the suspension viscosity due to the field-driven particle accumulation in a certain area.

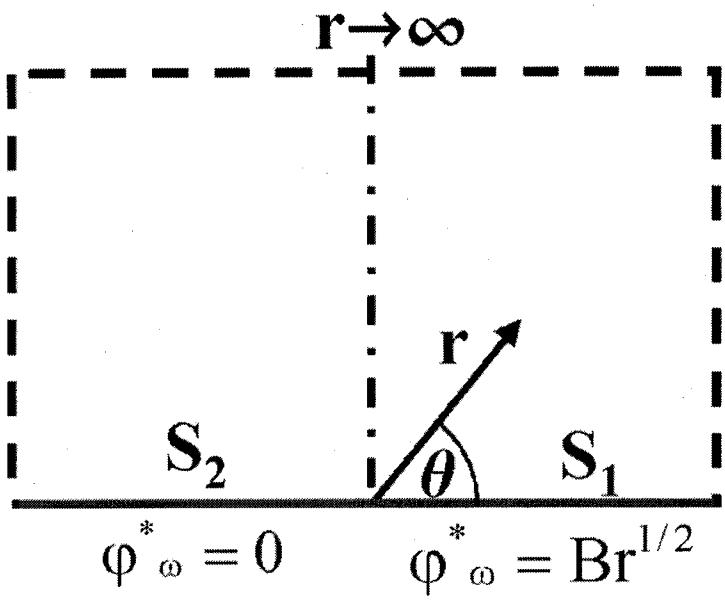

Figure 6.1: Schematic of the geometry under investigation. The left and the right of the bottom electrodes are maintained at ground and high voltage respectively in an infinite domain. Before the application of the electric field, the domain is filled with a suspension of uniform concentration c_0.

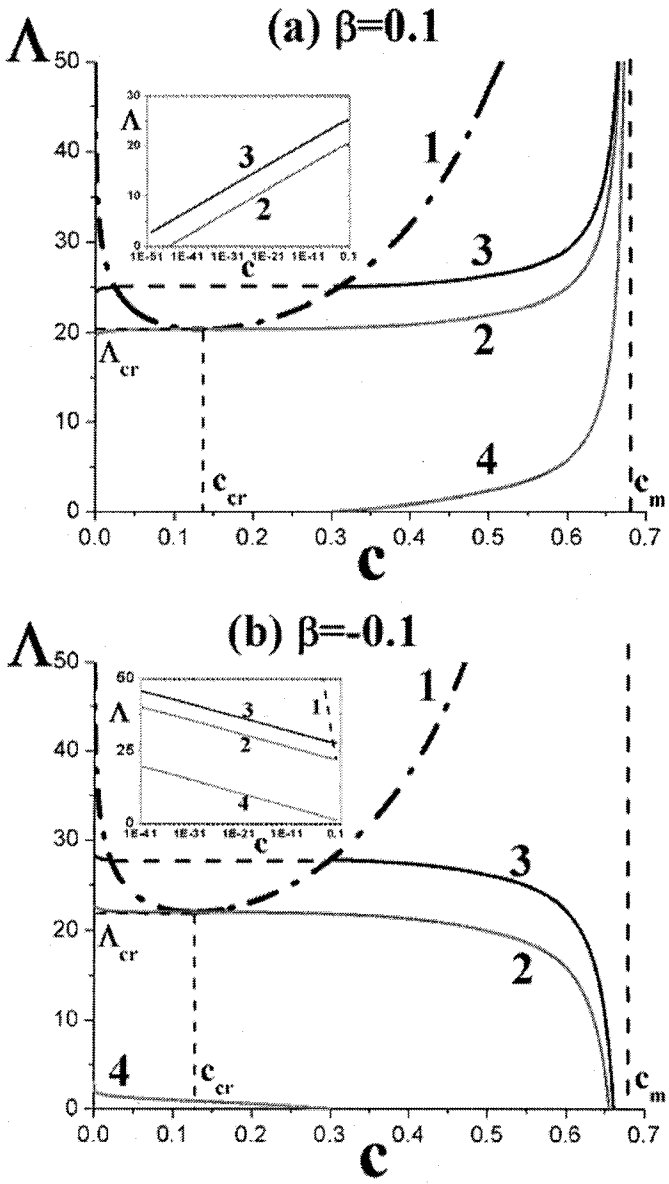

Figure 6.2: Plot showing the trajectories starting with various initial concentrations for (a) $\beta = 0.1$ and (b) $\beta = -0.1$; 1 corresponds to the coexistence curve, 2 is the limiting trajectory, 3 and 4 correspond to the cases when we start with an initial concentration on either side of c_{tr}. Curve 3, refers to the first case discussed in the text, where the equilibrium particle concentration changes abruptly when it intersects the coexistence curve, while for curve 4, which refers to the second case in the text, the spatial variation of the equilibrium particle concentration is smooth because the trajectory lies entirely within the single phase region. Here $\Lambda = 3\beta^2\lambda$ where $\lambda = \varepsilon_0\varepsilon_f\langle E^2\rangle v_p / k_B T$ is the relative strength of the field.

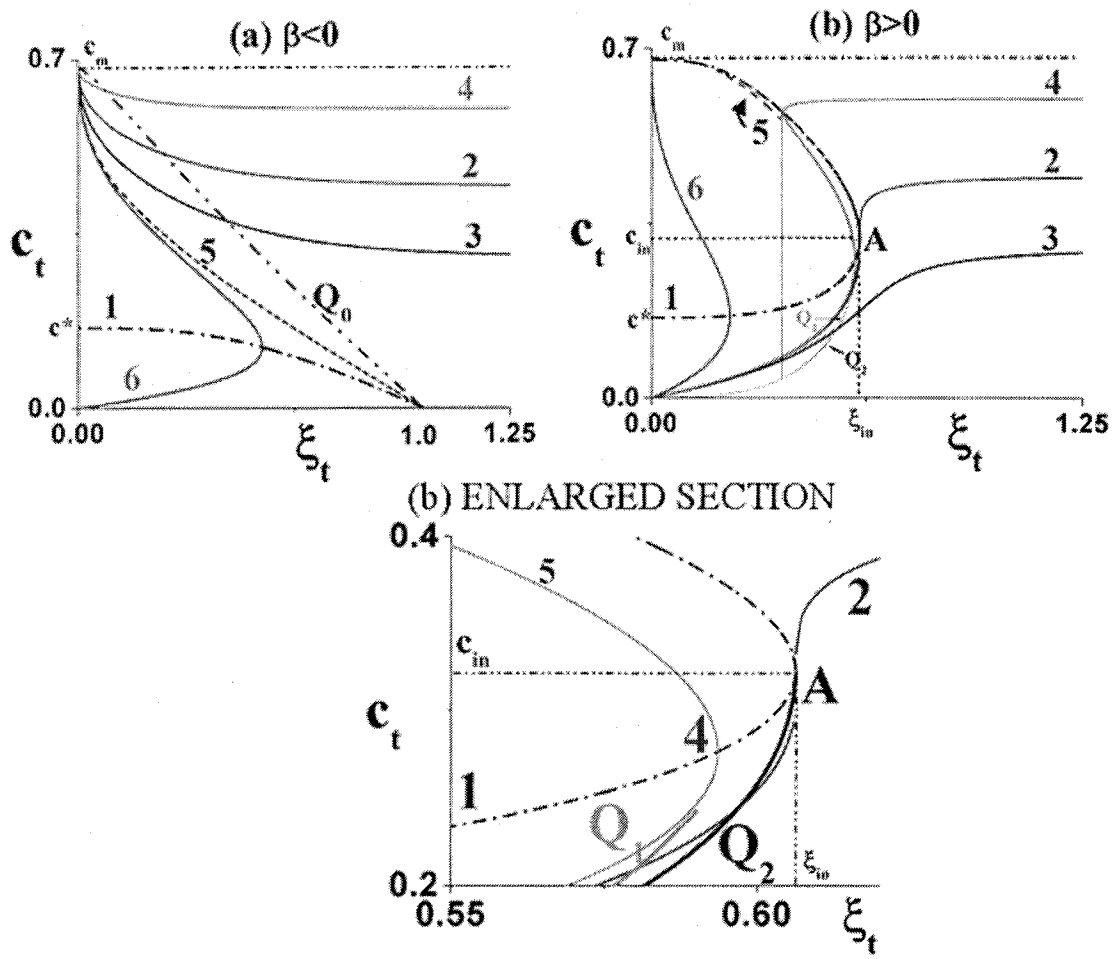

Figure 6.3: Plot showing the behavior of the trajectories for (a) $\beta < 0$, and (b) $\beta > 0$ along with an enlarged section close to $\xi_t = \xi_{in}$, where $\xi_{in} = 0.606, c_{in} = 0.32$. The isoclines of Eq. (6.8) (aside from the horizontal and vertical lines) are shown by curve 1; curves 2,3,4 represent the solution of Eq. (6.8) with c_0= 0.445, 0.30, and 0.60, respectively, as $\xi_t \to \infty$. Curve 5, refers to the limiting trajectory passing through $\xi_t = 0$, $c_t = c_m$. Curve 6, refers to the family of curves starting from $\xi_t = 0$, and $c_t = c_m$, which lie to the left of the limiting trajectory and after intersecting the isoclines approach $\xi_t = 0$, and $c_t = 0$. Q_0 specifies the location of the shock and the magnitude of the concentration jump for $\beta < 0$, Q_1 specifies the location of the shock and the magnitude of the concentration jump for $\beta > 0$, $c_0 \le c_{lim}$. Note that, for $c_0 > c_{lim}$, the trajectory, curve 4, after intersecting the upper branch of the isocline (curve 1) falls vertically until it reaches Q_2; thereafter it proceeds accordingly to the solution of Eq. (6.8) until it intersects Q_1 and then jumps upwards until it intersects curve 5. This is shown in Fig. 6.6b in for a specific case.

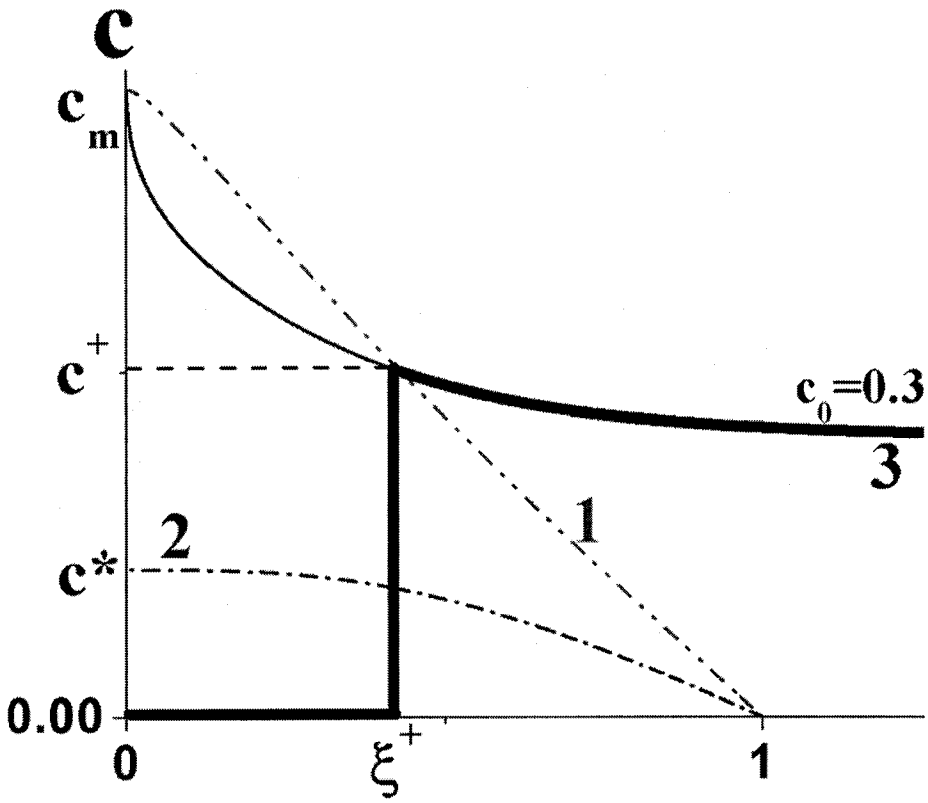

Figure 6.4: Plot showing the concentration profile for the case $\beta < 0$, for an initial concentration $c_0 = 0.3$. 1 denotes the curve Q_0, 2 is the isocline given by Eq. (6.8) and 3 is the trajectory from the solution of Eq. (6.8) originating from $\xi_t \to \infty$, with $c_0 = 0.3$. The shock is located at $\xi^+ = 0.42$, where the concentration suddenly drops from $c^+ = 0.37$ to 0.

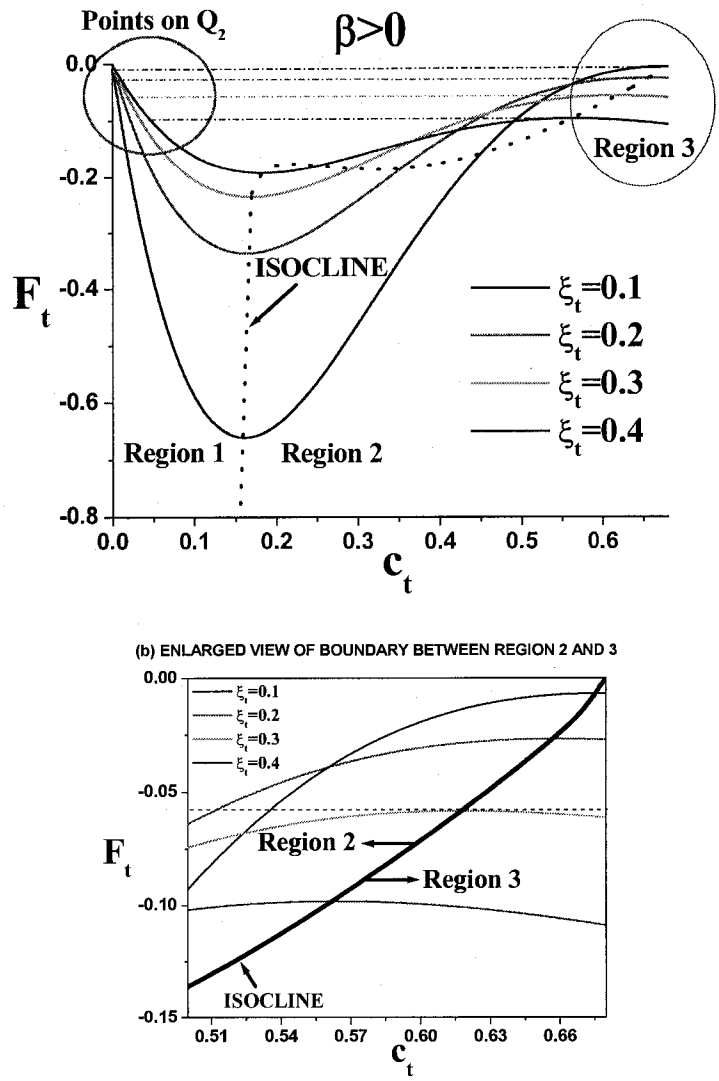

Figure 6.5: (a) Plot showing the variation of F_t vs. c_t at different values of ξ_t for $\beta > 0$. Notice that, in Regions 1 and 3, lying respectively, below and above the isocline given by trajectory 1 in Fig. 6.3b, F_t decreases monotonically with increasing c_t at a fixed value of ξ_t, in contrast to Region 2 (the region bounded by the isocline in Fig. 6.3b) where F_t decreases with increasing c_t. Also, there exist a single and unique point, which lies on the transition from Region 2 to Region 3 and lies on the isocline given by trajectory 1 in Fig. 6.3b, corresponding to which another point could be found in Region 1 having the same value of F_t which forms the curve Q_2 described in the text. Also since trajectory 5 lies inside the Region 2, hence the curve Q_1, which corresponds to same value of F_t as on trajectory 5 in Fig. 6.3b, lies at higher value of c_t then on Q_2, i.e. Q_1 is located above Q_2 as shown in Fig. 6.3b. (b) Shows the enlarged section of the boundary between region 2 and region 3.

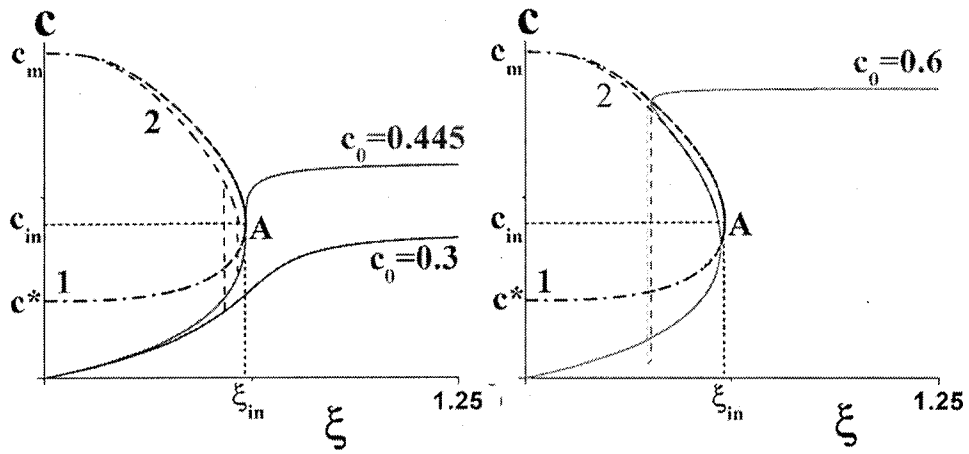

Figure 6.6: Plot showing the concentration profiles for $\beta > 0$ and for initial concentrations $c_0 = 0.3$, 0.445 (on the left) and $c_0 = 0.6$ (on the right), respectively. Trajectories shown by 1-2, corresponds to isocline given by Eq. (6.8) and trajectory starting with $c = c_m, y_t = 0$ from $\xi_t = 0$. For $c_0 \leq 0.445$, the solution is constructed by matching the trajectory originating from $\xi_t \to \infty$, with the trajectory given by curve 2 at the point where the trajectory originating from $c = c_0, \xi_t \to \infty$ intersects the curve Q_1, while $c_0 > 0.445$, the solution is constructed by jumping from the intersection of the trajectory originating from $c = c_0, \xi_t \to \infty$, with isocline onto Q_2 followed by continuation using the solution of the equation, then taking a jump from the intersection of the continued solution with curve Q_1 followed by jumping onto the trajectory starting with $c = c_m, y_t = 0$ from $\xi_t = 0$.

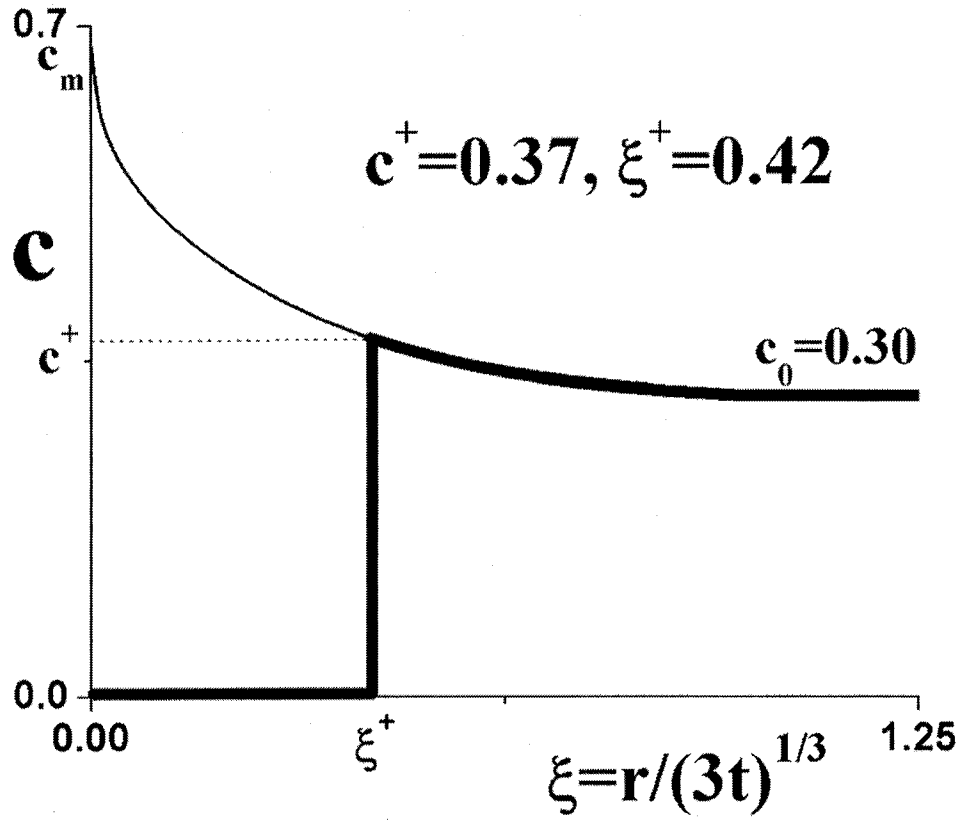

Figure 6.7: Plot showing the solution of the concentration profile for the case of $\beta = -0.1$, for an initial concentration $c_0 = 0.3$. The shock is located at $\xi^+ = 0.42$, where the concentration suddenly drops from $c^+ = 0.37$ to 0. For the case of $\beta < 0$, a unique solution always exists.

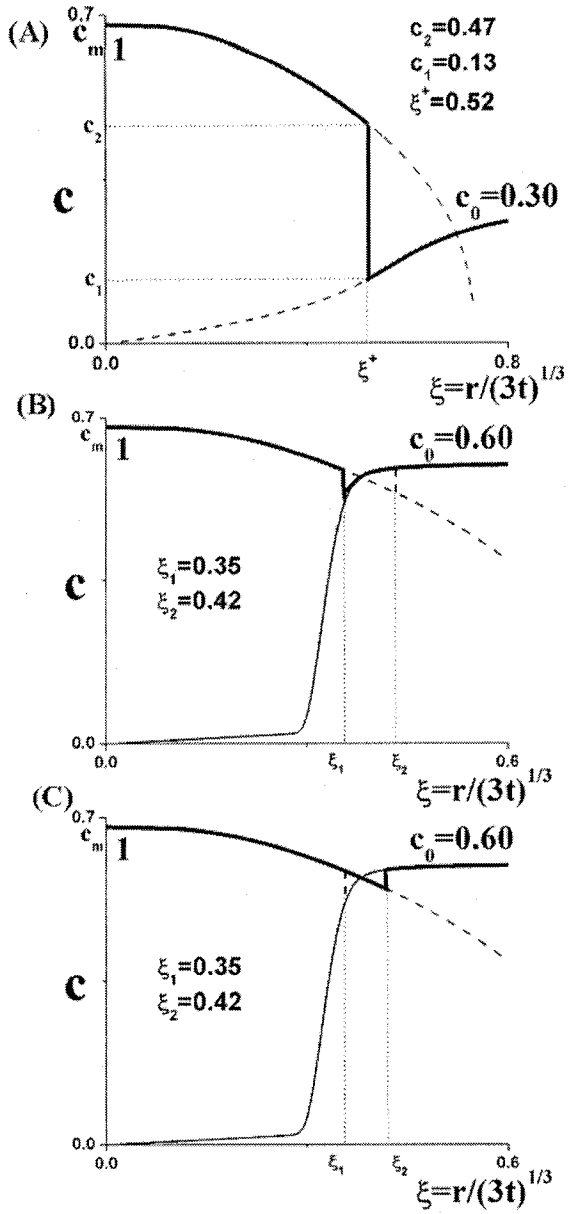

Figure 6.8: Plot showing the solution of the concentration profile for the case of $\beta = 0.1$, for initial concentrations of $c_0 = 0.3$ (A) and $c_0 = 0.6$ (B and C), respectively. Trajectory 1 refers to the trajectory starting with $c = c_m, y_s = 0$ from $\xi = 0$. For $c_0 = 0.3$, the solution is constructed by matching the trajectory originating from $\xi \to \infty$, with curve 1 by matching the jump condition. For $c_0 \leq c_{\text{lim}}$, where $c_{\text{lim}} \sim 0.446$, there exist a unique solution of the concentration profile (shown in A). For $c_0 = 0.6$, there exist two possible locations where the jump condition can be satisfied (shown in B and C). At this point one need to have an extra condition to determine the physical solution.

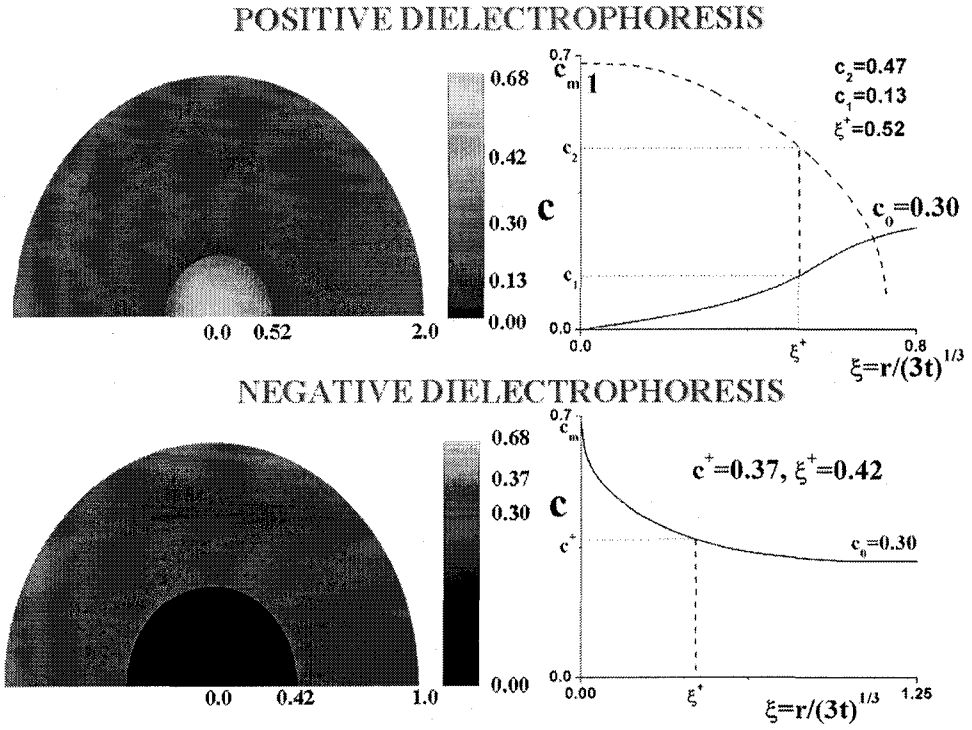

Figure 6.9: Schematic showing the snapshot of the concentration profile for a fixed time, $t > 0$, for the case of $\beta = 0.1$ and $\beta = -0.1$, starting from an initial concentration $c_0 = 0.3$.

Table 6.1
Expansions for $\beta < 0$

ISOCLINES

$\xi_t^3 + \text{sign}(\beta)\frac{d}{dc_t}\left[\frac{c_t(1-c_t)^2}{\hat{\eta}(c_t)}\right] = 0$ [Shown by 1, Fig. 6.3(a)], $\xi_t = 0$, $c_t = 0$, $c_t = c_m$ [where $1/\hat{\eta}(c_t) = 0$]

Starting from	Expansion for c_t	Expansion for y_t	Comments
$c_t = 0, \xi_t = 0$	$c_t \approx M\xi_t + 2M^2(1+1/c_m)\xi_t^2$	$y_t \to -M$	$M \geq 0$, Finite y_t except for M=0 where $c_t = 0$ and $y_t \to 0$, shown by 6 in Fig. 6.3(a).
$c_t = c_m, \xi_t = 0$	$c_t \approx c_m(1 - L\xi_t^{1/2})$	$y_t \to -c_m(1-c_m)^2 L^2$	$L \geq 0$, Finite y_t except for L=0 where $c_t = c_m$ and $y_t \to 0$, shown by 2,3,4,6 in Fig. 6.3(a)
$c_t = c_0, \xi_t \to \infty$	$c_t \approx c_0 - \frac{\text{sign}(\beta)c_0(1-c_0)^2}{3\hat{\eta}(c_0)\xi_t^3}$	$y_t \approx -\frac{c_0(1-c_0)^2}{\hat{\eta}(c_0)\xi_t}$	$c_t \to c_0, y_t \to 0$ as $\xi_t \to \infty$, shown in 2,3,4 for c_0=0.445, 0.3 and 0.6, respectively in Fig. 6.3(a)
$c_t = 0, \xi_t = 1$	$c_t \approx -c_m(\xi_t - 1)/(1+c_m)$	$y_t \approx c_m(\xi_t - 1)/(1+c_m)$	Shown in 5, this line divides the trajectories approaching $c_t = c_m$ into two parts, those above it approaches $\xi_t \to \infty$ with $c_t \to c_0$ and $y_t \to 0$, while those on the left goes to $c_t = 0, \xi_t = 0$ after intersecting the isocline given by curve 1.

* Clearly no continuous solution exist which satisfy $c_t \to c_0$ as $\xi_t \to \infty$ with $y_t \to 0$ to be matched with any expansion starting from $\xi_t = 0$ with $y_t \to 0$. M and L are the constants determining the initial slope of the trajectory.

Table 6.2

Expansions for $\beta > 0$

ISOCLINES

$\xi_t^3 + \text{sign}(\beta)\frac{d}{dc_t}\left[\frac{c_t(1-c_t)^2}{\hat{\eta}(c_t)}\right] = 0$ [Shown by trajectory 1, Fig. 6.3(b)], $\xi_t = 0$, $c_t = 0$, $c_t = c_m$ [where $1/\hat{\eta}(c_t) = 0$]

Starting from	Expansion for c_t	Expansion for y_t
$c_t = 0, \xi_t = 0$	$c_t \approx M\xi_t + 2M^2(1+1/c_m)\xi_t^2$	$y_t \to -M$
* $M \geq 0$, Finite y_t except for M=0 where $c_t = 0$ and $y_t \to 0$, shown by trajectory 6 in Fig. 6.3b		
$c_t = c_m, \xi_t = 0$	$c_t \approx c_m - 3c_m\xi_t^3/5(1-c_m)^2$	$y_t \approx -9c_m\xi_t^5/25(1-c_m)^2$
*Start from $c_t = c_m$ with $y_t \to 0$ as $\xi_t \to 0$, shown by 5 in Fig. 6.3(b). This trajectory separates the trajectories originating from $c_t = 0$, $\xi_t = 0$ given above into two parts, those originating with smaller M, approaches $c_t = c_0$ as $\xi_t \to \infty$ (shown by trajectories 2,3,4) from those originating with larger M, approaches $c_t = c_m$ with finite value of y_t (shown by trajectory 6) shown on Fig. 6.3(b).		
$c_t = c_0, \xi_t \to \infty$	$c_t \approx c_0 - \frac{\text{sign}(\beta)c_0(1-c_0)^2}{3\hat{\eta}(c_0)\xi_t^3}$	$y_t \approx -\frac{c_0(1-c_0)^2}{\hat{\eta}(c_0)\xi_t}$
* $c_t \to c_0, y_t \to 0$ as $\xi_t \to \infty$, shown in trajectories 2,3,4 for c_0=0.445, 0.3 and 0.6, respectively in Fig. 6.3(b). Trajectories with $c_0 \leq 0.445$ approach $c_t \to 0$ with finite value of y_t without intersecting the isocline given by trajectory 1 except for the special case when trajectory originating from $c_0 = 0.445$ touches the isocline at its inflection point [A] with the coordinates $c_{in} = 0.32$ and $\xi_{in} = 0.606$ where c_{in} is the root of the equation $\frac{d^2}{dc_t^2}\left[\frac{c_t(1-c_t)^2}{\hat{\eta}(c_t)}\right] = 0$ and $\xi_{in}^3 = -\frac{d}{dc_t}\left[\frac{c_t(1-c_t)^2}{\hat{\eta}(c_t)}\right]$ for $c_t = c_{in}$, while for $c_0 > 0.445$, the trajectories intersect curve 1, changes the sign of the derivative and crosses again the isocline before approaching $c_t \to 0$ with finite value of y_t.		
* Clearly no continuous solution exist which satisfy $c_t \to c_0$ as $\xi_t \to \infty$ with $y_t \to 0$ to be matched with any expansion starting from $\xi_t = 0$ with $y_t \to 0$. M is a constant determining initial slope of the trajectory originating from $c_t = 0, \xi_t = 0$.		

Chapter 7

Novel electric-field-driven mesoscale phase transitions in polarized suspensions subject to a uniform ac field

In contrast to the earlier Chapters, here we shall describe a phenomenon of pattern formation in suspensions subjected to a spatially **uniform** ac electric field.

7.1 Introduction

The electric and magnetic manipulation and assembly of tiny polarized particles dispersed in a host fluid is widespread in industrial applications. Important examples include the field-controllable ferrofluids [**32**] and electro-rheological (ER) [**33**] and magneto-rheological (MR) suspensions [**34**] for interfacing mechanical systems to electronic controls; electric and magnetic techniques for handling and separating particles in micro-fluidics [**35**]; creating well aligned structures in block copolymers [**36**] and ceramics [**37**] for the designed control of materials properties; photonic devices, optical switches, and modulators for affecting the propagation of electromagnetic waves [**38-40**]; and sensors for environmental monitoring and biodetection [**18**]. While each of these applications is independently unique, from the physical point of view all of them share the common feature of utilizing highly interesting and still obscure phase separation phenomena that are driven by the anisotropic long-range dipole-dipole interactions. In

addition to their technological applications, the fundamental significance of these so-called dipolar fluids is that they constitute the simplest examples that can yield insight into dipolar interactions occurring throughout nature.

The natural scale of the interparticle dipolar interactions, Λ, is the ratio of the interaction energy between two parallel dipoles in contact relative to the thermal energy [**41**, **42**]. Despite of the fact that the energy of two dipoles averaged over their relative orientation equals zero, the average of such dipolar interactions over a random arrangement of polarized spheres appears to be attractive due to their long-range nature [**1**] thereby rendering unstable the gas-like distribution of the particles above a threshold value of Λ which depends on the particle volume fraction φ. This is because, when dipole-dipole interactions exceed Brownian forces, the dipolar potential favors the arrangement, in which dipoles self assemble head-to-tail in polymer-like chains aligned in the field direction that minimizes their free energy [**41**]. The chaining of polarized particles, a well-known phenomenon for hundreds of years [**7**, **9**], is well understood. It constitutes, however, only the initial stage of the field-driven micro-structural transitions in polarized suspensions. The next stage, termed the lateral aggregation of dipolar chains, has become the subject of intensive theoretical and experimental investigations in the past decade [**43**] because it eventually determines the suspension properties and, furthermore, presents a model for studying the structural evolution in an ensemble of interacting one-dimensional structures that arises in various different contexts, ranging from Abrikosov's flux lines in superconductors to molecular crystals. The surfaces confining the specimen affect the interchain interactions through the relative strength of an image dipole formed by a given dipole located near them because another "real" dipole sees the field created by this

dipole and its image [**44-46**]. In the magnetic case, these surfaces are often made of low permeability materials which do not affect dipoles at the chain ends. In equilibrium, thin films of magnetic fluids confined between two glass plates and subjected to a magnetic field display two-dimensional labyrinthine stripes and hexagonal arrays of columns in the plane perpendicular to the field [**32**]. Their non-equilibrium structures, which are formed when the time it takes for the particles to aggregate together is comparable with the ramping rate of the field or when the column motion is frozen, range from a glassy state of separate columns and sheet-like stripes to labyrinthine patterns [**47**, **48**]. Although detailed questions still remain, the pattern formation in magnetic suspensions is similar to the domain shapes of modulated structures that are observed in many other systems with dipolar interactions (such as Langmuir films of polar molecules, ferromagnetic garnet films, and type-I superconductors), which are governed by the competition between the field-induced long-range dipolar repulsion, $\sim 1/r^3$, and a variety of short-range forces favoring a spatially uniform concentration of particles that can be described within the framework of the Ginzburg-Landau model [**49**].

In the electric case, a specimen is typically confined with conducting electrodes which screen dipoles at the chain ends via images having the same dipole moment [**44**]. This determines the ground states ($\Lambda \to \infty$) of ER suspensions to be a body-centered-tetragonal (BCT) crystals [**46**]. It is generally believed that screening the chain ends favors the formation of BCT domains within columns but does not affect substantially the aggregation at a larger scale in a relatively thick layer of an ER suspension. Experiments on ER suspensions [**50-52**] demonstrate the appearance of chains and interconnected labyrinthine sheets similar to that in magnetic fluids, which then evolve slowly into

collections of BCT structures [**52**]. Direct computer simulations of the field-driven particle motions [**53-55**] and modeling the field-driven pattern formation in dielectric suspensions within the Ginzburg-Landau model [**56**] also do not reveal significant differences between in MR and ER suspensions. Theories for the long-range lateral electric interaction of two infinite dipolar chains [**44**, **55**] appear to be consistent with experiments on the dynamics of finite magnetic chains [**53**].

Our study was motivated by an unsuccessful attempt to combine various patterns reported in the literature on electric and magnetic transitions into a universal "Λ vs. φ" map, assuming that the large-scale aggregation is only governed by the interparticle interactions. In fact, we found that a number of other factors (gravity, fluid surface tension, electro-convection, charge transfer, etc.) strongly affected the patterns observed in the literature. Our experiments on the electric-field driven aggregation in both microgravity (aboard the NASA KC-135 aircraft) and ground-based environments [**27**] also demonstrated that gravity, even if relatively week in comparison with the interparticle dipole-dipole forces (~ 19%), exerts an unexpectedly pronounced influence on the chain formation by releasing loosely connected particles and forming finer and shorter structures.

7.2 Suspension Properties

To eliminate all artifacts, we, therefore, conducted experiments on suspensions of polyolefin spheres in corn oil ($\rho_f = 0.92\,g/cm^3$, $\eta_f = 59.7cp$) at 23^0C whose densities were precisely matched to suppress gravity decomposition on a millimeter scale for several hours. The particle size distribution on a number basis was measured with a Beckman-Coulter laser diffraction particle size analyzer LS 230 and the average diameter

of the particles was found to be $87\,\mu m$ with 80% of them having diameters between 68 and $116\,\mu m$. We carried out experiments on suspensions of particles $90\,\mu m$ and $45\,\mu m$ in diameter and varied the particle volume fraction from 0.5% to 10%. The experimental setup is shown in Fig. 1a. The gap between the electrodes varied from 0.69 mm to 3.53 mm. The frequency range of the applied field, 0.1-3.0 kHz, was chosen to suppress any effects due to electro-convection, electrophoresis, and charge transfer whose contribution decreases with increasing field frequency. Since the particle polarizability did not vary within this frequency range [**31**], the insensitivity of the patterns to the frequency provides a rigorous test that only interparticle interactions are involved. The magnitude of Λ varied from approximately $7 \cdot 10^6$ to $2 \cdot 10^8$. The quantification of images was carried out utilizing image analysis software SIGMASCAN Pro 5 (SYSTAT Software Inc., Illinois).

7.3 Experimental Data

To our surprise, we observed a new class of electric field driven mesoscale phase transitions in polarized suspensions in the plane perpendicular to the field. Specifically, we found that, within a certain range of parameters, the application of a sufficiently strong field (~kV/mm) to a suspension (Fig. 7.1b) generated a stable cellular pattern of fluid domains surrounded by chain-enriched walls (Fig. 7.1c). The time evolution of this pattern is illustrated in (Figs. 7.1d-h). To start with (Fig. 7.1d) shows the initial random particle arrangement in the gap. Following the application of the field, these particles rearrange themselves rapidly (~ms) into an ensemble of chains and columns bridging the electrodes, which are uniformly distributed over the plane perpendicular to the field (Figs. 7.1e and 7.1f). After several minutes, particle-free domains began to appear (Fig.

7.1g) which expanded gradually as the surrounding chains and columns moved away from the core of these particles depleted regions (Figs. 7.1g and 7.1h). Eventually, the growth of the particle-free domain ceased and the final cellular pattern emerged (Fig. 7.2c). The insert in (Figs. 7.1e-h) shows how the process of the cellular structure formation is accompanied by the lateral coalescence of the chains and columns.

The photos presented in Figs. 7.2a, 7.2b demonstrate that the shape of a container affects only the formation and growth of nuclei adjacent to its boundary. To quantify the cellular pattern, we measured the aerial number density of cells, N_c, and the average area of chain-depleted domains, A_f, which formed in cylindrical containers (Figs. 7.2). The values of N_c and A_f measured under the same conditions were found to be reproducible to within $\pm 5-7\%$ and with all other parameters maintained fixed also remained unaffected (again within $\pm 5-7\%$) by changes in the diameter of the container from 1.5" to 2.5" (Figs. 7.2c-d_1), and the sizes in the particles diameter (Figs. 7.2i-j_1). However, the particles of smaller size formed the sharper cellular pattern (Figs. 7.2i- $2j_1$). The average size of the cells is seen to decrease with a decrease in the gap size L (Figs. 7.2e-$2f_1$) and an increase in the particle concentration (Figs. 7.2g-$2h_1$). The photo in Fig. 7.2k, taken at an angle of $\sim 30^0$ to the horizontal plane, illustrates the structure and arrangement of the columns surrounding the fluid domains. Varying the field frequency (Fig. 7.3) and the ramping rate of the field application (Fig. 7.3) does not affect the average cell size and the nucleation kinetics while, increasing the field strength, increases only slightly the cell size (Figs. 7.3) but, as we shall see, reduces the time for the appearance of first nucleus as well as accelerates significantly the nucleation and growth rate of the particle-depleted domains.

To characterize the cellular pattern, we calculated the average radii of the cells, $R_c = 1/\sqrt{\pi N_c}$, and that of the fluid domains, $R_f = \sqrt{A_f/\pi}$, plus the thickness of the chain-enriched wall of a cell, $W = 2(R_c - R_f)$, and the concentration of the particles in the wall $c_w = c/\left[1-(R_f/R_c)^2\right]$ and plotted them as functions of the gap size, L, and c in Fig. 7.4. Regression analysis of these data yields

$$R_c \sim 1.22 L^{1.0\pm0.1} E^{0.3\pm0.1}/c^{0.3\pm0.1}; \qquad R_f \sim 0.18 L^{1.1\pm0.1} E^{0.3\pm0.1}/c^{0.45\pm0.05};$$

$$c_w \sim c/\left[1-(0.10)c^{-0.40\pm0.03}\right] \qquad (7.1)$$

where R_c, R_f, W, and L are measured in mm, the root-mean-square (rms) field strength, E, is given in kV/mm, and c is the volume fraction of the particles. The scale of the cellular pattern increases with an increase in the gap size L (nearly proportional) and, only slightly, with the field strength but decreases with increasing initial particle concentration. Notice that c_w appears to be insensitive to the gap size and the field strength. As it follows from Eqs. (7.1), the wall width at the particle concentration c is always smaller than the cell diameter, as if it were as the concentration c_w, i.e., $W|_c \le 2R|_{c_w}$. Therefore, once the cellular pattern has been formed, it becomes impossible for the field-driven phase transition to proceed further because new cells cannot form inside the walls.

The photos presented in Fig. 7.5 illustrate the formation of a typical cellular pattern through the nucleation and growth of the fluid domains at random sites until the columns stop moving. As can be seen from these photos, all nuclei form over a short period of time (~ 2min) which is substantially shorter than the period of their growth (~20min). To quantify the dynamics of the pattern formation, we measured the time variation of the

fraction of the specimen area occupied by fluid domains. We found that the relative size of such domains, $R(t)/R_f$, increases linearly with time up to about $R(t)/R_f$ =0.6 beyond which it gradually stops growing owing to the presence of other nuclei (Fig. 7.6). It appears that both successive processes can be represented by the so-called Avrami equation (Fig. 7.6)

$$R^2/R_f^2 = 1 - \exp\left[-G^2(t-t_0)^2/R_f^2\right] \quad \text{with} \quad R = G(t-t_0) \text{ for } R << R_f, \qquad (7.2)$$

where t_0 is the average time it takes nuclei to form and G is their initial growth rate. A regression analysis of the data on the linear part of the evolution of the fluid domains (Fig. 7.6) demonstrates that G and t_0 depend only on the field strength and the particle concentration as $G(\text{mm/s}) \sim 0.007\, E^{1.8\pm0.3}/c^{0.73\pm0.21}$ and $t_0\ (\text{s}) \sim (4.21 \pm 1.27)/E^{1.45\pm0.22}\, c^{0.4\pm0.1}$ with the rms E being given in kV/mm. The success of using the Avrami equation indicates that there exists a close similarity between the field-driven formation of the cellular patterns and nucleation phenomena in solid and liquid solutions triggered by a change in the temperature and/or the composition [**66**].

The quantify the lateral coalescence of the chains and columns (inserts in Figs. 7.1e-1h), we selected randomly ~ 100-200 aggregates in the plane perpendicular to the field, which were located inside the cell walls of the stable cellular pattern, and measured their area and shape factors. Since their average aspect ratio was found never to exceed 2, we computed their mean radius, R_{agg}, and the width of the size distribution, σ_{agg} (Fig. 7.7). A regression analysis demonstrates that the average size of these aggregates is increasing and their size distribution is broadening with an increase in the gap, L, and the particle volume fraction but the both parameters are not affected by the diameter of the suspended

particles and the field strength $R_{agg}(\text{mm}) \sim L^{0.46\pm0.06} c^{0.41\pm0.05}$ and $\sigma_{agg}(\text{mm}) \sim L^{0.62\pm0.09} c^{0.46\pm0.11}$, where L is measured in mm. These results correlate qualitatively with the data on the lateral coarsening of the magnetic field induced structures in ferrofluid emulsions [**47**].

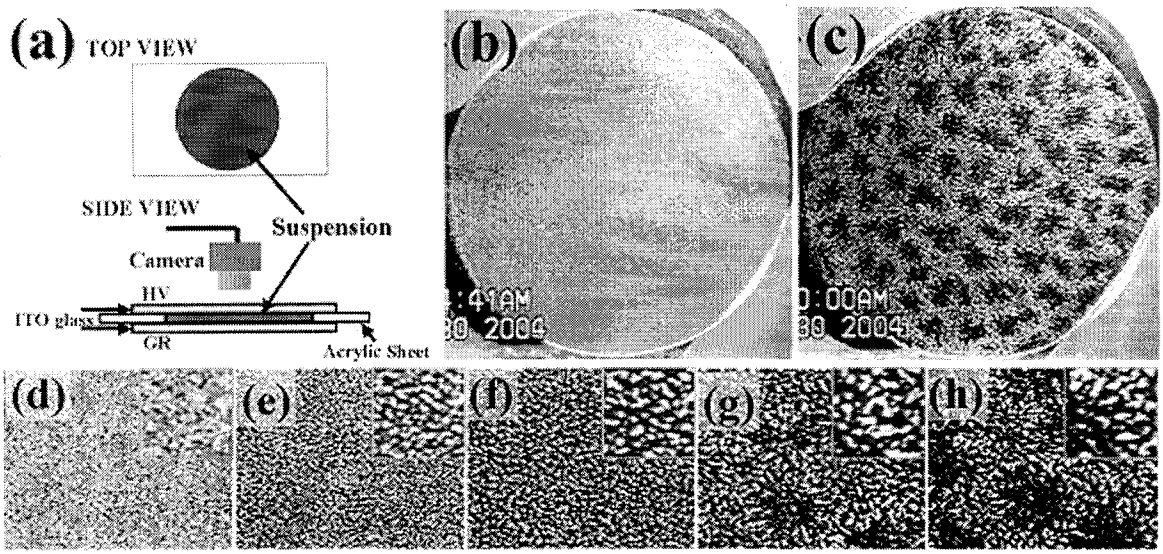

Figure 7.1: (a) Schematic of the experimental setup; (b)-(h) show the particle arrangement in the plane perpendicular to the applied field; (b) and (c) refers to the macroscopic particle arrangement within the experimental cavity before and 30min following the application of the field, respectively, while (d)-(h) show the enlarged sections at 0, 1, 5, 15, and 24min, respectively, following the field application. The inset in (d)-(h) shows the twice-zoomed images of the aggregates inside the wall regime. The experiment was conducted for: c=0.03(v/v), L=1.79mm, 3kV/100Hz, d_p=90μm, D=1.5 inch. The particles are seen as white spots and a black region refers a region devoid of particles throughout the length of the cavity along the field direction.

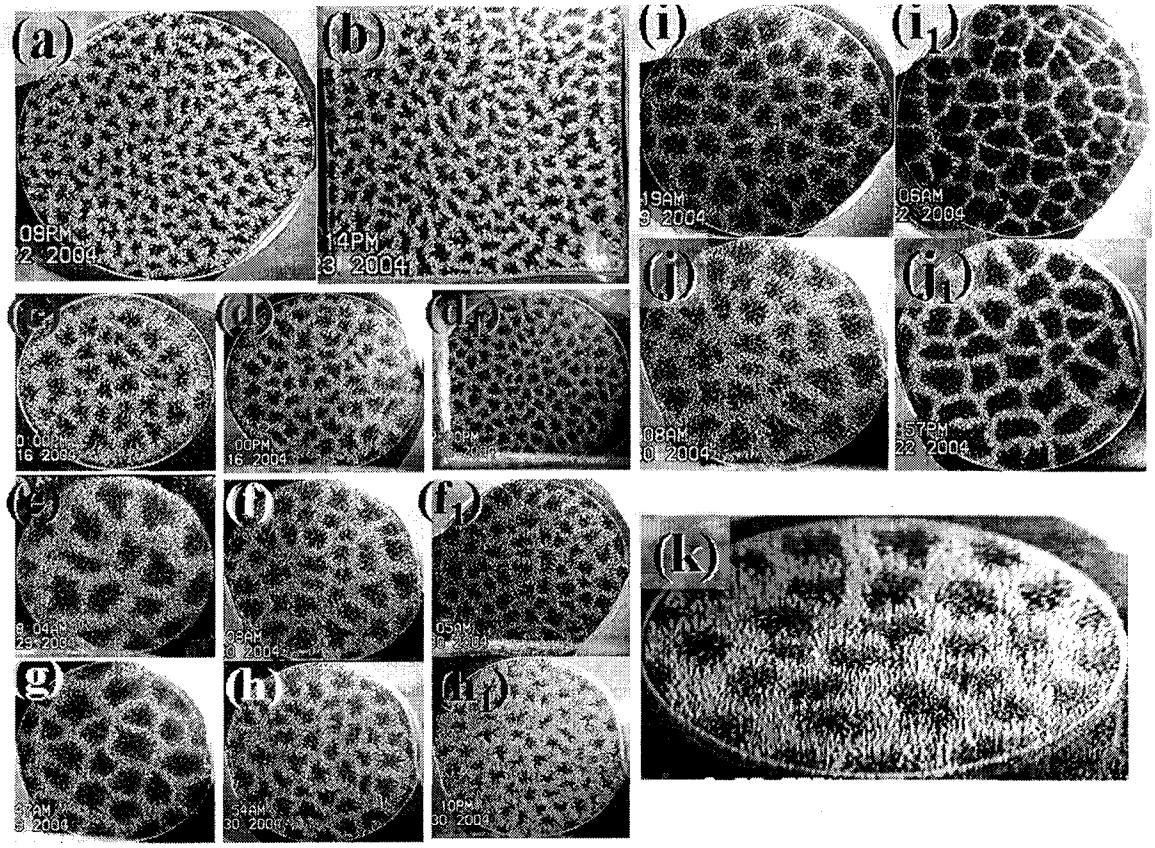

Figure 7.2: (a)-(k) refers to the experimental pictures taken ~30min following the field application; where (a)-(j_1) shows the particle arrangement as seen in the plane perpendicular to the applied field while (k) illustrates the structure observed at an angle (~30^0) to the horizontal plane. In all photographs, the particles are seen as white spots and a black region refers to a region devoid of particles throughout the length of the cavity along the field direction.

Figs. (a) and (b) shows the effect of varying the shape of the cavity from (a) a cylindrical with diameter, D=2" to (b) a cuboid having dimensions of 2" by 2", respectively. Experimental parameters: 3kV/100Hz, L=1.79mm, c=0.05(v/v), d_p=45μm. The aerial average number density of the cells in (a) and (b) are 50.32 and 46.75 cells/inch^2, respectively.

Figs (c)-(d_1) shows the effect of varying the diameter of the cylindrical cavity for D= (c) 1.5 inch, (d) 2.02 inch, and (d_1) 2.5 inch, respectively. Experimental parameters: 3kV/100Hz, L=1.79mm, c=0.02, d_p=90μm. The aerial average number density of the cells for (c)-(d_1) are 17.54, 16.86, and 21.6 cells/inch^2, respectively.

Figs. (e)-(f_1) shows the effect of changing the confinement between the electrodes for L= (e) 3.53mm, (f) 2.3mm, and (f_1) 1.7mm, respectively. Experimental parameters: E=1.7kV/mm, f=100Hz, c=0.02(v/v), D=2.02", d_p=90μm. (e)-(f_1) corresponds to N_{cells} = 17, 37, and 66, respectively.

Figs. (g)-(h_1) shows the effect of changing the initial particle concentration for c= (g) 0.01, (h) 0.03, and (h_1) 0.05 (v/v), respectively. Experimental parameters: E=1.7kV/mm, f=100Hz, D=2.0", L=2.3mm, d_p=90μm. (g)-(h_1) corresponds to N_{cells} = 28, 45, and 63, respectively.

Figs. (i)- (j_1) shows the effect of varying the particle diameter, d_p, where (i) and (j) are for d_p=90μm whereas (i_1) and (j_1) are for d_p=45μm. (i) and (i_1) corresponds to c=0.01, L=1.7mm while (j) and (j_1) corresponds to c=0.02, L=2.3mm. Experimental parameters: E=1.7kV/mm, f=100Hz, D=2 inch. (i)-(j_1) corresponds to N_{cells}= (i) 54, (i_1) 59, (j) 36, and (j_1) 37, respectively.

Fig. (k) shows the particle columns spanning the gap between the electrodes when observed from an angle ~30^0 to the horizontal plane. Experimental parameters: c=0.02(v/v), L=1.79mm, 3kV/100Hz, d_p=90μm, D=1.5 inch.

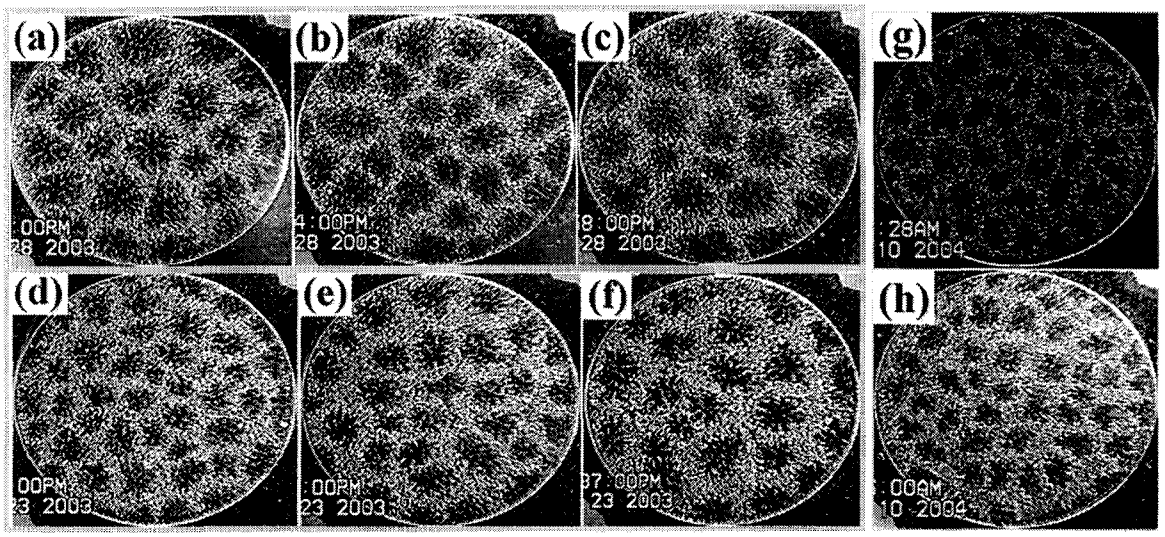

Figure 7.3: Shows the effect of varying the frequency [(a)-(c)], the magnitude of the field strength [(d)-(f)], and the ramp of the applied field [(g)-(h)] on the final structural morphology.

Figs. (a)-(c) correspond to frequencies, f= (a) 100Hz, (b) 1kHz and (c) 3kHz, respectively. The experimental pictures were taken ~30min following the field application. Experimental parameters: E=1.7kV/mm, D=1.5 inch, L=1.79mm, c=0.01, d_p=90μm. (a)-(c) corresponds to N_{cells} = 24, 26, and 23 respectively.

Figs. (d)-(f) were taken after 60min, 30min and 20min, respectively following the application of the electric field of strength, E= 1.2, 1.7, 2.2kV/mm. f=100Hz, D=1.5 inch, L=1.79mm, c=0.02, d_p=90μm. (d)-(f) corresponds to N_{cells} = 39, 29, and 24 respectively.

Photos, (g) and (h) were, taken after 55min following the application of an applied field, for increasing and decreasing ramp, respectively. The experiment for increasing ramp was conducted by applying an instantaneous field of 0.28V/mm followed by an increase at 0.028V/(mm.min) at steps of one minute, till the final value of 1.82kV/mm was reached over a period of 55 min, while for decreasing ramp, we applied 1.82kV/mm followed by a decrease at 0.028V/(mm.min) at steps of one minute, till the final value of 0.28kV/mm over a period of 55 min was achieved. D=1.5 inch, L=1.79mm, c=0.02, d_p=90μm, f=100Hz.

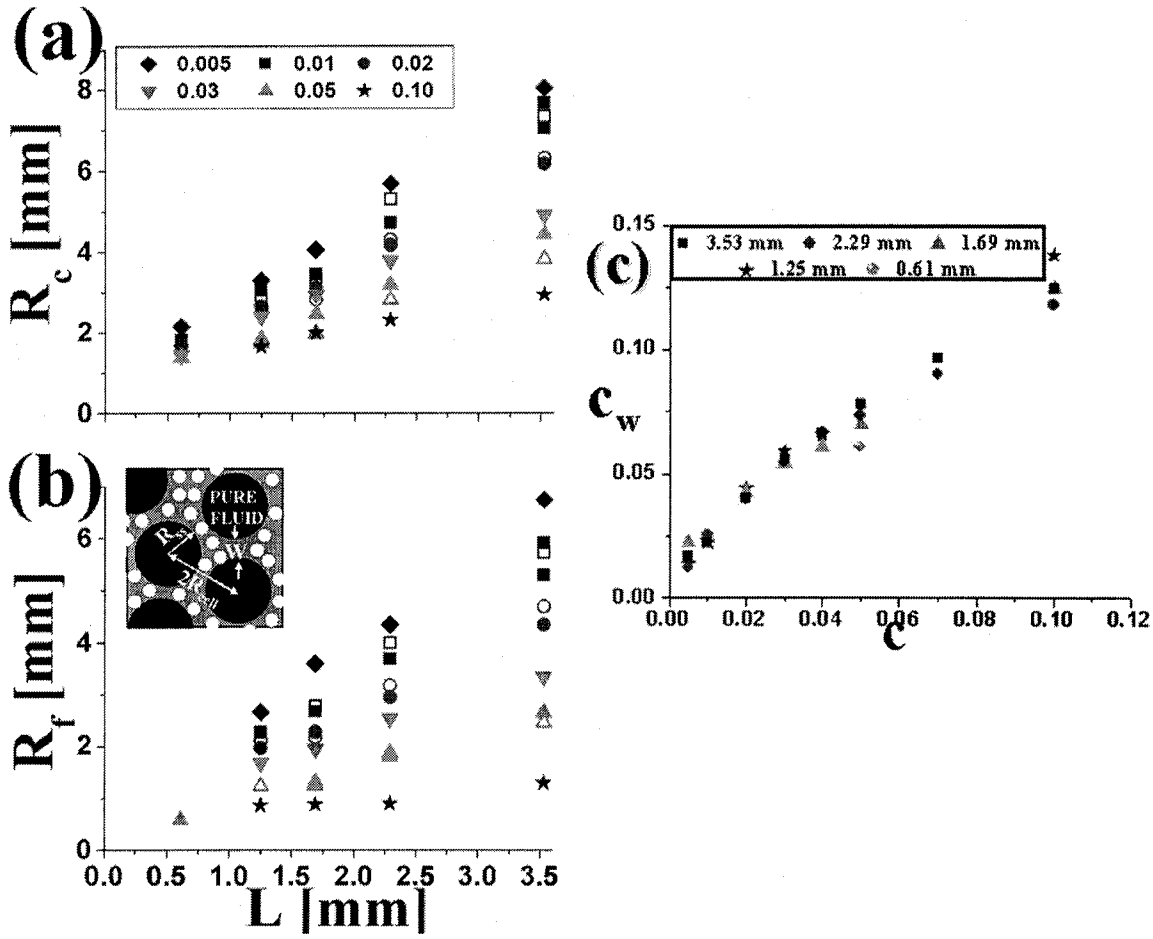

Figure 7.4: (a) and (b) shows the average radius of the cell, $R_c = 1/\sqrt{\pi N_c}$, and that of the cell core, R_f, defined respectively as shown schematically in the inset on (b), for L=0.61-3.53mm, c=0.005-0.10(v/v), for a fixed strength (E~1.7kV/mm) and frequency (f=100Hz) of the ac applied field in the cylindrical cavity of diameter, D=2 inch. (c) Shows the computed volume average particle concentration inside the wall region, $c_w = cR_c^2/(R_c^2 - R_f^2)$ for various initial concentrations. The legends in (a) and (b) refer to the various initial concentrations whereas in (c) they refer to the gap between the electrodes. Filled and hollow symbols refer to the data for 90 and 45μm particles, respectively. A regression analysis yields $R_c \sim 1.22L^{1.0}E^{0.3}/c^{0.3}$ mm and $R_f \sim L^{1.1}E^{0.3}/c^{0.45}$, where a series of additional experiments for D=1.5 inch were considered wherein the field strength was varied from 1.25 to 2.83kV/mm and the frequency from 100Hz to 3kHz.

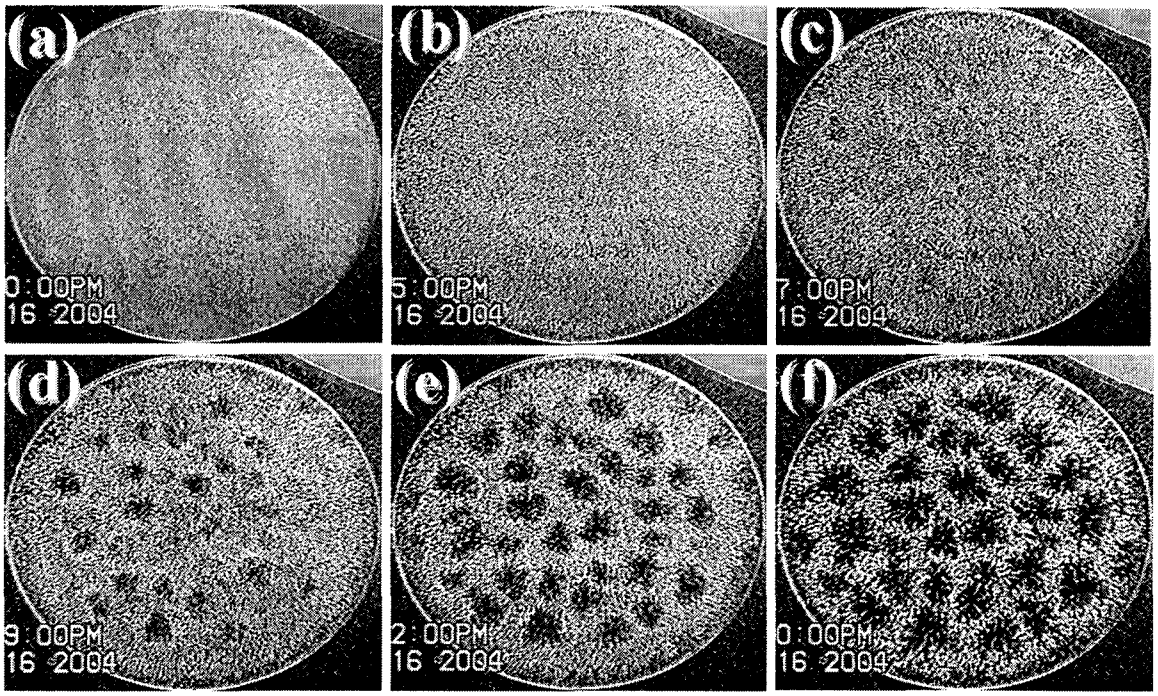

Figure 7.5: Temporal evolution of the cellular structure in the plane perpendicular to the applied field; (a)-(f) corresponds to structures at initial, 5min, 7min, 9min, 12min, and 30min, respectively, following the exposure of the suspension to an applied ac electric field of 3kV/100Hz; c=0.02(v/v), D=1.5 inch, L=1.7mm,d_p=90μm. The particles are seen as white spots and a black region refers to a region devoid of particles throughout the length of the cavity along the field direction.

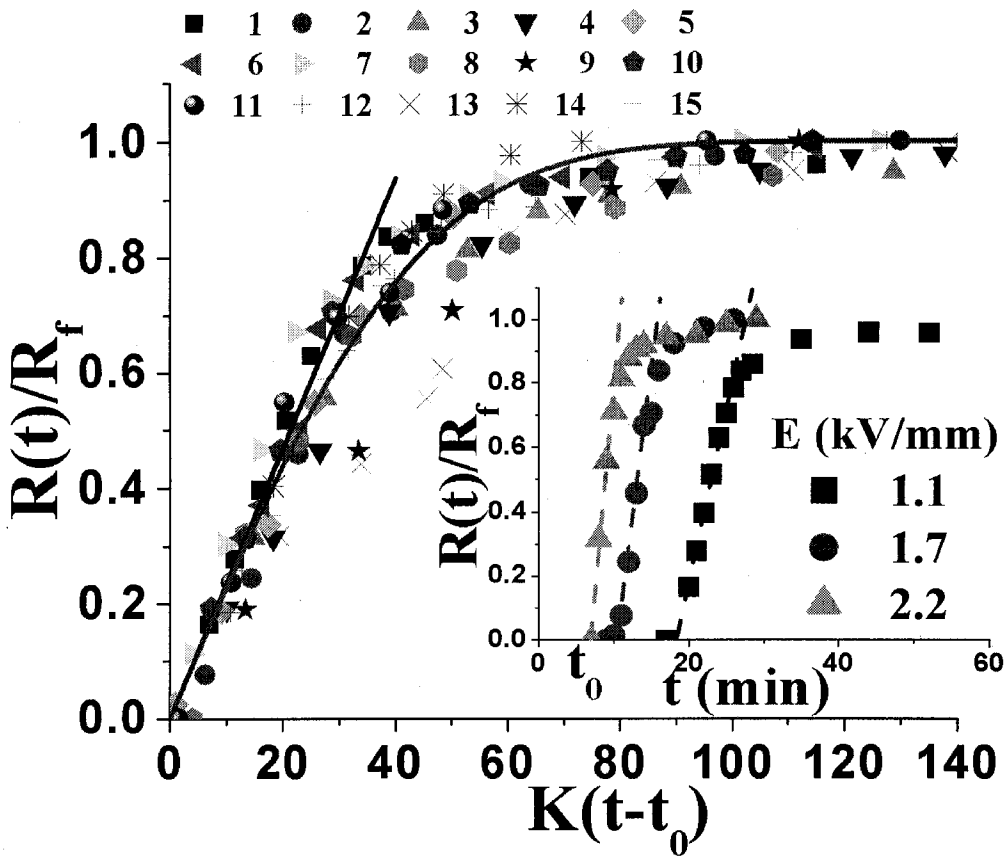

Figure 7.6: The average growth kinetics of nuclei for various experiments with E=1.1-2.2kV/mm, c=0.01-0.05, d_p=45 and 90μm, f=0.1-3kHz, D=1.5 inch [with detailed description in [**Table 7.1**], is shown by various symbols. Red and black lines are the predictions of Avrami's hypothesis in non-interacting and interacting regions of nuclei's growth. The plot in the inset shows the effect of different strengths of applied field on the growth, where t_0 signifies the appearance of the first nucleation site and the initial linear slope is the growth rate, G. A regression analysis yields $t_0 \sim 4.21/(E^{1.45}c^{0.4})$ sec and $K \sim 0.02344E^{1.49}/c^{0.43}L^{1.1}$ $(sec)^{-1}$.

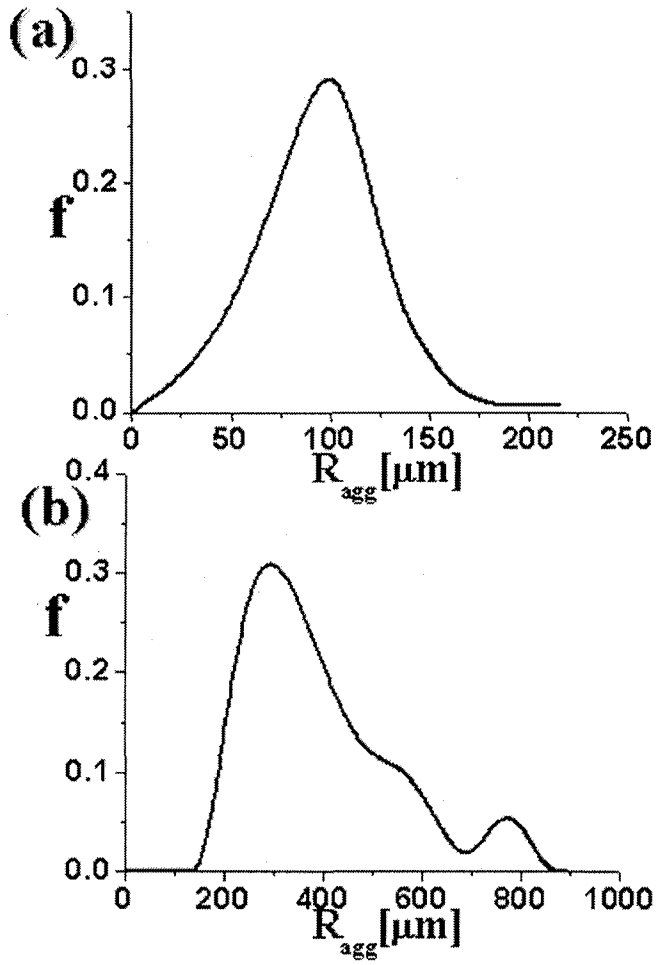

Figure 7.7: Plot depicting the aggregate size distribution for (a) c=0.03, L=0.61mm; (b) c=0.10, L=3.53mm where f represents the relative fraction of the aggregate size. A regression analysis based on data, for which c=0.01-0.1(v/v), L=0.61-3.53mm, d_p=45 and 90μm, E~1.7kV/mm, yields $\langle R_{agg} \rangle \sim L^{0.46\pm0.06} c^{0.41\pm0.05}$ and $\langle \sigma_{agg} \rangle \sim L^{0.62\pm0.09} c^{0.46\pm0.11}$.

Table 7.1

Experimental Parameters for Kinetic Study [Fig. 7.6]

Expt. No.	c (v/v)	L [mm]	$d_p(\mu m)$	f [Hz]	E[kV/mm]
1	0.01	1.79	90	100	1.12
2	0.01	1.79	90	100	1.68
3	0.01	1.79	90	100	2.23
4	0.01	1.79	90	1000	1.68
5	0.01	1.79	90	3000	1.68
6	0.02	1.79	45	100	1.12
7	0.02	1.79	45	100	1.68
8	0.02	1.79	45	100	2.23
9	0.02	1.79	90	100	1.12
10	0.02	1.79	90	100	1.68
11	0.02	1.79	90	100	2.23
12	0.02	3.20	90	100	1.25
13	0.02	3.20	90	100	1.56
14	0.05	3.20	90	100	1.25
15	0.05	3.20	90	100	1.56

All the experiments refer to above were performed in a cylindrical cavity of diameter, D=1.5 inch.

Chapter 8

Future Work

This thesis focuses on various aspects of electric field positive and negative dielectrophoresis. We demonstrated that dielectrophoresis could be used as a means of concentrating particles in prespecified locations. We also demonstrated that the common belief of "clinorotation" to simulate microgravity conditions on the ground, fails under some conditions. The theoretical modeling provided in Chapter 6, provides an understanding of yet another mechanism of concentration front formation, as observed in Chapter 5, other than well-know electric field induced phase transition. Our work toward manufacturing suspensions of silica nanoparticles could be utilized in testing such suspensions in microdevices, wherein high-gradients (~kV/mm) could be utilized while working at relatively higher frequencies of the applied field strength, where the effect of fluid conductivity could be substantially reduced. This suspension could be used to study various features such as the particle behavior at relatively higher concentrations by studying the tracers. In Chapter 7, we present a new electric field induced phase transition, which happens over much longer time scale than the chain/column formation. It would be worth studying this phase transition using computer simulations starting from a system of particle chains spanning the gap between the electrodes having defects inside them so as to interact them with the neighboring chains. The experimental results for the kinetics and morphological aspects of the pattern formed could be utilized to understand

the scaling behavior for computational purposes. Yet another extension of this work could to study the process by studying time variation of the three-dimensional structures by mean of confocal microscopy. It would also be interesting to study the "particle ring formation" at the three-phase interface as presented in the Appendix 7B. This work would require one to investigate the development of model for first finding the shape and thereafter solving the electric field distribution using Maxwell equations and I believe that this transition could be explained by a combined phenomenon of "electric field induced phase transition" followed by "negative dielectrophoresis" exhibited by the polyolefin particles.

In brief, this thesis presents a good starting point for a reader to understand the basics of dielectrophoresis and field-induced phenomenon.

Appendix 2A

Measurement procedure for the Dielectric Spectrometer BDS-80 with temperature control at 20^0C

1. Put the sample in the cell and place the cell in between the electrodes.
2. Turn on main switch and the pump.
3. Start the WinDETA software.
4. Set measurement files.
5. Set Sample specifications:
   - Thickness of cell=0.27mm
   - Diameter of cell=19.21mm
6. Click on List order and choose permittivity' [] and permittivity"[].
7. Click on Value list:
   - Set temperature=20^0C
   - Specify the frequencies of interest.
8. Specify start and end conditions.
9. Initialize the temperature controller.
10. Specify temperature controller stabilization conditions
11. Activate temperature controller:
    - Set point 20^0C
    - Temperature derivation 10^0C
    - Temperature control of the sample
12. Start the measurements.

Appendix 2B

Measurement procedure for COULTER LS230 device

1. Clean the sample cell with fresh DI water, and then put the fresh water into the cell.
2. Put the pump off.
3. Click on the *LS230 Control* program icon on the desktop.
4. Click on *run->run sample*:
   - For new samples make sure that *Auto rinse, Repeat cycle, and Include PIDS data* options are off, for particles size >0.4 microns, otherwise choose PIDS options on.
   - Click on *start*.
5. A window with graph will appear. During this time prepare the particle suspension
6. A message will appear which will indicate to add sample.
7. Add sample and adjust the value of the obscuration (range~8-12%) to such a value, till OK appears on the title of the graph window.

   NOTE: in order to increase the obscuration add more sample and to reduce it, just dilute the sample.
8. Press done when obscuration value is in right range.
9. Click on run->run cycle
10. Fill sample information and run information.
11. Wait until the measurement is done and the result window appears.
12. Save the information and exit.

Appendix 2C

Procedure for working with COULTER N4 Plus

1. Load the sample in the sample cell.
2. Start the program by clicking on N4Plus icon.
3. Click on the 123 icon and fill the basic information and click next.
4. In the preparation parameters window: enter preparation name and click: edit diluent button.
    - Choose water and temperature greater than 20^0C (viscosity and refractive index data will automatically appear).
    - Click on the close button and then on Next in the preparation window.
5. N4Plus-Instrument Settings window will appear. Enter some comments and click more>> button.
    - Set run time to 90 sec.
    - Change the value for the temperature to the one that was entered in previous section.
6. Click on the start to begin the measurement.

Appendix 3A

1. Deriving the expression for the critical point

The critical point on the phase diagram corresponds the inflection point of $\mu_p(c)$ as a function of c, hence:

$$\frac{\partial \mu_p(c)}{\partial c} = \frac{\partial^2 \mu_p(c)}{\partial c^2} = 0, \text{ where } \mu_p(c) = \frac{k_B T}{v_p}\frac{df_0}{dc} - \varepsilon_0\left(\frac{\partial \varepsilon'_s}{\partial c}\right)_{\omega t_c}\left\langle \frac{E^2}{2}\right\rangle \quad (1)$$

- $\varepsilon'_s = \dfrac{1+2\beta c}{1-\beta c}$, where $\varepsilon'_s = \mathrm{Re}(\varepsilon^*_s)$, and $\beta = \mathrm{Re}(\beta^*)$, yield $\left(\dfrac{\partial \varepsilon'_s}{\partial c}\right)_{\omega t_c} = \dfrac{3\varepsilon_f \beta}{(1-\beta c)^2}$ (2)

- $f_0 = c\ln\left(\dfrac{c}{e}\right) + c\int_0^c \dfrac{Z(c)-1}{c}dc$, with $Z(c) = \begin{cases} \dfrac{1+c+c^2-c^3}{(1-c)^3} & 0 < c \le 0.5 \\ \dfrac{A}{(c_m - c)} & 0.5 < c \le c_m \end{cases}$ (3)

- $f'_0 = \ln(c) + Z(c) - 1 + \int_0^c \dfrac{Z(c)-1}{c}dc$; $f''_0 = Z' + \dfrac{Z}{c}$; (4)

Using these expressions we can write

$$\frac{\partial \mu_p(c)}{\partial c} = \left[Z' + \frac{Z}{c}\right] - \frac{\Lambda}{(1-\beta c)^3} = 0, \text{ which}$$

h implies the first condition

$$Z + cZ' = \frac{\Lambda c}{(1-\beta c)^3} \quad (5)$$

and hence $\dfrac{\partial^2 \mu_p(c)}{\partial c^2} = \left[Z'' + \dfrac{Z'}{c} - \dfrac{Z}{c^2}\right] - \dfrac{3\beta\Lambda}{(1-\beta c)^4} = 0$; which on simplification and using Eq(1) gives:

$$Z'' + \frac{Z'}{c} - \frac{1}{c^2}\left\{\frac{\Lambda c}{(1-\beta c)^3} - cZ'\right\} - \frac{3\beta\Lambda}{(1-\beta c)^4} = 0, \text{ multiplying with c throughout we obtain:}$$

$$cZ'' + Z' + Z' = \frac{\Lambda(3\beta c + 1 - \beta c)}{(1-\beta c)^4} \text{ or } cZ'' + 2Z' = \frac{\Lambda(1+2\beta c)}{(1-\beta c)^4} \quad (6)$$

Equations (5) and (6) have been shown in the text for determining the location of the critical points.

2. Derivation of the asymptotic forms of f'_0 for the special limits, $c_1 \to 0$ and $c_2 \to c_m$

Close to the low values of c, $c_1 \to 0$:
Substituting the expressions of f'_0 from Eq. (4) and using the expression of Z (c) from Eq.(3) for small values of $c \to 0$, we have:

$$f'_0 = \ln(c) + Z(c) - 1 + \int_0^c \frac{Z(c)-1}{c} dc \text{, where } Z = \frac{1 + c + c^2 - c^3}{(1-c)^3}$$

hence

$$f'_0 = \ln(c) + (1 + c + c^2 - c^3)(1-c)^{-3} - 1 + \int_0^c \frac{(1 + c + c^2 - c^3) - (1-c)^3}{(1-c)^3 c} dc \text{, neglecting } O(c^3)$$

terms inside this equation we end up:

$$f'_0 = \ln(c) + (4c + 10c^2 + ..) + \int_0^c \frac{(4c + 10c^2 + ...)}{c} dc \text{, and upon integration we get:}$$

$$f'_0 = \ln(c) + (4c + 10c^2 + ..) + (4c + 5c^2 + ..) = \ln(c) + 8c + 15c^2 + O(c^3) \qquad (7)$$

For the limit $c_2 \to c_m$:

$$Z = \frac{A}{(c_m - c)} \text{; we have } f'_0 = \ln(c) + \frac{A}{(c_m - c)} - 1 + \int_0^{0.5} \frac{Z(c)-1}{c} dc + \int_{0.5}^c \frac{(A - c_m) + c}{(c_m - c)c} dc \text{; where}$$

for the integral for $0 < c \le 0.5$, we need to use the appropriate expression for Z given by Eq. (3).

Upon integrating the above expression could be reduced to:

$$f'_0 = \ln\left(\frac{c}{e}\right) + \frac{A}{(c_m - c)} + \int_0^{0.5} \frac{Z(c)-1}{c} dc + \frac{(A - c_m)}{c_m} \ln(c)\Big|_{0.5}^c + \frac{A}{c_m} \ln(c_m - c)\Big|_{0.5}^c$$

Upon substituting the values we get:

$$f'_0 = \ln\left(\frac{c}{e}\right) + \frac{A}{(c_m - c)} + \int_0^{0.5} \frac{Z(c)-1}{c} dc + \frac{(A - c_m)}{c_m} \ln(2c) + \frac{A}{c_m} \ln\left(\frac{c_m - c}{c_m - 0.5}\right) \text{ which can be}$$

written as:

$$f'_0 = -\ln(2e) + \frac{A}{(c_m - c)} + \int_0^{0.5} \frac{Z(c)-1}{c} dc + \frac{A}{c_m} \ln(2c) + \frac{A}{c_m} \ln\left(\frac{c_m - c}{c_m - 0.5}\right) \qquad (8)$$

Eqs. (7) and (8) have been provided in the text.

3. Detailed derivation for the expressions for the Chemical Potential in the two-phase region

The basic condition for defining the coexistence curve is that the chemical potential as well as the osmotic pressure in the two phases should be equal, i.e.

$\mu_p(c_1) = \mu_p(c_2)$ and $\Pi_p(c_1) = \Pi_p(c_2)$

On letting $\beta^2\lambda \to \infty$, we find that $c_1 \to 0$ and $c_2 \to c_m$:

This leads to the two equations:

$$f'_0(c_1) - \frac{3\beta\lambda}{2(1-\beta c_1)^2} = f'_0(c_2) - \frac{3\beta\lambda}{2(1-\beta c_2)^2} \tag{9}$$

and

$$c_1 Z(c_1) - \frac{3c_1^{\,2}\beta^2\lambda}{2(1-\beta c_1)^2} = c_2 Z(c_2) - \frac{3c_2^{\,2}\beta^2\lambda}{2(1-\beta c_2)^2} \tag{10}$$

where, $f'_0(c_1) = \ln(c_1) + 8c_1 + 15c_1^{\,2} + \ldots\ldots;$

$$f'_0(c_2) = -\ln(2e) + \frac{A}{(c_m - c_2)} + \int_0^{0.5} \frac{Z(c)-1}{c}\,dc + \frac{A}{c_m}\ln(2c_2) + \frac{A}{c_m}\ln\left(\frac{c_m - c_2}{c_m - 0.5}\right)$$

and

$$Z(c_1) = \frac{1 + c_1 + c_1^{\,2} - c_1^{\,3}}{(1-c_1)^3}\ ;\ Z(c_2) = \frac{A}{(c_m - c_2)}$$

Clearly for $c_1 \to 0$, we can eliminate left hand side of Eq. (10) and thereby obtain:

$c_2 \dfrac{A}{(c_m - c_2)} - \dfrac{3c_2^{\,2}\beta^2\lambda}{2(1-\beta c_2)^2} = 0$ which for $c_2 \to c_m$ becomes to a first approximation:

$$c_2 = c_m - \frac{2A(1-\beta c_m)^2}{3c_m\beta^2\lambda} + \ldots\ldots \text{ where } c_2 > 0.5 \tag{11}$$

Upon substituting the above expression for c_2 into Eq. (9) we thereby obtain that:

$\ln(c_1) - \dfrac{3\beta\lambda}{2} = \dfrac{A}{(c_m - c_2)} + \dfrac{A}{c_m}\ln\left(\dfrac{c_m - c_2}{c_m - 0.5}\right) - \dfrac{3\beta\lambda}{2(1-\beta c_2)^2}$; which can further be simplified into:

$$\ln(c_1) = \frac{A}{(c_m - c_2)} + \frac{A}{c_m}\ln\left(\frac{c_m - c_2}{c_m - 0.5}\right) - \frac{3\beta\lambda}{2}\left\{\frac{1}{(1-\beta c_2)^2} - 1\right\}$$

Or

$$\ln(c_1) = \frac{A}{(c_m - c_2)} + \frac{A}{c_m}\ln\left(\frac{c_m - c_2}{c_m - 0.5}\right) - \frac{3\beta^2\lambda c_2}{2}\left\{\frac{1}{(1-\beta c_2)^2} + \frac{1}{(1-\beta c_2)}\right\}$$

where, from Eq. (11), $c_m - c_2 = \frac{2A(1-\beta c_m)^2}{3c_m\beta^2\lambda} + ...$

Therefore,

$$\ln(c_1) = \frac{A}{(c_m - c_2)} + \frac{A}{c_m}\ln\left(\frac{c_m - c_2}{c_m - 0.5}\right) - \frac{3\beta^2\lambda c_2}{2}\left\{\frac{1}{(1-\beta c_2)}\right\} - \frac{A}{(c_m - c_2)}$$

or

$$\ln(c_1) = \frac{A}{c_m}\ln\left(\frac{c_m - c_2}{c_m - 0.5}\right) - \frac{3\beta^2\lambda c_2}{2}\left\{\frac{1}{(1-\beta c_2)}\right\} \qquad (12)$$

These equations have been used in Chapter 3 for determining the expression of the chemical potential in, both, the single phase as well as the two-phase regions, i.e. Eqs. (3.3-3.6), of the suspension phase diagram shown in Fig. (3.1).

Appendix 5A

A Novel Approach for studying the behavior of concentrated suspensions

5A.1 Introduction

In this section we shall present a brief overview of the experimental procedure along with our preliminary experimental results for the manufacturing of a suspension in which the particles are refractive index matched with the suspending fluid. This study was motivated by the fact that, when we applied the electric field to the concentrated suspensions (~5%-15%(v/v)) discussed in Chapter 5, we were unable to use any optical technique for studying the motion of the particles and their subsequent distribution because of the opacity of the suspension. To this end, we started looking for a system in which the particles had a narrow size distribution plus the same refractive index but quite different electrical properties than the suspending fluid. The idea was to subsequently change the refractive index of some of these particles, without affecting their electrical properties, so as to use them as tracers for observing the details of the particle motions and their distribution in concentrated suspensions. In what follows, we shall describe the experimental procedure and present our preliminary experimental results on the suspension behavior under the action of an ac-electric field.

5A.2 Experimental Procedures

We grew, in a controlled fashion, colloidal spherical particles of nearly uniform size [d_p~600nm] following the recipe of Dr. James Martin [**57**]. These particles were

synthesized via the base catalyzed nucleation and growth of colloidal silica from Tetraethyl orthosilicate (TEOS). The synthesis was conducted in the mixed organic solvent system which includes a 75% benzyl alcohol/ 25% formamide mixture that closely index-matches the growing spheres and reduces Keesom interactions. The latter are due to the fact that polar molecules try to arrange themselves from head to tail, positive to negative, an orientation, which leads to a further increase in the intermolecular interactions thereby promoting aggregation. In one batch, 200 ml of the sample was manufactured using the following amount of chemical reagents:

- 21.2 ml of NH_4OH.
- 39.2 ml of Formamide
- 117.2 ml of Benzyl Alcohol
- 22.4 ml of Tetraethyl orthosilicate (TEOS)

All the chemicals were added to the beaker very gently along the wall of the beaker, in the sequence mentioned above. The chemical synthesis was performed under a fume-hood, because ammonia and the other chemicals had a strong stingy smell. Once TEOS was added, which contained the silicon which was the major chemical substance for the formation of these nanoparticles, the reaction started. At that point the solution was mixed very gently without greatly disturbing the reaction mixture because, otherwise, a gel like structure would form which eventually would give rise to a wider particle size distribution, clearly an undesirable state of affairs for our purpose. Once the gentle mixing of the chemicals was completed, the reaction mixture was kept for about 2 hours under the fume-hood without disturbing it. Initially, the chemical mixture was transparent but as the particles started to form, the color of the solution began to change from

transparent to pink thereby giving us an initial indication that the chemical reaction was taking place. After 2 hours, 5 ml of 3-(trimethoxyl) propyl methacrylate was added to the chemical mixture. This chemical was used specifically for coating the surface of the particles, which had already been formed in the initial 2 hours of the reaction, to yield the desired surface/electrical properties of these particles. 15 minutes after the 3-(trimethoxyl) propyl methacrylate had been added, the sample was taken out and placed in the distillation set-up **[Fig. 5A1]**, designed specifically for removing the extra amount of liquid, i.e., mostly water and ammonia, which was present during the reaction in the system. During the distillation, which lasted 24 hours, the sample was maintained at a constant temperature of ~50^0C with a temperature controller and under a vacuum of ~0.1millitorr, using a vacuum pump (Vector Inc.). Following this ~24 hour distillation, a significant amount of liquid (~30ml) had evaporated from the sample leaving a concentrated suspension along with (~1-2 grams) of particles settled at the bottom of the flask. The latter were then re-suspended into the concentrated portion of the liquid.

Subsequently, this concentrated suspension was placed in a centrifuge for ~7 hours at 30g to separate the particles from the parental fluid. At the end of that period, the sample was taken out showing a clear demarcation between the pure liquid and the particles which had settled at the bottom of the centrifuge tube. The liquid from the sample was then drained and a small amount of 4-methylcyclohexanol, whose refractive index matched that of the already grown particles, was added and the particles were re-dispersed by shaking. This new suspension was kept for 16 hours in the centrifuge at 30g after which, the sample was taken out and the top liquid layer was decanted leaving a concentrated layer of particles. The procedure of resuspending the particles in 4-methyl cyclohexanol

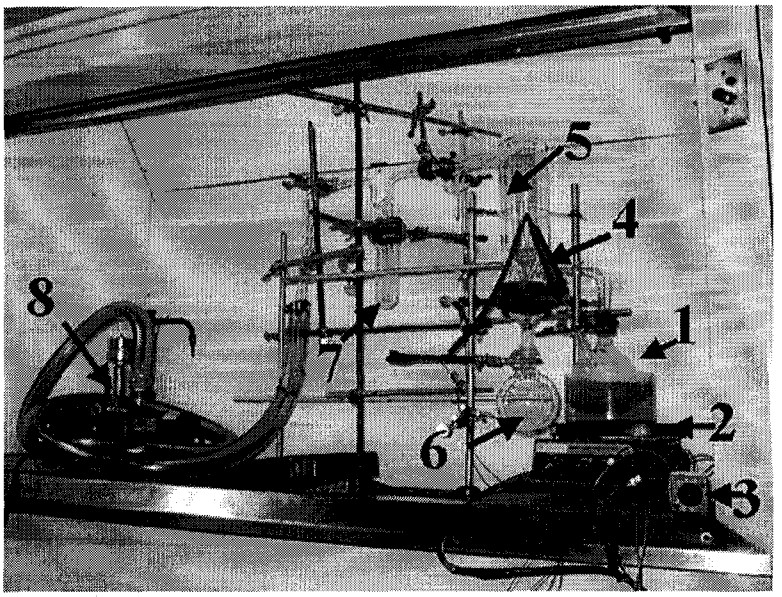

Figure 5A1: Distillation apparatus, showing all the details, (1) Sample flask, (2) Heater along with a water bath, (3) Temperature controller, (4) Thermocouple, (5) Condenser, (6) Flask for collecting the condensed vapors, (7) Extra condenser for trapping the vapors and preventing them from going into the vacuum pump, (8) Vacuum pump.

was repeated 3-4 times to remove most of the original parental fluid which had remained in the suspension. At the end of the procedure described above, we observed that the particles were perfectly refractive index matched with 4-methyl cyclohexanol. The suspension thereby prepared was then used for measuring its dielectric properties and particle size characterization, as a prelude for the dielectrophoresis experiments.

The size distribution of these particles, measured using a Coulter N-4 device [Chapter 2], showed a mean particle diameter of 553nm, with polydispersity of 0.116 [**Appendix 5B1**]. The plot shown in [**Fig. 5A2a**] indicates that the particles are definitely not monodisperse, as we were hoping, with their diameters ranging from 200nm to 2000nm, clearly an undesirable state of affairs for our experiments. We also employed an alternate method of measuring the particle size by taking an image of the solid particles after drying them for 2 days under a fume hood. The image, shown in [**Fig. 5A2b**], was taken

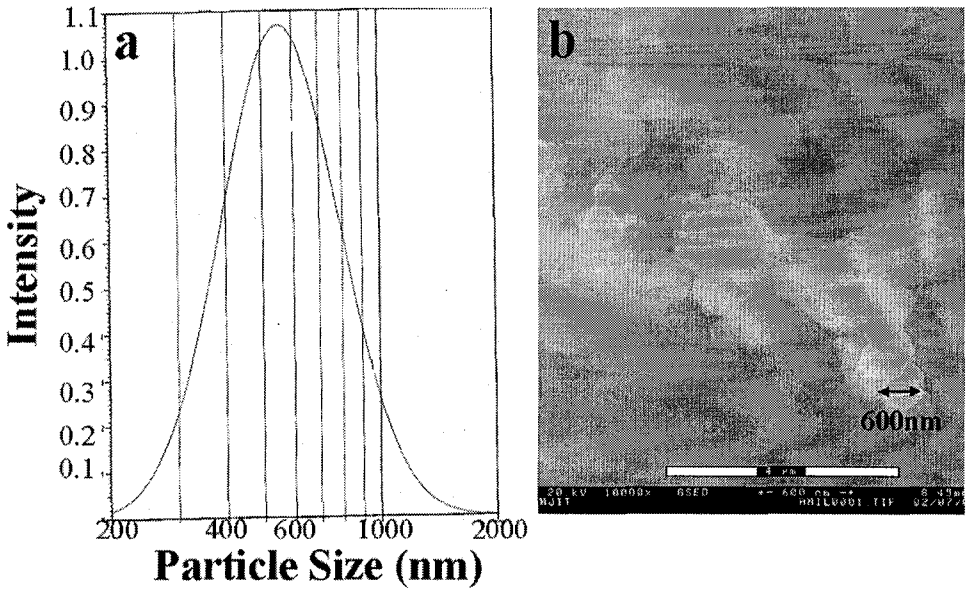

Figure 5A2: Particle size distribution using (a) Coulter N4 Plus and (b) SEM image of particles.

using SEM (scanning electron microscope) to characterize the particles, as concerns their size and shape. From the image, it is clear that we have spherical particles with a wide size distribution consistent with the measurements performed using the COULTER N4Plus. Although, admittedly, the size distribution is quite wide, this in principle should not be a serious issue since with filtration techniques available today one could easily narrow down this size distribution, if needed.

In the work described above, we were able to make a suspension of silica nanoparticles having a refractive index that matched with that of the 4-methylcylohexanol. Now our objective was to change the refractive index of some of these particles so as to detect them by optical means. Hence, following the recipe given by [**58**], we sought to replace some of the silica in the particles by a colored transition metal element Titanium (Ti). It was shown by [**59**], that 62% of the silanols were removed by the addition of only 0.025 equivalents of TET (Titanium ethoxide), and that, with 10% TET no silanol groups could

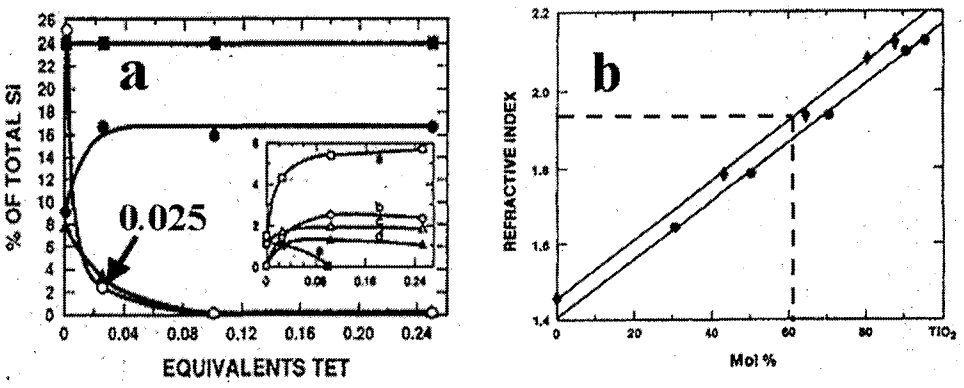

Figure 5A3: Plot showing the effect on the refractive index of the suspension by adding the Titanium compound.

be detected inside the particles. The change in the refractive index as a function of the fraction of TiO_2 being present inside the particles formed in the solution is shown in [**Fig. 5A3**].

As can be seen from the plot, a 62% molar fraction of TiO_2 with a 38% molar fraction SiO_2 will have a refractive index of ~2.0, compared to that of 100% SiO_2, 0% TiO_2 used previously which was of ~1.4. So while preparing the initial reaction mixture we added the volume required for the 62% TiO_2 ~ $0.025\left(\frac{22.4\rho_{TEOS}}{208.086}\right)\left(\frac{227.867}{\rho_{Ti(OC_2H_5)_4}}\right)$ cc of Titanium ethoxide. The subsequent steps following the addition of the $Ti(OC_2H_5)_4$ to the reaction mixture were the same. In the end we could see that the final suspension containing Ti, as one of the component inside the particles, showed a greenish color. The density of the particles was expected to be little higher (because Ti is heavier than Si) but no change in the electrical properties (coming from the coating layer on the particles), and of the particle size distribution (depending on the time how long we let the reaction mixture go) was expected. A photograph of the final suspensions formed, with and without the addition of the Ti group is shown in [**Fig. 5A4**].

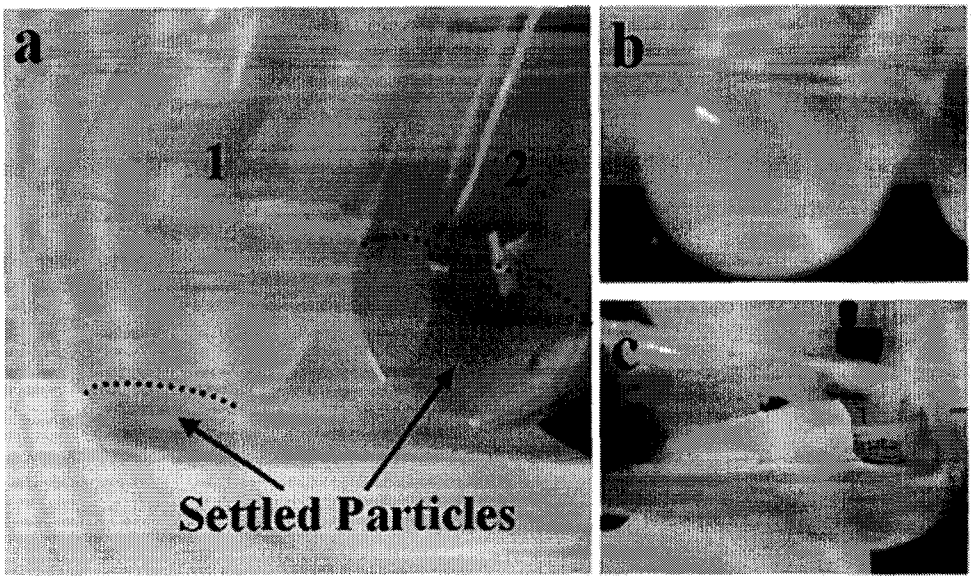

Figure 5A4: Photographs showing the final suspensions: (a) with (1) and without (2) the addition of the Titanium compound (b)-(c) shows a layer of settled particles containing Ti at the bottom.

5A.3 Dielectrophoresis Experiment

We conducted some preliminary experiments to test the dielectrophoretic behavior of these suspensions. The experiments were conducted using a very simple electrode configuration shown in [**Fig. 5A5**], in which the suspension was placed in the gap between two needles, connected to the high-voltage and the ground, respectively, of an ac electric field power supply. The strength of the electric field near the edges of the needles is highest and decays as we go away from them. So, if the particles are positively polarized, they would be expected to accumulate near the needle tip, while the negatively polarized particles, should be repelled from those high field regions. Once the field was turned on, the particles, seen as green due to the presence of the Ti group, were attracted toward the electrode edges showing the positive dielectrophoretic behavior of the suspension.

But we found that even though we worked in the 5kHz frequency range of the applied ac

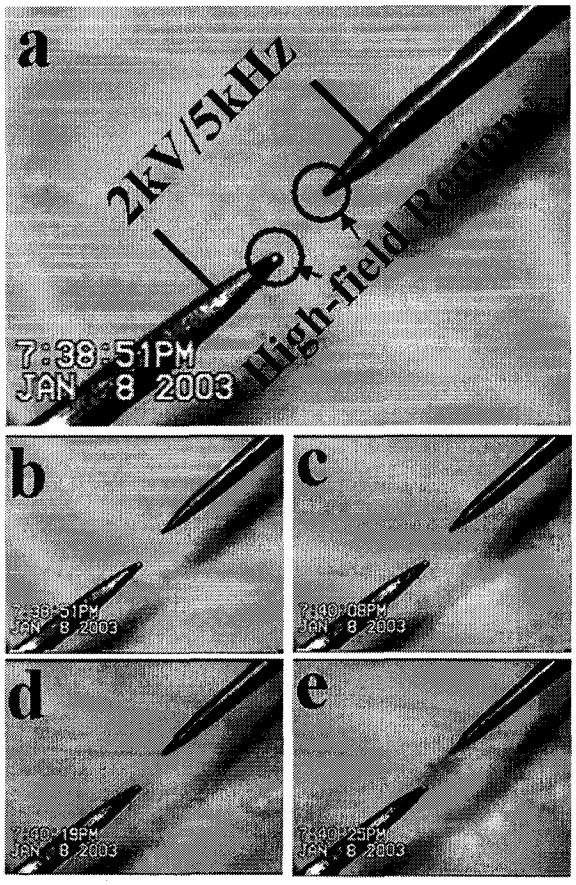

Figure 5A5: Experimental results showing positive dielectrophoresis for a pair of needles geometry. The green color in between the needles confirms the presence of particles accumulation in that region.

field, a spark was generated at the end probably due to the high conductivity arising from the presence of water inside the system. Unfortunately, with the facilities available to us, we were unable to work with very high frequencies, where the effect of the fluid conductivity could be substantially suppressed, and with ac field gradients ~kV/mm, in macro devices. But if resources could be made available, this could be achieved in micro devices where even with voltage of several volts, we could generate field strengths several ~kV/mm while still permitting us to work within the frequency range of several MHz where fluid conductivity would be expected to play a negligible role.

5A.4 Results and Discussions

We presented here a novel method of manufacturing a suspension composed of ~600nm particles, with the majority of them having a refractive index matched equal to that of the suspending fluid. This suspension could be used to study electric field induced particle aggregation in concentrated suspensions in micro devices. This suspension was unique because it could allow us to observe the details about the particle kinetics and their distribution even at very high concentration. Changing the coating material provides flexibility in controlling the electrical properties of the particles and changing the material from Ti to any other transition metal group would impart a different color to the particles. In addition, changing the duration of the chemical reaction would lead to different particle sizes, i.e. the longer the duration of the reaction the larger will be the particle size. A possible extension of this work could be to test this suspension in a micro device.

Appendix 5A[1]

POLYDISPERSITY

[1]means $\sqrt{\frac{\sum_{i=1}^{N}(x_i-\bar{x})^2}{N}} = 0.116\bar{x}$, $\bar{x}$ is the mean particle diameter, N being the number of measurement points.

RELATION BETWEEN THE INTENSITY TO THE NUMBER CONCENTRATION OF THE PARTICLES IN THE SUSPENSION:

[2] The Intensity of the scattered light follows:

$$\frac{I_\theta}{I_0} = \frac{2\pi^2(1+\cos^2\theta)(dn/dc)^2 Mc}{N_A\lambda^4 r^2} \propto N$$

which is proportional to the number of particles N given that $c = \frac{NM}{N_A}$ with N_A being Avogadro's number and M the molecular weight of the particles. Also n is the refractive index of the particles, r is the distance of the particles from the measuring sensor, θ is the scattering angle and λ is the wavelength of the applied beam of intensity I_0 [**60**]

Appendix 7A

Effect of Charge Transfer: Behavior of positively polarized aluminum oxide particles under low frequency ac electric field

These experiments were conducted in the experimental geometry shown in Fig. 7.1a, where the cylindrical cavity was filled with a 0.2% (v/v) particle concentration suspension of heavy Al_2O_3 particles (of two different diameters, d_p=1-2μm and 90μm, ρ_p=3.75g/cc) with relative particle polarization, $Re(\beta)$~0.3, suspended in Mazola corn Oil (ρ_f=0.92g/cc, ε_f=2.87). The suspension details are in Chapter 4. Before the field application, these particles, owing to the density mismatch, initially settle at the bottom electrode forming nearly a single particle thick layer. Following the field application, the amplitude of which was held constant at ~1.4kV/mm while its frequency (sinusoidal) was varied from 1 to 1000 Hz, we observed that these particles had no discernable vertical motion, for applied frequencies greater than ~100Hz, except for a slight re-arrangement among themselves in the plane of the bottom electrode due to the well-known dipolar interaction. But, on decreasing the frequency to 10 or 1Hz, we noticed that these particles acquired a vertical motion and interacted among each other forming particle clusters as shown in [**Fig. 7A1 & 7A2**], in the same fashion as observed by Aranson et. al. [**61, 62**]. The height to which the particles rose was found to depend on the frequency of the applied ac field. Specifically, at 1 Hz, the particles were seen to hit the upper electrode; but on increasing the frequency, the particles rose to progressively lower heights and, for frequencies above 100Hz, their vertical motion ceased completely. This experiment shows that by

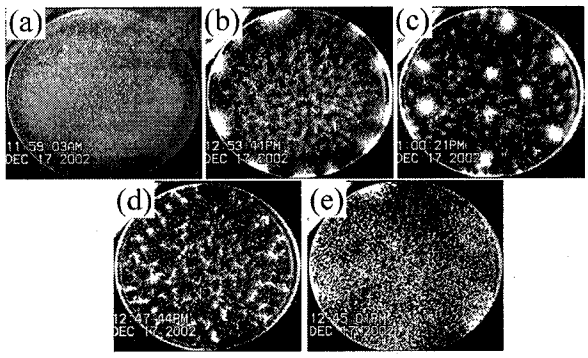

Figure 7A1: Experiments conducted with heavy aluminum oxide particles (d_p=90μm) suspended in Mazola Corn Oil with c=0.002(v/v), sedimentation time, t_{sed}~11sec (much shorter than the time required to start the experiment after pouring the suspension inside the cavity, $t_{process}$~5-10min); (a) particles initially settled at the bottom electrode before the field application; (b)-(e) correspond to the structures seen in the plane perpendicular to the applied field of magnitude 1.4kV/mm and frequencies (b) 1Hz (Sinusoidal), (c) 1Hz(Pulse), (d) 10Hz(Sinusoidal), and (e) 100Hz(Sinusoidal), respectively. The experiment was started with an applied frequency of 1kHz(Sinusoidal). The particles are seen as the white spots and a black region refers to the absence of particles throughout the length of the cavity along the field direction. The experiment was conducted for fixed experimental geometry with dimensions of L=2.79mm, and D=1.5 inch.

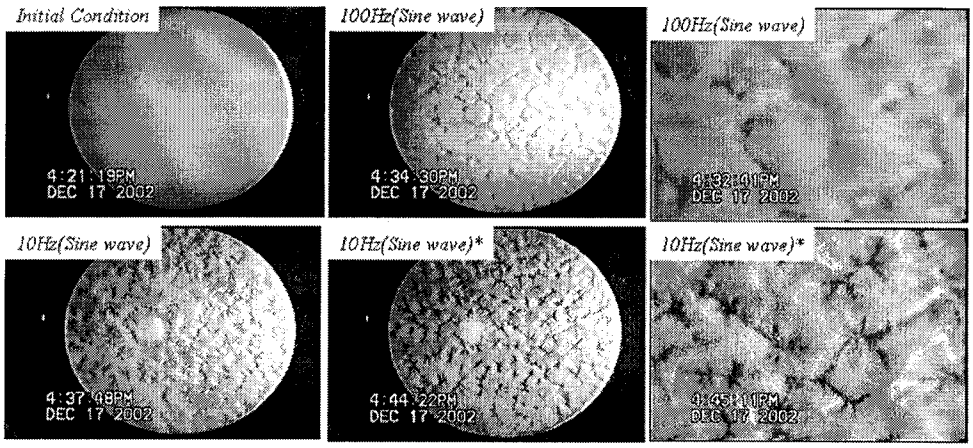

Figure 7A2: Experimental pictures for 1-2μm sized Al_2O_3 particles suspended in corn oil, c=0.001(v/v), and subjected to a ~1.4kV/mm ac electric field at various frequencies shown in the inset of each photograph. The electric field was turned on at 4:22PM with the applied field at a 1kHz frequency. No significant changes were discerned at 1kHz, while a decrease in the frequency to 10 and 100Hz led to the formation of a pattern as a result of charge transfer. L=2.79 mm, and D=1.5 inch.

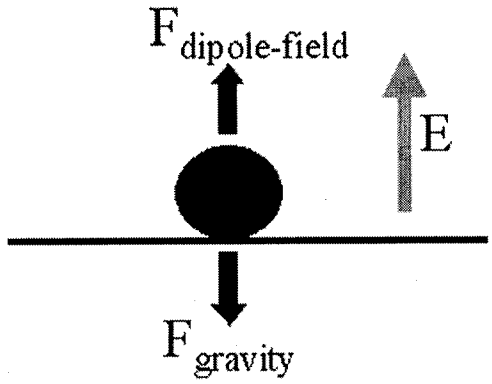

Figure 7A3: A schematic showing the principle of charge transfer phenomenon observed in Figures 7A1 & 7A2.

tuning the frequency of the applied ac field we could eliminate electrophoretic effects in the vertical direction implying that the patterns formed due to charge transfer. We also found that varying the shape of the frequency from sinusoidal to a pulse led to a different kind of pattern [**Fig. 7A1**].

A simple calculation shows that the minimum electric field strength required to lift a conducting metallic charged particle from the bottom electrode surface [**Fig. 7A3**] is $E_c = \left(\frac{(\rho_p - \rho_f)ga}{3\varepsilon_0 \varepsilon_f k} \right)^{1/2}$, where k=1.36 for the metallic particles [7]. When the applied field E exceeds E_c, the particle will start moving vertically upwards and leave the surface of the electrode, at which point it will experience a viscous drag force owing to the hydrodynamic resistance of the fluid and will eventually move with a velocity $\vec{u} = 2a\varepsilon_0 \varepsilon_f E^2 k / 3\eta_f$, assuming that $E >> E_c$. Assuming that the field does not change its sign while this particle travels a distance, H, before exchanging its charge with another oppositely charged particle or with the upper electrode, the characteristic time and

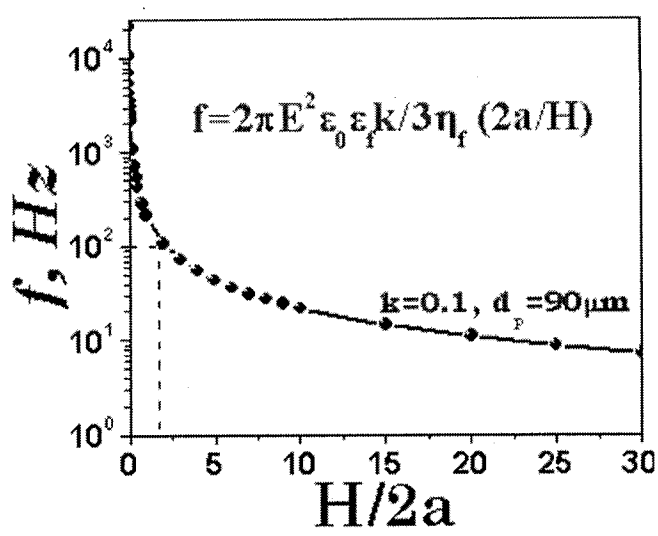

Figure 7A4: A plot showing the critical frequency vs. the maximum amplitude of the vertical excursion of particle for 90 μm sized particle.

frequency at which its charge is being transferred is given by, $t = H/\bar{u}$ and $f_c = \frac{2\pi}{t} \sim \frac{2\pi\varepsilon_0\varepsilon_f E^2 k}{3\eta_f}\left(\frac{2a}{H}\right)$. Therefore by applying uniform ac electric field $E = E_0 \sin(2\pi ft)$ with $E_0 > E_c$ and adjusting its frequency, f, allows one to control the vertical excursion of the particles by turning them back before they collide with the upper electrode [**Fig. 7A4**].

Similar experimental results were seen with suspensions of 1-2μm Al_2O_3 particles, shown in [**Fig. 7A2**], and polyalphaolefin particle suspensions in Mazola Corn Oil where no particle motion was observed for frequencies as low as ~10Hz, suggesting that a frequency ~100Hz or higher is sufficient to eliminate the effect of charge transfer.

Appendix 7B

Particle Ring Formation at the Three-Phase Contact Line

Here we will report the discovery of a particle ring formation at the three-phase contact line arising from an electric-field induced phase separation followed by negative dielectrophoresis.

We conducted two different types of experiments. In the first type, we established the occurrence of a phase separation when two immiscible fluids initially forming layers one on top of another were subjected to a spatially uniform ac electric field at frequencies ~O (10^2Hz) where electro-convection and electrophoretic effects inside the system could be neglected [**31**]. Before the field application, the liquid layers stayed one on top of the other, with heavier fluid being at the bottom but, once the field was turned on, a phase separation took place leading to the formation of columnar structures [**63, 64**]. Now, to make the story more interesting, we replaced one of the fluids on the top with a corn oil (ε_f =2.87, ρ_f =0.92g/cc, μ_f~60cp at 23^0C) suspension containing neutrally buoyant, negatively polarized poly alpha-olefin particles (ε_p =2.30, ρ_p =0.92g/cc, d_p~87.6μm). The bottom consisted of a layer of Silicon Oil (ε =2.02, ρ =1.03g/cc). Once the field was turned on, we observed a phase separation with the Silicon Oil forming conical structures as shown in [**Fig. 7B1**]. But interesting enough, we noticed that the particles which were initially uniformly suspended in the corn oil, migrated to the lower (grounded) electrode as seen from the top, forming a 2-3 particle wide layer at the three-phase contact line. In contrast no particles were observed at the three-phase contact line in the conical ring region, on the upper electrode (High-voltage). We also observed a convective radial flow

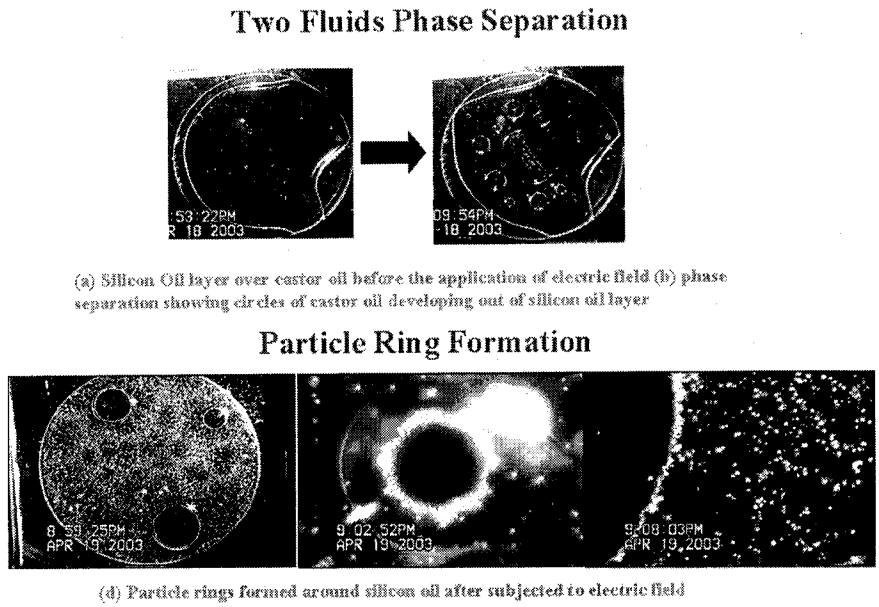

Figure 7B1: Showing phase separation on application of the electric field, as well as formation of the ring pattern at the three-phase interface.

pattern, around this particles ring, in which the particles from the bulk region migrates toward the interface of the two fluids in the region somewhere inbetween the gap and either migrated to the three-phase contact point located on the bottom electrode or returned to the bulk and repeated this motion continuously. The phase separation for two different fluid systems as well as the particle ring formation at three-phase contact line is shown in [**Fig. 7B1**].

In the third experiment, we varied the dielectric contrast between two fluids, using air (ε =1.0) as one medium along with the polyolefin suspension. We noticed that an increase in the dielectric constants between the fluids led to an increase in the number of particles accumulating in the ring at the three-phase contact point [**Fig. 7B2**]. But this time, the particles mainly accumulated on the upper (high-voltage) electrode contrary to the previous experimental observation with the polyolefin suspension and the Silicon Oil.

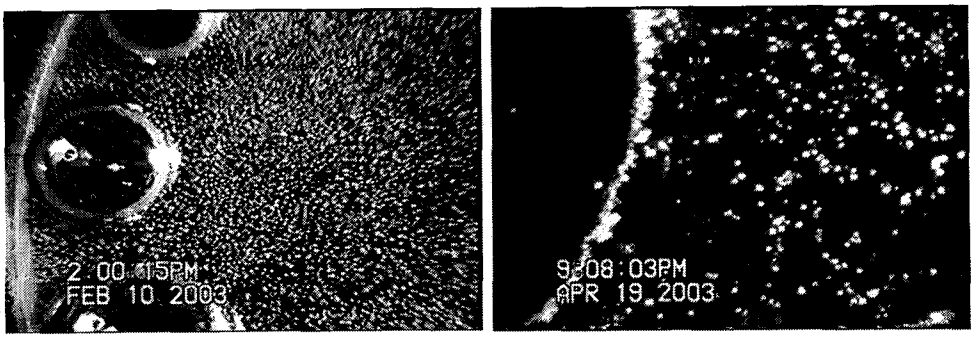

Figure 7B2: Experimental pictures showing the effect of an increase in the dielectric mismatch between two suspending fluids. Increasing the dielectric mismatch leads to the accumulation of more particles at the three phase contact line.

To provide a plausible explanation for this phenomenon, we need to split the problem into two steps. First to predict the phase separation we recall that a simple analysis based on the free energy calculation [**65**] shows that the arrangement of [**Fig. 7B3b**] has low free energy compared to that of [**Fig. 7B3a**], for a fixed volume ratio of the two phases. Assuming as a first estimate a conical structure for the shape of the columnar structure in accordance with [**Fig. 7B1b**], we solved the Laplace's equation and computed the electric field distribution [E^2], shown in [**Fig. 7B4**], for this conical structure. We imposed the symmetry boundary conditions at the far ends along with the continuity of electric displacement, i.e. D, at the two fluid interfaces, i.e. $\varepsilon_1 E_1 = \varepsilon_2 E_2$.

As is evident from the electric field distribution, there exists an electric field (E^2) minimum at the three-phase contact line at the bottom electrode (i.e. 2.25, 0) and by the virtue of negative polarization of the polyolefin particles in corn oil (Phase 1), they will be attracted toward the minimum field region as a result of negative dielectrophoresis

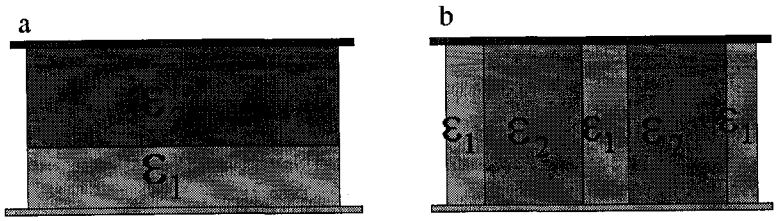

Figure 7B3: Figures showing two states, in which the free energy for state (b) is lower than that of (a), implying that the system will try to go towards, the cylindrical column formation.

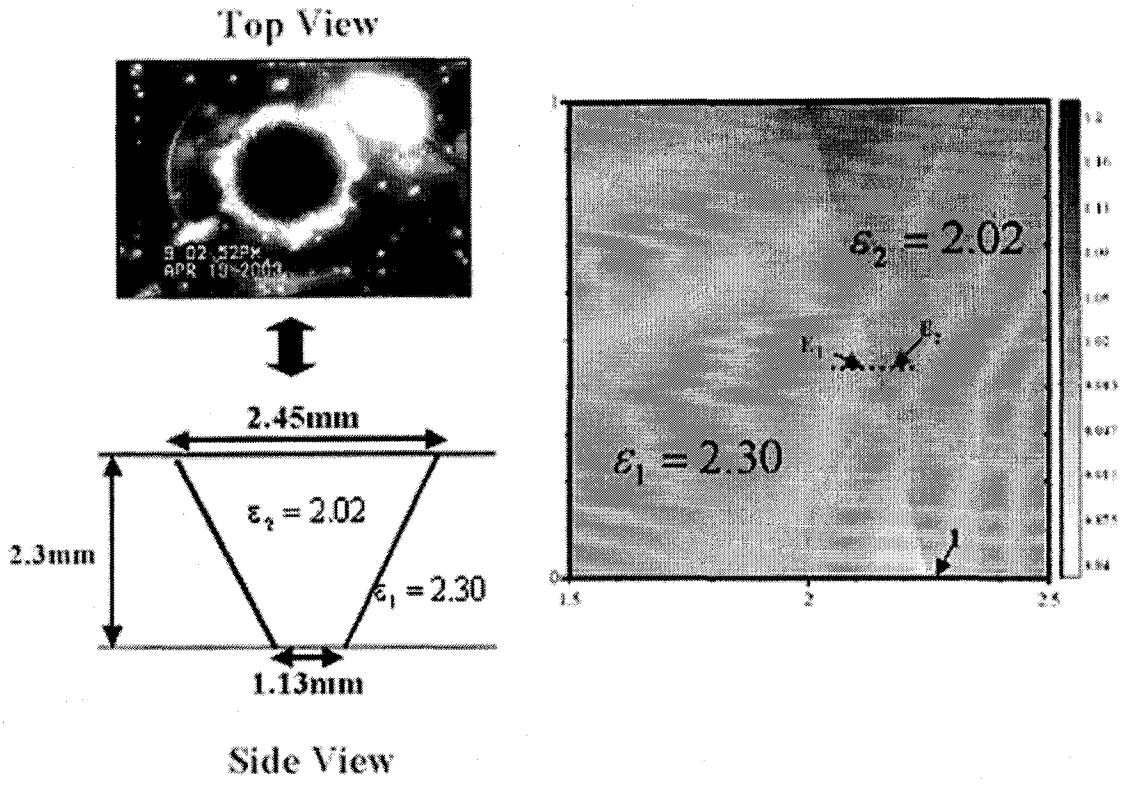

Figure 7B4: Showing the electric field calculations (i) the electric field minima is located at the lower electrode, exactly at the three-phase interface. (ii) There is an increase in the electric field as we proceed from the high to the lower dielectric medium, i.e. from medium 1 to medium 2.

forming a particle-ring structure as seen from the top at the three-phase contact point on the bottom electrode. Also the three-phase contact line at the upper electrode has a maximum in the electric field, hence no particle accumulation in the interfacial region on the upper (high-voltage) electrode would be expected, consistent with the experimental

observations. Another observation from the electric-field distribution suggests that, at the interface of the two fluids, an olefin particle coming from the left, will not be able to penetrate the surface of the two fluids at any fixed vertical location because $E_2 > E_1$, i. e. negatively polarized particle will not wish to go towards regions of higher electric field, and hence either will join the region, where the field is lowest, at the three-phase contact line on the bottom electrode or will return back to the bulk as observed experimentally, i.e. by convection around this conical structure as can be seen from a movie. From this simple picture of the electric field distribution we are able to capture the physics behind this process. On the other hand, it might be desirable to conduct a more detailed study by solving the full Maxwell equations to first predict the shape of the interface, followed by simulations for predicting the motion and subsequent accumulation of these particles in the regions of minimum field.

Bibliography

[1] B. Khusid and A. Acrivos, "Effect of conductivity in electric-field-induced aggregation in electrorheological fluids" Phys. Rev. E, **52**, 1669 (1995).

[2] B. Khusid and A. Acrivos, "Effect of interparticle electric interactions on dielectrophoresis in colloidal suspensions" Phys. Rev. E, **54**, 5428 (1996).

[3] B. Khusid and A. Acrivos, "Phase diagrams of electric-field-induced aggregation in conducting colloidal suspensions" Phys. Rev. E, **60**, 3015 (1999).

[4] A. D. Dussaud, B. Khusid, and A. Acrivos, "Particle segregation in suspensions subject to High-gradient ac electric fields", J. Appl. Phys., **88** (10), 5463(2000).

[5] Z. Qiu, N. Markarian, B. Khusid, and A. Acrivos, "Positive dielectrophoresis and heterogeneous aggregation in high-gradient ac electric fields", J. Appl. Phys., **92**(5), 2829(2002).

[6] N. Markarian, M. Yeksel, B. Khusid, K. R. Farmer, and A. Acrivos, "Particle motions and segregation in dielectrophoretic microfluidics" J. Appl. Phys., **94**(6), 4160(2003).

[7] T. B. Jones, " Electromechanics of particles" (Cambridge University Press, Cambridge, 1995).

[8] I. J. Lin and L. Benguigui, "Progress in Filtration and Separation" edited by R. J. Wakerman (Elsevier, Amsterdam, 1983), **3**, pp. 149-205.

[9] H. A. Pohl, " Dielectrophoresis: The behavior of Neutral Matter in Nonuniform Electric fields" (Cambridge University Press, Cambridge, 1978).

[10] M. Shapiro, A. L. Shalom, and I. J. Lin, "Dielectric flocculation of nondiffusive particles in a nonconducting fluid and a uniform electric field", J. Appl. Phys., **58**, 1028 (1985).

[11] L. Benguigui and I. J. Lin, "Phenomenological aspect of particle trapping by dielectrophoresis", J. Appl. Phys., **56**, 3294(1984).

[12] N. G. Green and H. Morgan, "Dielectrophoretic separation of nano-particles", J. Phys. D, **30**, L 41(1997).

[13] R. Pethig, Y. Huang, X. B. Wang, and J. P. H. Burt, "Positive and negative dielectrophoretic collection of colloidal particles using interdigitated castellated microelectrodes", J. Phys. D, **25**, 881(1992).

[14] W. M. Arnold, "Positioning and levitation media for the separation of biological cells", IEEE Transactions on Industrial Applications, 37(5), (Sep-Oct 2001).

[15] W. M. Arnold, "Positioning, Levitation and separation of biological cells", Inst. Phys. Conf. Ser. No. 163, Presented at 10th Int. Conf., Cambridge (1999).

[16] X. B. Wang, J. Vykoukal, F. F. Becker, and P. R. C. Gascoyne, "Separation of Polystyrene Microbeads Using Dielectrophoretic/Gravitational Field-Flow-Fractionation", Biophys. J. 74, 2689(1998).

[17] N. Markarian, M. Yeksel, B. Khusid, K. Farmer, and A. Acrivos, "Limitations on the scale of an electrode array for trapping particles in microfluidics by positive dielectrophoresis", Appl. Phys. Lett., **82**, 4839(2003).

[18] D. J. Bennett, B. Khusid, C. D. James, P. C. Galambos, M. Okandan, D. Jacqmin, and A. Acrivos, "Combined field-induced dielectrophoresis and phase separation for manipulating particles in microfluidics", Appl. Phys. Lett., **83**, 4866(2003).

[19] W. B. Russel, D. A. Saville, and W. R. Schowalter, "Colloidal Dispersions", (Cambridge University Press, Cambridge, 1989).

[20] V. V. Daniel, "Dielectric Relaxation", (Academic Press, London and New York, 1967).

[21] S. S. Duskin and V. N. Shilov, "Dielectric Phenomena and Double Layer in Disperse Systems and Polyelectrolytes", (John Wiley, New York, 1974).

[22] H. P. Langtangen, "Computational Partial Differential Equations: Numerical Methods and Diffpack Programming", (Springer-Verlag, Berlin, 1999).

[23] http://www.beckman.com

[24] L. D. Landau, E. M. Lifshitz, and L. P. Pitaevski, "Electrodynamics of Continuous Media", (Pergamon, Oxford, 1984).

[25] F. N. H. Robinson, "Macroscopic Electromagnetism", (Pergamon, Oxford, 1973).

[26] M. Ungarish, "Hydrodynamics of Suspensions", (Springer-Verlag, Berlin, 1993).

[27] N. Markarian, M. Yeksel, B. Khusid, A. Kumar, and P. Tin, "Effects of clinorotation and positive dielectrophoresis on suspensions of heavy particles", Phys. Fluids, **16**, 1826(2004).

[28] C. F. Zukoski, "Material Properties and the Electrorheological response", Annu. Rev. Mater. Sci., **23**, 45(1993).

[29] Progress in Electrorheology. Science and Technology of Electrorheological Materials, edited by K. O. Havelka and F. E. Felisko (Plenum, New York, 1995).

[30] G. K. Batchelor, "An Introduction to Fluid Mechanics", (Cambridge University Press, Cambridge, 1993), pp. 182,183.

[31] A. Kumar, Z. Qiu, A. Acrivos, B. Khusid, and D. Jacqmin, "Combined negative dielectrophoresis and phase separation in non-dilute suspensions subject to a high-gradient ac electric field", Phys. Rev. E, **69**, 021402(2004).

[32] R. E. Rosenzweig, "Ferrohydrodynamics", (Cambridge Univ. Press, 1985).

[33] K. O. Havelka, "Progress in Electrorheology: Science and Technology of Electrorheological Materials", (Kluwer Academic Publication, August 1995).

[34] M. Nakano and K. Koyama, "Electrorheological Fluids, Magnetorheological Suspensions and Their Application", (World Scientific, 1999).

[35] M. P. Hughes, "Nanoelectromechanics in Engineering and Biology", (CRC Press, 2002).

[36] Y. Tsori, F. Tournilhac, D. Andelman, and L. Leibler, "Structural Changes in Block Copolymers: Coupling of Electric Field and Mobile Ions", Phys. Rev. Lett. **90**, 145504 (2003).

[37] W. D. Ristenpart, I. A. Aksay, and D. A. Saville, "Electrically Guided Assembly of Planer Superlattices in Binary Colloidal Suspensions", Phys. Rev. Lett. **90**, 128303(2003).

[38] C. Mio and D.W.M. Marr, "Optical Trapping for the Manipulation of Colloidal Particles", Advanced Materials, **12**, 917(2000).

[39] C. Mio, T. Gong, A. Terray, and D.W.M. Marr, "Design of a Scanning Laser Optical Trap for Multiparticle Manipulation", Review of Scientific Instruments, **71**, 2196(2000).

[40] R.W. Applegate Jr., J. Squier, T. Vestad, J. Oakey, and D.W.M. Marr, "Optical Trapping, Manipulation, and Sorting of Cells and Colloids in Microfluidic Systems with Diode Laser Bars", Optics Express, **12**, 4390(2004).

[41] P. G. De Gennes and P. A. Pincus, Phys. Kondens. Mater. **11**, 189(1970).

[42] J. H. E. Promislow, A. P. Gast, and M. Fermigier, "Aggregation kinetics of paramagnetic colloidal particles", J. Chem. Phys. **102**(13), 5492(1995).

[43] E. M. Furst and A. P. Gast, " Dynamics and lateral interactions of dipolar chains", Phys. Rev. E. **62** (5), 6916(2000).

[44] T. C. Halsey and W. Toor, "Structure of electrorheological fluids", Phys. Rev. Lett., **65**,2820 (1990).

[45] T. C. Halsey, "Electrorheological Fluids." Science **258**, 761(1992).

[46] R. Tao and J. M. Sun, "Three-dimensional structure of induced electrorheological solid", Phys. Rev. Lett. **67**, 398 (1991).

[47] G. A. Flores, J. Liu, M. Mohebi, and N. Jamasbi, "Magnetic-field-induced nonequilibrium structures in a ferrofluid emulsion", Phys. Rev. E, **59**, 751 (1999).

[48] M. F. Islam, K. H. Lin, D. Lacoste, T. C. Lubensky, and A. G. Yodh, "Field-induced structures in miscible ferrofluid suspensions with and without latex spheres", Phys. Rev. E **67**, 021402 (2003).

[49] M. Seul and D. Andelman, Science **267**, 476 (1995).

[50] Y. Grasselli, G. Bossis, and E. Lemaire, J. Phys. (France) II **4**, 253 (1994).

[51] E. Lemaire, Y. Grasselli, and G. Bossis, J. Phys. (France) II **2**, 359 (1992).

[52] Dassanayake U, Fraden S, van Blaaderen A. Structure of Electrorheological Fluids, J Chem Phys **112**:3851(2000).

[53] D. J. Klingenberg, Frank van Swol, and C. F. Zukoski, "Dynamic simulation of electrorheological suspensions", J. Chem. Phys. **91**(12), 7888(1989).

[54] R. T. Bonnecaze and J. F. Brady, "Dynamic simulation of an electrorheological fluid", J. Chem. Phys. **96**(3), 2183(1992).

[55] J. E. Martin, "Thermal Chain Model of Electrorheology and Magnetorheology", Phys. Rev. E **63**, 011406 (2001).

[56] M. D. Johnson, X. Duan, B. Riley, A. Bhattacharya, and W. Luo, "Thermodynamic model of electric-field-induced pattern formation in binary dielectric fluids" Phys. Rev. E **69**, 041501(2004).

[57] J. E. Martin, D. Adolf, and T.C. Halsey, "Electrorheology of a model colloidal fluid", J. Colloidal Interface Sci. **167**(2), 437(1994).

[58] Sol-Gel Science: The Physics and Chemistry of Sol-Gel processing (Academic Press Inc. Brinker, 1990, Chapter 3: Hydrolysis and Condensation II: Silicates (p. 226).

[59] J. D. Basil and C. C. Lin, "Ultrastructure Processing of Advance Ceramics" edited by J. D. Mackenzie and D. R. Ulrich (John Wiley, New York, 1988).

[60] A. Kumar and R. K. Gupta, "Fundamentals of Polymers", (Mc Graw Hill, 1998).

[61] M. V. Sapozhnikov, Y. U. Tolmachev, I. S. Aranson, and W. –K. Kwok, "Dynamic Self-Assembly and Pattern in Electrostatically Driven Granular Media", Phys. Rev. Lett. **90**, 114301(2003).

[62] I. S. Aranson, D. Blair, V. A. Kalatsky, G. W. Crabtree, W. –K. Kwok, V. M. Vinokur, and U. Welp, "Electrostatically Driven Granular Media: Phase Transitions and Coarsening", Phys. Rev. Lett. **84**, 3306(2000).

[63] S. Hermenghuas, "Dynamical instability of thin liquid films between conducting media", Phys. Rev. Lett. **83**, 2359(1999).

[64] J. R. Melcher, "Continuum Electrohydrodynamics" (The MIT Press, Cambridge, Massachusetts, and London, England, 1981).

[65] Xin-Lu Tang, Ke-Qin Zhu, E. Guan, and Xiao-Ping Wu, "Electric-Field-Induced Phase Separation in Electrorheological Fluids", in Electrorheological Fluids: Mechanisms, Properties, Technology, and Applications, edited by R. Tao and G. D. Roy (World Scientific, Singapore, 1994), p. 223.

[66] P. Papon, J. Leblond, and P. H. E. Meijer, " The Physics of Phase Transitions: Concepts and Applications" (Springer-Verlag Berlin, 2002).